# Discriminative adsorption of amphiphilic monolayer protected gold nanoparticles on amyloid fibers

# THÈSE Nº 7037 (2016)

#### PRÉSENTÉE LE 6 JUIN 2016

À LA FACULTÉ DES SCIENCES ET TECHNIQUES DE L'INGÉNIEUR
LABORATOIRE DES NANOMATÉNAUX SUPRAMOLÉCULAIRES ET INTERFACES - CHAIRE CONSTELLIUM
PROGRAMME DOCTORAL EN SCIENCE ET GÉNIE DES MATÉRIAUX

#### ÉCOLE POLYTECHNIQUE FÉDÉRALE DE LAUSANNE

POUR L'OBTENTION DU GRADE DE DOCTEUR ÈS SCIENCES

#### PAR

# Paulo Henrique JACOB SILVA

acceptée sur proposition du jury:

Prof. H. Hofmann, président du jury Prof. F. Stellacci, directeur de thèse Prof. L. Pasquato, rapporteuse Prof. T. Knowles, rapporteur Prof. H. Lashuel, rapporteur



"Dorm'inha pequena Não vale a pena despertar Eu vou sair Por aí afora Atrás da aurora Mais serena" I.C.S.D.P, eu tentei, vou continuar tentando.

# Acknowledgements

The results shown in this thesis would not exist without the guidance and support from my supervisor, Prof. Francesco Stellacci. More than simply acknowledging him for his advisory role, I'd like to thank him personally for reaching to me during a somber period in my life: to me, you are the inventor of the second chance.

This thesis would also not exist without the work ethic, professionalism and instrumental prowess of Marie Müller, who acquired most of the cryo electron microscopy images that build the backbone of this work, and worked with me in so many projects: Marie, it's been a pleasure and an inspiration to know and work with you.

On this note, I'd like to say: Quy Ong you are my brother. We need to do some new things.

Prof. Alfredo Alexander-Katz and Dr. Francesco Tavanti provided the simulations, without which, the current interpretations would not be possible. Dr. Maria Ricci, and Dr. Reid van Lehn, thank you for rationalizing how our particles interact with lipid bilayers.

I would also like to thank Patrizia Andreozzi, who has worked with me to systematize and build a framework to tackle batch to batch reproducibility.

For offering me their curiosity and interest in scientific dialogue, I am grateful to Benjamin Le Ouay, and Dr. Emma-Rose Janecek, who helped me write, and prepare the phosphate-protected nanoparticles.

To all my colleagues at SUNMIL, I partially apologize for my difficult temperament. Thank you Jeff Kuna, Yun Tang, Mauro Moglianetti, Marta Mameli, Kislon Voitchovsky, Ahmet Bekdemir, Zekiye Pelin Guven, Zhi Luo (Samuel Jones, Urszula Cendrowska, Sergio Allegri, Elif Ertem, Lydia Duport, Randy and Tamara Carney. Thank you Jan Gebers for patiently teaching me basic chemistry, along with all the folk at LMOM who kept I laboratory that inspired me in organization and methodology.

Prof. Fantner opened his lab for me, to which I am grateful. Pascal Odermatt kindly used his time to investigate my samples with AFM: thank you.

I am immensely grateful to all the services and comprehensive infra-structure provided by EPFL. To the people who have taught me so much, I thank Dr. David Hacker, Dr. Pascal Mieville, Dr. Thomas Lagrange and Dr. Davide Demurtas.

The Tau protein that strengthened our hypotheses was kindly provided by Nadine Ait Bouziad, from Prof. Lashuel's group.

Je tiens également à remercier Chiara Donini, Sylvie Vaucher, Gilles Auric et Monsieur Vasseur. Merci pour votre support. Et toutes les services disponible a l'EPFL.

#### **Abstract**

This thesis presents a systematic study of how different types monolayer-protected AuNPs interact with amyloid fibers. We report a class of amphiphilic gold nanoparticles capable of adsorbing onto specific surface features on these types of protein fibers. A common diseaseassociated protein fold is the amyloid state: it is characterized by a cross-beta sheet structure that forces proteins and peptides into a fibrillar state, commonly found in illnesses such as Alzheimer's disease, Parkinson's disease among many others. Amyloid diseases are typically chronic, correlated with ageing and have posed several challenges: the exact structure of the fibers is difficult to determine and their etiologic role is often unclear. This thesis shows, for the first time, that amphiphilic monolayer-protected AuNPs can discriminatively adsorb onto surface features of amyloid fibers made of  $A\beta_{1-40}$  and  $\alpha$ -synuclein in vitro and that hydrophobicity determines adsorption onto Tau fibers. Given an amyloid fiber that adopts a twisted ribbon morphology, AuNPs protected by a mixture of sulfonated and hydrophobic thiolate molecules adsorb onto specific features on the surface of the fiber, leaving other interfaces uncovered. This generates a novel supra-molecular assembly that directly interfaces an engineered nanomaterial with a biological structure, without using antibodies. Experiments and calculations demonstrated the importance of nanoparticle size and ligand-shell composition: a size cut-off around 4 nm was observed and other types of water soluble nanoparticles did not adsorb discriminatively. Small amphiphilic AuNPs act as surfactants and probably adsorb onto solvent-exposed beta sheets and small amyloidogenic oligomers. The results presented in this thesis provide a systematic framework to understand the interaction between nanoparticles and amyloid fibers. The particles can, moreover, become useful markers for amyloid research and possibly a cross-instrumental probe to reconcile spectroscopic and imaging techniques to help molecular structure determination. During this work, the synthesis and purification of large amounts of sulfonated thiolate molecules was systematized to generate libraries of differently coated water soluble gold nanoparticles (AuNPs). This helped elucidate how amphiphilic AuNPs fuse with lipid bilayers.

Keywords: gold nanoparticles, amyloid, lipid bilayers, proteins, aggregation, monolayer-protected, mixed-ligand, amphiphilic, beta sheets.

# Kurzzusammenfassung

In dieser Doktorarbeit wird eine systematische Untersuchung der Interaktion zwischen einschichtig beschichteten Gold-Nanopartikeln und Proteinaggregaten vorgestellt. Die am häufigsten mit Krankheiten assoziierte Proteinfaltung sind Amyloide. Diese sind durch eine beta-Faltblattstruktur gekennzeichnet, welche Proteine und Peptide in einen fibrillären Zustand zwingt. Diese Fibrillen werden gemeinhin in Krankheiten wie Alzheimer, Parkinson und vielen anderen gefunden. Amyloid-assoziierte Krankheiten sind in der Regel chronisch, korrelieren mit dem Altern und stellen mehrere Herausforderungen, da sowohl die genaue Struktur der Fasern schwierig zu bestimmen, als auch ihre Wirkung auf Organismen unklar ist.

Diese Arbeit zeigt zum ersten Mal, dass amphiphile einschichtig beschichtete Gold-Nanopartikel in vitro diskriminativ an Oberflächenmerkmalen von Amyloidfibrillen aus  $A\beta_{1-40}$  und  $\alpha$ -Synuclein adsorbieren, sowie dass Hydrophobie die Absorption an Tau-fasern bestimmt. Während einschichtig, aus einer Mischung sulfonierter und hydrophober Thiole, beschichtete, wasserlösliche Gold-Nanopartikel an spezifischen Oberflächenmerkmalen der Fasern adsorbieren, bleiben andere mögliche Grenzflächen unbedeckt. Dies stellt eine neue direkte supramolekulare Schnittstelle zwischen einem synthetisch hergestellten Nanomaterial und einer biologischen Struktur dar, ohne Antikörper zu verwenden.

Experimente und Berechnungen zeigten die Bedeutung der Nanopartikelgröße und Beschichtungszusammensetzung: es wurden sowohl eine Grenzgröße von circa 4 nm beobachtet, als auch dass andere Arten von wasserlöslichen Nanopartikeln nicht in der Lage sind, diskriminativ an den Fasern zu adsorbieren. Kleine amphiphile Gold-Nanopartikel wirken als Tenside und adsorbieren an Lösungsmittel-exponierten Beta-Faltblättern und kleinen Amyloid-Oligomeren. Die Ergebnisse dieser Arbeit bieten einen systematischen Rahmen, um die Wechselwirkung zwischen Nanopartikeln und Amyloid-Fasern zu verstehen. Die Partikel haben darüber hinaus Potential, als nützliche Marker für die Amyloid-Forschung und sowie als interdisziplinäres Werkzeug für spektroskopische und bildgebende Verfahren zur molekularen Strukturbestimmung genutzt zu werden.

Weiterhin wurden in dieser Arbeit die Synthese und die Aufreinigung großer Mengen sulfonierter Thiole systematisiert, um Bibliotheken unterschiedlich beschichteter wasserlöslicher Gold-Nanopartikel zu erzeugen. Dies trug unter anderem dazu bei aufzuklären, wie amphiphile Gold-Nanopartikel mit Lipid-Doppelschichten verschmelzen.

Stichwörter: Gold-Nanopartikel, Amyloid, Lipid-Doppelschichten, Proteine, Aggregation, einschichtig beschichtet, gemischte Liganden, amphiphil.

# **Table Contents**

Ack	owledgements	ii
Abs	ract	v
Kur	zusammenfassung	vii
List	of Abbreviations	xi
1	Protein aggregation and the amyloid fold	13
1	•	
1.		
1	· · · · · · · · · · · · · · · · · · ·	
1.	Structural models of amyloid fibers	20
	1.4.1 Detailed molecular models of Aβ	21
	1.4.2 A structural model for α-synuclein	32
	1.4.3 Amyloid fibers made of large proteins: the example of Tau	
1.	• • • • • • • • • • • • • • • • • • • •	
1.	Summary of proposed amyloid structures	38
1.	Introduction to metal nanoparticles	39
1.	Overview of self-assembled monolayers and nanoparticles	40
1		
1	10 Amphiphilic gold nanoparticles: interaction with lipid bilayers	
1.	1 Conclusions	58
2	Using nanoparticles for amyloid research: statement of the problem	61
2.	· ·	
2		
2		
	v 1	
3	Interaction of charged gold nanoparticles and amyloid fibers	
3.		
3.		
3.		
3.	1	
3.	8	
3.	6 Conclusions	86
4	Discriminative adsorption of amphiphilic gold nanoparticles onto amyloid fibers	91
4		
4	Cryo-EM results with $A\beta_{1-40}$ : binding and non-binding conditions	92
4		
4		
4	·	
4		
4		
_	0.41.11.116.4	117
5	Outlook and future work	
5.	$\Gamma$	. 11/
5.		110
n 5	cleation	
	VV 1 V 1 1	
5. 5.		
5. 5.		
)		
Μ.	Methods	. 125

	Ligand synthesis	125
M.1		
M.1		
M.1	3 Synthesis of zwitterionic ligand	131
M.2	Nanoparticle synthesis and characterization	132
M.2	One phase allMUS and MUS:OT synthesis	133
M.2	2 Stucky allMUS and MUS:OT synthesis	134
M.2	3 Stucky synthesis of allTMA and ZW nanoparticles	134
M.2		
M.3 P	reparation of amyloid fiber experiments	141
M.3		
M 3	2 Aβ sample preparation and kinetic assays	142
M.3	3 $\alpha$ -synuclein fiber growth	144
M.3	· · · · · · · · · · · · · · · · · · ·	
1.1.0	1. 4	
	iectron microscopy of amyloid nanoparticle samples	145
	lectron microscopy of amyloid nanoparticle samples  1 Dry negative staining TEM	
M.3 E	1 Dry negative staining TEM	145
M.3 E	1 Dry negative staining TEM	145

#### **List of Abbreviations**

2D two-dimensional
3D three-dimensional
Aβ beta-amyloid protein
AD Alzheimer's disease
AFM atomic force microscopy

AM-AFM amplitude modulated atomic force microscopy

Au gold

AuNPs gold nanoparticles

AUC analytical ultracentrifugation
CHO chinese hamster ovary
DMF dimethylformamide
DMSO dimethysulfoxide
DNA deoxyribonucleic acid

DOPC 1,2-dioleoyl-sn-glycero-3-phosphocholine

EM electron microscope

Cryo-EM cryogenic electron microscopy
EPR electron paramagnetic resonance

H/D hydrogen-deuterium MD molecular dynamics

MHol hydrophilic 6-mercapto-1-hexanol
MUP 11-mercaptoundecylphosphoric acid
MUS 11-mercapto-1-undecanesulfonate

NaBH<sub>4</sub> sodium borohydride

NAC non-amyloid β component NMR nuclear magnetic resonance

ssNMR solid state nuclear magnetic resonance

NPs nanoparticles OT 1-octanethiol

PBS Phosphate buffer solution QCD quartz crystal microbalance

S sulfur

SAM self-assembled monolayers

SASA hydrophobic solvent exposed surface area

SLB Suspended lipid bilayer

STEM scanning transmission electron microscopy

STM scanning tunneling microscope
TEM transmission electron microscopy

ThT thioflavin T

TMA N,N,N-Trimethyl(11-mercaptoundecyl)ammonium Chloride

ZW NPs Zwitterionic nanoparticles

# 1 Protein aggregation and the amyloid fold

The results presented in this thesis cannot be rationalized without appreciating the background on protein aggregation. Moreover, amyloid fiber structural determination has become a field in itself: this chapter reviews the basic developments of the past 15 years, and provides the background to interpret the cryo electron micrographs discussed in chapters 3 and 4. It emphasizes, in detail, the structural models for A $\beta$  fibers, their variations and experimental constraints.  $\alpha$ -synuclein and Tau-441 fibers are briefly presented, and contextualized in the debate on amyloid pathogenicity, followed by a summary of what the surfaces of twisted ribbon amyloid fibers correspond to according to the literature.

### 1.1 Protein folding and misfolding in disease.

Living organisms are composed of a few classes of building blocks, such as lipids, nucleotides and amino acids. Despite the remarkable information-density and transmission reliability that nucleotides afford living organisms, life itself occurs as an expression of the coordinated functions encoded in the final shapes, forms and combinations of proteins. Unsurprisingly, the quest to understand protein structure to gain a glimpse of how they operate, and hope to correct their malfunction in disease, is a major undertaking in the scientific community<sup>1</sup>.

Anfinsen's dogma states that the primary structure of a polypeptide, in other words, the amino acid sequence, determines the final three-dimensional structure of the native protein<sup>2</sup>. This rationale implies a rugged funnel-shaped energy landscape, in which the native protein sits at the lowest free-energy state (Figure 1.1(a)). This landscape is evolutionarily favorable, because it allows multiple paths for the same ultimate function, which does not rule out potentially beneficial mutations. However, even under physiological conditions, proteins can adopt structures that depart from the native conformation. This observation does not contradict Anfinsen's dogma, but reveals that, depending on the conditions, polypeptides can fold and aggregate outside the free-energy minimum, as depicted in Figure 1.1(b). This figure shows a different energy landscape, in which the free-energy minimum is the aggregated state, that is avoided by the action of chaperones<sup>3,4</sup>. Whichever the landscape, protein aggregation occurs and its repercussions can be devastating.

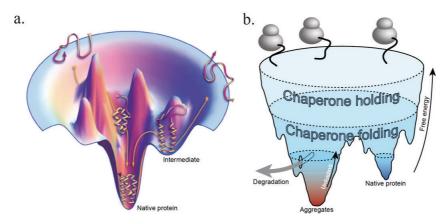


Figure 1.1 Proposed energy landscapes available for protein folding. (a) The rugged, multi-pathway landscape in which different paths lead to the native protein conformation depending only on the primary structure, regardless the route. Reused with permission from reference (1) Copyright© 2012 AAAS. (b) From reference (3) a different possibility for proteins prone to misfold, highlighting the role of chaperones to ensure correct folding, and the possibility of degradation for incorrectly arranged proteins.

A polypeptide chain, in its path to the native conformation, can undergo several energy-minimizing arrangements that deviate from the physiological route, placing it in front of a kinetic barrier. There are proteins called chaperones that act to correct and guide the polypeptide around kinetic barriers towards the native state (Figure 1.1(b)). The roles of chaperones go beyond navigating proteins through the rugged free-energy landscape, and include the redirection of faulty proteins to the proteasome system, where homeostatic degradation of discarded proteins take place<sup>5</sup>. Post-translational modifications add another layer of complexity to how proteins fold, and play a crucial role in establishing the native conformation<sup>6</sup>. Again, this does not directly contradict Anfisen's dogma, because the primary sequence of amino acids still determines how the post-translationally modified proteins adopt their three-dimensional conformation, therefore, how they operate.

Faulty protein causes disease through multifactorial pathophysiological mechanisms. The pathologies can be roughly categorized depending on the degree of known causality between misfolding and phenotype, in other words, how well-established the etiology is. First, mutations in the DNA sequence can lead to a loss of function or a gain of toxicity that deviates from homeostasis. In this category, Mendelian conditions such as Cystic Fibrosis (CB), a disease caused by a mutation in the gene for the chlorine channel *Cystic Fibrosis Transmembrane Conductance Regulator* (CFTR), culminates in a devastating condition marked by viscous secretions from epithelial tissues. The repercussions of this incorrect mucous production affects the respiratory and digestive systems, culminating in organ failure and death by obstructive lung failure in 80% of cases<sup>7</sup>. Despite a well-established etiology,

treatments for CB remain palliative. Sickle cell anemia is another example of an inherited faulty protein disease. When the  $\beta$ 6 glutamic acid in hemoglobin S (HbS) is replaced by valine, the solubility of deoxygenated HbS decreases, which causes the protein to aggregate inside the red blood cell<sup>8</sup>. These aggregates made of HbS fibers distort the shape of the erythrocyte into an elongated cell, hence the name of the disease, that causes a variety of vascular complications, and depending on the severity, culminates in death. Other Mendelian "misfolding" disorders include Huntington's disease and phenylketonuria<sup>9</sup>. The latter has recently been proposed to culminate in fibrous phenylalanine aggregation in the brain which can be one mechanism of toxicity. This finding illustrates that protein aggregation, and the damage it causes, can be downstream from a simple mutation in an enzyme.

In addition to these causally well-established genetic conditions that express faulty pathogenic proteins, a collection of other syndromes correlated to protein malfunction has been described. They can be triggered by defects in the chaperoning system and culminate in cataracts, retinopathy, inclusion-body myositis among other diseases<sup>11</sup>. Or they can be age-related multifactorial syndromes, often neurodegenerative, such as Alzheimer's disease<sup>12,13</sup> and Parkinson's disease<sup>14</sup>. Other neurodegenerative conditions are also related to protein malfunction, including progressive supranuclear palsy (PSP), frontotemporal dementia<sup>15</sup> and multiple-system atrophy<sup>16</sup>. Notably, the archetypical protein aggregation diseases are the Transmissible Spongiform Encephalopathies (TSEs) caused by aggregation of prion protein (PrP), that is capable of propagating its noxious aggregates across tissues, individuals and even species<sup>17</sup>.

Most of these diseases share one characteristic: the presence of proteins in the amyloid state. This type of protein fold is a common, stable structure correlated with about 50 human diseases<sup>18</sup>, and has become a field of study in itself. Difficulties to crystallize and determine high-resolution structural models for the amyloid state led to several attempts using Nuclear Magnetic Resonance (NMR) techniques in combination with Electron Microscopy (EM). This thesis shows, for the first time, that gold nanoparticles ranging from 1 to 4 nm in core diameter can discriminatively adsorb onto features of the amyloid fiber, depending on the type of monolayer that protects the particles.

#### 1.2 Definition of the amyloid fold

In 1854, Rudolph Virchow reported iodine-positive inclusions in brain samples that he believed were made of a starchy material, hence the name *Amyloid*, from the Latin and Greek words for sugar: *amylum* and *amylon* respectively<sup>19</sup>. Later, the proteinaceous nature of the inclusions was established, and currently, pathologists impose a stringent definition for amyloids. They are body tissue deposits of non-branching protein filaments, that bind the Congo-Red dye, and exhibit green-yellow birefringence under polarized light microscopy when stained<sup>20</sup>. The International Society of Amyloidosis (ISA) suggests the term amyloid-like for fibers prepared *in vitro* from natural or synthetic precursors<sup>20</sup>.

On the other hand, the biophysical definition of amyloid encompasses fundamental structural features common to all fibers, and is summarized as: protein fibers that display a cross-beta fiber diffraction pattern. Astbury first reported this structure in 1935, observing the diffraction pattern of stretched egg-white that showed ~4.7 Å and ~10 Å meridional and equatorial scattering respectively<sup>21</sup>. Similar diffraction patterns were later observed for fibers extracted from disease tissue deposits<sup>22</sup>, thus consolidating the definition of amyloids. Segments of the proteins (or entire peptides) adopt an extended beta-sheet conformation that stack parallel to one another and perpendicular to the fiber, giving rise to the ~4.7-4.8 Å meridional reflection. Identical layers of these beta-sheet supra-assemblies stack onto one another, producing the 6-11 Å equatorial diffraction bands, as illustrated in Figure 1.2.

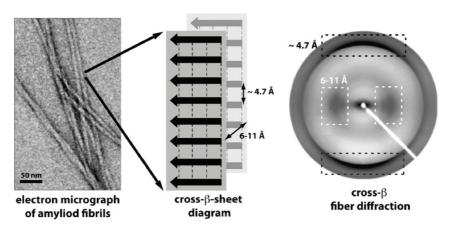


Figure 1.2 On the left, negatively stained TEM image of amyloid fibers. In the center, schematic view of how beta-sheet segments arrange in space, in the fiber core, followed by a typical fiber X-Ray diffraction pattern. From reference (23) reprinted with permission Copyright © 2010 Elsevier Ltd. All rights reserved.

Despite a constitutively simple motif, amyloid fibers pose a challenge for protein structure determination. High-resolution models of fibers made from disease-related proteins are

difficult to obtain: such polydisperse helical fibers have not yet been crystallized for X-ray diffraction. Most models rely on complex NMR approaches and mass density maps from EM images. This generates a gap between biological properties and the underlying fiber structures. Furthermore, it has been recognized that proteins correlated with devastating diseases, such as amyloid beta  $(A\beta)$  in the case of Alzheimer's disease, exist in several morphologies<sup>24</sup>, analogous to the different strains found in prion diseases. Recently, the crystallization of small peptide fragments, that also form amyloid fibers, has revealed a set of structural constraints, that likely underpin the fundamental design rules dictating how longer peptides and full proteins self-assemble into fibers<sup>25,26</sup>.

#### 1.3 Amyloid-like microcrystals

Amyloid fibers are unbranched twisted ribbons, 5 to 20 nm wide that span from tens of nanometers to a few microns in length. Different shapes, helical pitches, widths and symmetries can reflect all the possible ways the constitutive polypeptide monomers fold and subsequently arrange with respect to one another. To understand the different detailed molecular structural models proposed for amyloid fibers, it is convenient to begin with the reductionist approach taken by David Eisenberg's group. They have performed X-ray diffraction crystallography on short peptides that form both fibrils and microcrystals. A set of intermolecular arrangements was revealed by microcrystal X-ray crystallography which coincides with the basic fiber structure: care must be exercised to translate these findings to the fibers<sup>25-27</sup>.

The first microcrystal structure was determined for the 7-residue fragment derived from Sup35 yeast prion protein, GNNQQNY<sup>25</sup>. The microcrystal matched fundamental aspects of the crossbeta motif found in the fibers: the heptapeptides adopt a Pauling-Corey beta-sheet conformation, perpendicular to the long axis of the crystal, spaced by 4.87 Å. The unit cell is formed by complementary pairs of anti-parallel monomers (two heptapeptides) bound together by a dry interface of self-complementary, interdigitating side chains, termed steric zippers. These unit cells are related via a 2<sub>1</sub> screw axis, bound together by extended hydrogen bonds in the long axis (**b** axis in Figure 1.3(a)). Despite not being the structure of a full-length amyloid fiber, these results provide molecular insight to understand the lower resolution models proposed for fibers. Not all properties seen in the microcrystals translate to the fibers: for example, the facets and beta-sheets of the crystals are flatter than those reported on fibers<sup>28</sup>.

Nevertheless, the microcrystal structures offer invaluable insight to understand fiber polymorphisms and prion strains.

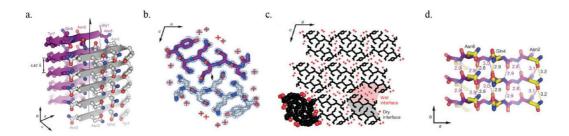
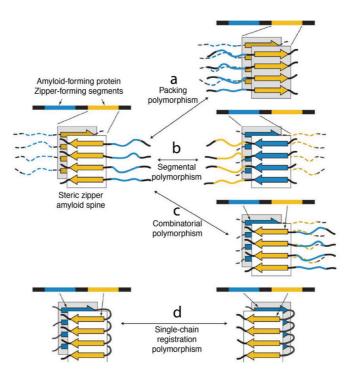


Figure 1.3 1.8 Å resolution crystal structure of a GNNQQNY microcrystal: space group P2<sub>1</sub>. Carbon atoms in purple or grey/white, oxygen red and nitrogen blue (a) Lateral view of the crystal highlighting the beta-sheet stacking in agreement with the biophysical definition of the amyloid fold. (b) A cross-sectional view of the peptide pair, highlighting the antiparallel nature, the self-complementary interdigitating side-groups coined steric zippers that form a dry interface (c) A view along the b axis on how the units in (b) pack in the a-c plane: note the wet interfaces between the faces of the peptides not committed to steric zipper (d) The hydrogen bonding network between adjacent in-register parallel beta sheets. Adapted with permission from reference (25) Copyright© 2005, Rights Managed by Nature Publishing Group.

To date, dozens of amyloid-like microcrystal structures have been determined by X-ray crystallography<sup>26,29,30</sup>. These structures reveal how short amyloid-forming peptides can selfassociate in different patterns, giving rise to the possible root of amyloid polymorphism and prion strains<sup>26</sup>. Briefly, as depicted in Figure 1.4(a), a peptide pair can undergo a shift in registry, in other words, how two neighboring peptides stack relative to one another, which creates different steric zippers. They can also combine in a parallel or antiparallel fashion, depending on the crystal-formation conditions. These possibilities have been aptly named packing polymorphisms, whereby the relative arrangement between the two monomers varies in orientation and registry. When different segments of the peptide form steric zippers, as in Figure 1.4(b), the polymorphism is called **segmental**. So far, only these two types of polymorphisms have been described in amyloid-like microcrystals. If different segments from two separate molecules (Figure 1.4(c)), or within the same polypeptide chain (Figure 1.4(d)) form heterosteric zippers, in other words, non-homologous interdigitations, the variations are called **combinatorial** and **single-chain registration polymorphism** respectively. The latter constitutes the ubiquitous U-shaped monomer found in several detailed structural models derived from multidimensional NMR techniques<sup>28,31,32</sup>.



**Figure 1.4** Schematic view of molecular scale polymorphisms. **(a)** Packing polymorphism. **(b)** Segmental polymorphism. **(c)** Combinatorial polymorphism. **(d)** Single-chain registration polymorphism. The last two types of polymorphisms have never been determined at high resolution, but (d) is commonly reported in amyloid fibers made of long peptides. Reprinted with permission from reference (26) Copyright © 2009, Rights Managed by Nature Publishing Group.

The microcrystals cannot capture all aspects of the amyloid state and prion propagation. Nonetheless, they offer crucial guidelines that might underlie the formation of the spines that define the fibrous species. The decrease in entropy upon formation of ordered fibers and microcrystals poses a barrier to their formation. The enthalpic gain upon formation of the extended beta-sheet hydrogen bonding network is not sufficient to offset the entropic loss. The new hydrogen bonds do not significantly outnumber the water-amide bonds in the soluble form, however, the complementary interdigitation between the amino acid side groups confer a significant decrease in enthalpy through van der Waals forces. In other words, the formation of the steric zippers may be the main driving force for the nucleation and propagation of amyloid-like structures. Once formed, the hydrogen bonding network on the amyloid fiber is remarkably robust because of dipole induction: however, unlike the steric zippers, this added strength is not considered a driving force to form the amyloid structure<sup>25</sup>.

The steric zipper may also be the molecular mechanism behind protein-encoded inheritance, whereby different conformations of prion proteins can propagate their own strain<sup>29</sup>. An analogous observation has been made for amyloid fibers of  $A\beta_{1-40}$  extracted from cadaveric brain tissue of AD patients. Different polymorphs were found in separate patients, and the

correlation between disease severity and amyloid morphology, a well-known phenomenon for prion strains, is now under close scrutiny for non-prion amyloid diseases as well<sup>33</sup>. The idea that molecular information can be encoded and transmitted by a protein conformation is new, and has even led to an intriguing speculation of a pre-biotic world, when prion-based life existed through the selection of sequences that fit a given conformation. In other words, the cross beta sheet motif would be an "ancestor" fold under this hypothesis, and the steric zipper acts as the information propagating unit in such 'amyloid world'<sup>34</sup>. The recent reports of functional amyloids<sup>35</sup>, for example the storage of pituitary peptide hormones in this conformation<sup>36</sup> reveal that organisms do take advantage of what was otherwise considered a mere pathognomonic finding.

#### 1.4 Structural models of amyloid fibers

Despite the enormous contributions that microcrystal atomic resolution models have warranted the field, full length fibers lack the same level of structural resolution. Amyloid fibers have not yet been crystallized, and even if a crystal is obtained, it will likely contain only a particular polymorph. Amyloid fibrils tend to be polydisperse, that is, vary in length and width, and also polymorphic through diverse self-associations between the building blocks. Furthermore, they are inherently non-crystalline and insoluble, which render them recalcitrant to structural determination, not only via conventional crystallography, but also through standard multidimensional solution NMR techniques. Figure 1.5 shows fibers made *in vitro* from three different polypeptides associated with neurodegenerative diseases. Figures 1.5(a) and (b) depict  $A\beta_{1-40}$  fibers imaged under Atomic Force Microscopy (AFM) and negatively stained EM respectively. Figure 1.5(c) is an EM image of Tau-441 in the fibrillar state and Figure 1.5(d) shows  $\alpha$ -synuclein fibers. Different types of fibers clearly co-exist in the same sample.

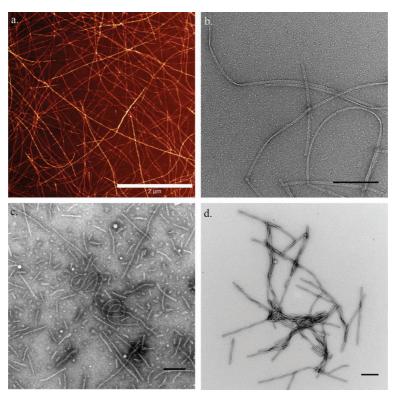


Figure 1.5 (a) Atomic Force Microscopy (AFM) image of mature  $A\beta_{1-40}$  fiber (Bruker, 40 N/m cantilever) (b) The same fibers imaged under negatively stained preparation for Transmission Electron Microscopy (TEM) (c) Wild-type full Tau-441. (d)  $\alpha$ -synuclein fibers. EM scale bars represent 200 nm and AFM 2  $\mu$ m. All EM images were obtained in an FEI TALOS<sup>TM</sup> Electron Microscope in bright-field mode.

#### 1.4.1 Detailed molecular models of AB

Several groups have used solid state NMR (ssNMR) and EM as constraints to propose detailed structural models of Aβ fibers, which are strongly correlated with Alzheimer's disease<sup>37</sup>. Other techniques including X-ray diffraction, electron paramagnetic resonance (EPR) and hydrogendeuterium (H/D) exchange in solution NMR along with mass spectrometry have helped produce detailed models. Nevertheless, ssNMR has yielded the most precise structural models, and is a powerful technique to study, not only amyloids, but also membrane proteins and dynamic aspects of these macromolecules<sup>38</sup>. A detailed technical background on ssNMR escapes the goal of this thesis, however the different detailed models proposed by NMR groups are essential to interpret the data in chapters 3 and 4. Therefore, it is imperative to briefly review these results and how they relate to the fundamental rules established by the amyloid-like microcrystal structures. The nomenclature for models established via X-ray diffraction and ssNMR varies: when the term structure is used, it denotes atomic resolution models derived from X-ray diffraction patterns. Because the resolution of ssNMR models is lower, the term detailed structural model is preferred. The resolution of these models span from 2.1 to 2.7 Å

based on root mean squared deviations of backbones and heavy atoms<sup>39</sup>. Ultimately, both approaches produce models that differ in their proximity to reality: henceforth the term model will be used interchangeably throughout this text.

Similar to microcrystal structural determination, early ssNMR studies focused on fragments of disease-related amyloid-forming proteins and peptides. In the early 90's, Griffin and then Lansbury published the first ssNMR of  $A\beta_{34-42}$ , a nonapeptide from the  $A\beta$  sequence<sup>40,41</sup>. Their results confirmed the cross beta sheet motif revealed by fiber X-ray diffraction, and showed that these nonapeptides adopt an anti-parallel conformation. As ssNMR researchers increased the length of the polypeptides, the cross beta sheet arrangement was consolidated, but different organizations between the monomers were found. For example, the model obtained for  $A\beta_{10-10}$  revealed parallel beta-sheets<sup>42</sup>, which became the most common arrangement found in  $A\beta_{10-10}$  and  $A\beta_{10-10}$  These different arrangements found by early ssNMR studies fall under the category of packing polymorphisms, shown in Figure 1.4(a).

After initial attempts to determine key aspects on how polypeptides self-associate to form amyloid fibers, 3D detailed molecular models for these materials were proposed. Notably, Robert Tycko's group published a model for  $A\beta_{1-40}^{44}$ , and later revealed that, depending on experimental conditions, different morphologies can self-propagate<sup>31</sup>. This finding demonstrated the existence of polymorphs that can recruit monomers to adopt a particular three-dimensional conformation through a mechanism similar to prion strains. When  $A\beta_{1-40}$  monomers were prepared under quiescent or agitated conditions, 3-fold or 2-fold symmetric structures were obtained, respectively<sup>28</sup>. Figure 1.6 illustrates the quiescently grown 3-fold symmetric fibers and the agitated 2-fold ribbons. These ssNMR models established the U-shaped or hairpin monomer model, in which the  $A\beta_{1-40}$  chain has two domains in a beta-sheet conformation, linked by a loop, establishing the the beta-turn-beta unit. Further studies showed that monomers can form multiple beta-sheet domains in the primary sequence and fold in a serpentine-like fashion alternating multiple beta-turn-beta segments: this superpleated structure is likely obligatory for larger amyloid-forming proteins<sup>45</sup> and has been described for certain preparations of  $A\beta_{1-42}^{46}$ .

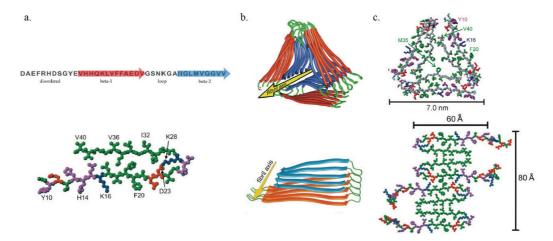


Figure 1.6 (a) The sequence of  $Aβ_{1-40}$  and the segments that adopt an extended beta-sheet conformation: beta-1 from residues 12 to 24 and beta-2 from 30 to 40. Possible segmental polymorphisms can cause variation in these domains. (b) Beta-turn-beta hairpin schematic model for monomers prepared under quiescent (top) and agitated (bottom) conditions. The 3-fold symmetric rendition is plausibly the accurate combinatorial geometry of the monomers, whereas the 2-fold symmetric shows only one layer, which is denoted protofilament. (c) Transection of the molecular backbone for both quiescently prepared fibrils (top) and possible lateral interactions for 2-fold symmetric protofilaments, with the first 10 N-terminal residues in a random coil conformation. Reproduced and adapted from references (44) and (28) Copyright© by the National Academy of Sciences.

Solid state NMR provides constraints that, combined with EM, enable the calculation of an energy-minimizing model of the peptides in 3D. Materials that cannot be characterized via conventional crystallography can be determined using this approach. Moreover, protein crystallography reveals the state of the macromolecule in its crystalline form, whereas spectroscopic techniques can capture the thermal fluctuations and less ordered native components. In the models proposed in Figure 1.6, residues 1 through 8 were deemed disordered, therefore omitted from the simulation. The loop is stabilized by a salt bridge between the positively charged lysine at position 28 (K28) and aspartic acid at 23 (D23). Other polar residues sit in the omitted N-terminal tail, on the outside of the beta-1 strand (notably another lysine at position 16) and on the outside of the loop. The remaining residues are hydrophobic (green in Figure 1.6(a)), especially in the beta-2 strand (residues 30 to 40) that can establish strong hydrophobic pairings with a homologous strand<sup>44</sup>. The amino acid side chain contacts in the interior of the hairpin model is reminiscent of the steric zippers described for amyloid-like microcrystals. For example, glutamine at position 15 (Q15) establishes a contact with the hydrophobic pocket formed by glycines 37 and 38 (G37 and 38): this, along with all contacts inside the hairpin, constitute a heterostatic steric zipper as defined for amyloid-like microcrystals (Figure 1.4(d)).

Despite the structural difference between 3 and 2-fold symmetric  $A\beta_{1-40}$  fibers (Figures 1.6(b) and (c)) the basic building block is, to a first approximation, identical. Subtle differences in

residue-residue interactions were reported: for example, the salt bridge between D23 and K28 for the 2-fold symmetric monomer occurs inside the hairpin at a 0.37 nm distance, whereas this gap is 0.5 nm for the monomers sitting on a 3-fold fiber. Nonetheless, both polymorphs are made of remarkably similar hairpin monomers that self-associate in-register with a cross-beta motif. The main differences are the overall symmetry, the contacts established between the homologous beta-strands and perhaps the disordered segments<sup>28</sup>.

The 3-fold symmetric species has a higher mass-per-length value (~27 kDa/nm) than the 2-fold type (18 kDa/nm), however, the rate of monomer addition to the ends of the different fibrils does not scale in a 3:2 ratio. On the contrary, the elongation and shrinkage rates ( $k_e$  and  $k_s$ ) are indistinguishable at 37°C, but the elongation rate at 24°C is higher for 2-fold symmetric fibers. Therefore, a direct correlation between structure and kinetic properties may not exist<sup>47</sup>. At 24°C the 2-fold species is more stable than the 3-fold by 0.8 kcal/mol, but this difference is below the detection limit at 37°C<sup>47</sup>. So far, the only properties that seem to be structure-dependent are the higher propensity of 2-fold fibers to fragment under shear stresses<sup>47</sup> and the higher *in vitro* toxicity of 3-fold fibers<sup>31</sup>. The former can explain the prevalence of 2-fold species in agitated preparations and the interconversion towards this morphology when both species co-exist. During sample preparation, the 2-fold symmetric fibers break and form nuclei that outnumber the 3-fold species, eventually becoming the dominant morphology via monomer exchange. Structural interconversion from one morphology to another has not been reported and is an unlikely phenomenon due to the high energy penalty to reorganize the structure. It is unlikely that the minor thermodynamic stability of the 2-fold morphology is the driving force behind its prevalence in experimental preparations.

Other groups have published different detailed structural models of  $A\beta_{1-40}$  using the same approach <sup>48,49</sup>, and reported slightly different models. Given that the same group obtains controllably different polymorphs at 24°C by tuning agitation, it is not surprising that different sample preparations produce distinct molecular arrangements. Figure 1.7 summarizes the relevant detailed molecular structures of  $A\beta_{1-40}$  obtained by two groups using ssNMR, highlighting their distinct intra and intermolecular contacts. Figure 1.7(c) depicts the model obtained by Bertini et. al. that, in addition to the beta-turn-beta monomer, has a segment of the otherwise disordered N-terminal in a beta-sheet conformation. This segmental polymorphism involves residues 4 through 7 that form a beta sheet ( $\beta_n$ ), followed by a kink prior to beta-1 that

starts at residue 11. The  $\beta_n$  segment might be related to the biological relevance of the N-terminal portion of  $A\beta^{48}$ . These models can be found in the protein database under 2LMN, 2LMO, 2LMP, 2LMQ.

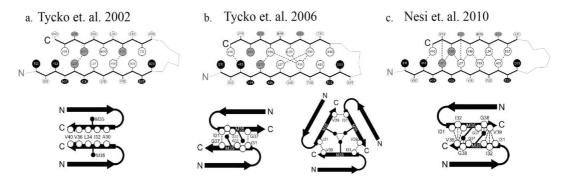


Figure 1.7 White dots represent hydrophobic residues, black acidic or basic and grey other types (a) Detailed molecular structure of  $A\beta_{1-40}$  in which position 35 methionine (M35) points into the hairpin space. Two protofibrils associate via parallel contacts between C-terminal beta-2 strands<sup>44</sup>. (b) The 2006  $A\beta_{1-40}$  model, with M35 facing outwards, and defining the contacts in the 3-fold symmetric polymorph, whereas the 2-fold stacks two homologous beta-2 strands anti-parallel to one another. While G37-I31 contacts define the 2-fold polymorph beta-2 contacts, V39-I31 stabilizes the beta-2 contacts in the 3-fold version<sup>28</sup>. (c) An  $A\beta_{1-40}$  model for an agitated preparation at 37°C reveals different beta-2-beta-2 contacts and a beta-sheet segment on the N-terminal, otherwise, amorphous segment. Adapted with permission from reference (48) Copyright © 2011, American Chemical Society.

Unlike *in vitro* preparations, different parts of a single human brain did not present  $A\beta_{1-40}$  fiber polymorphism, but fibers obtained from two different AD patients did<sup>33</sup>.  $A\beta_{1-40}$  fibers were extracted from different parts of cadaveric brain tissue of two patients with different clinical presentations. Each fiber morphology depended on the patient and not on the anatomical origin within the brain. In other words, at that stage of the disease, the mature fibers had a uniform morphology throughout the organ, which may be due to a common nucleation instance that imposed a particular structure. Both samples showed the hallmarks of 3-fold symmetric fibers, but the seeded fibers from only one patient had a good enough ssNMR spectrum for the calculation of a 3D detailed structural model. The resulting model, shown in Figure 1.8(c), differs from those obtained *in vitro*, but contains an overall 3-fold symmetry and a 28 kDa/nm mass per length density. The D23-K28 salt bridge is present with a 0.35 nm distance, similar to the 2-fold symmetric *in vitro* fiber. However, the N-terminal contains a beta-stretch, similar to Bertini's  $\beta_n$ , and the conformation of the beta-1 and 2 segments is more intricate than its *in vitro* counterparts. Nonetheless, the peptide adopts roughly a hairpin conformation instead of a serpentine-like superpleated structure.

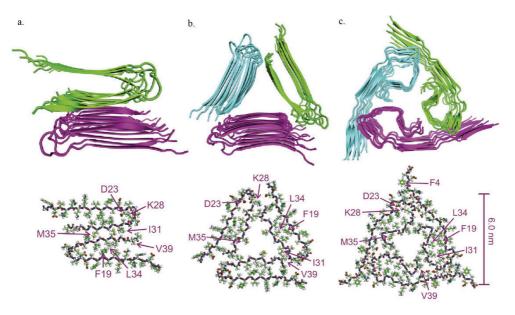
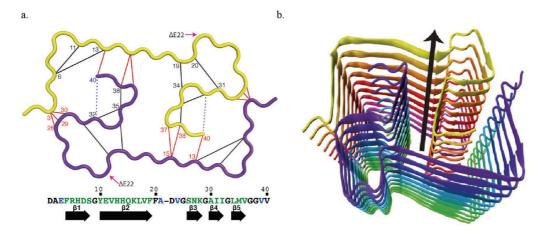


Figure 1.8 Differences between *in vitro* and human brain derived  $Aβ_{1-40}$  fibers: the D23-K28 salt bridge is tight both in the 2-fold symmetric *in vitro* fibers and in the human derived fibers. (a) Detailed molecular structure of  $Aβ_{1-40}$  prepared *in vitro* at 24°C with agitation (PDB 2LMN): (b) Quiescently grown fibers displaying a 3-fold symmetry (PDB 2LMP). (c) Detailed model for fibers produced by seeding with brain derived tissue from an AD patient. Notably, no polymorphisms were found inside the same brain, but between two different brains, the ssNMR spectra revealed structural differences that can correlate with clinical presentation. Adapted with permission from references (24) Copyright © 2015 Elsevier Inc. All rights reserved and (33) Copyright © 2013 Elsevier Inc. All rights reserved.

This cross-patient polymorphism reveals a complex landscape for  $A\beta$  toxicity. Not only the aggregation process and its associated oligomers can be toxic, but also specific conformations may respond for different clinical presentations. In addition to wild type  $A\beta$ , the strong correlation between certain mutations and early onset familial types of AD (FAD) ties a close link between  $A\beta$  and the disease. Several mutations have been described, many of them surrounding the glutamic acid (E) at position 22 of the  $A\beta$  sequence. For example, the Arctic, Dutch and Italian mutations replace E22 with a glycine, glutamine and a lysine respectively.

Recently, a model of the Osaka mutant<sup>50</sup> fiber containing a deletion of E22 (E22 $\Delta$ A $\beta_{1-40}$ ) has been proposed using ssNMR<sup>51</sup>. Figure 1.9 depicts the proposed structure, in which K28, instead of establishing a salt bridge with D23, does so with the glutamic acid at position 3 (E3) of its homologous pair. In this morphology isoleucine 32 interacts with valine 40 (I32-V40), which disrupts the otherwise beta-2 stretch forcing it to kink outwards. Therefore, instead of a U-shaped monomer, the peptide adopts a serpentine-like conformation that pairs with its homologous counterpart. The distinctive morphology of *in vitro* E22 $\Delta$ A $\beta_{1-40}$  fibers is not necessarily due only to the E22 deletion, but may also result from sample preparation conditions: it is most likely a consequence of both.



**Figure 1.9** Detailed structural model for Osaka mutant  $E22\Delta A\beta_{1.40}$  fibers. (a) Backbone model showing important inter and intramolecular contacts. Notice the departure from the simple U-shaped monomer as the I32-V40 contact forces the otherwise beta-2 strand in wild type  $A\beta_{1.40}$  fibers to bend inwards. Residues from 30 to 40 are then broken into three beta sheet segments, connected by kinks. (b) Configuration of 20 monomers of  $E22\Delta A\beta_{1.40}$  in 3D defining the protofibril of this mutant. A mature fiber is likely made of multiple intertwined structures like this one. Reproduced and adapted with permission from reference (51) Copyright© 2014 The Authors. Published by Wiley-VCH Verlag GmbH & Co.

Another important mutation that contributes to the current understanding of detailed structural models for  $A\beta_{1-40}$  is the replacement of aspartic acid at position 23 with an asparagine (D23NA $\beta_{1-40}$ ). This substitution known as the Iowa mutation was found in kindred patients who presented severe brain lesions, marked by a devastating cerebral amyloid beta-protein angiopathy (CAA)<sup>52</sup>. This mutant revealed the existence of anti-parallel beta sheets along the fibril axis, which can be called an intermolecular registration polymorphism, following the nomenclature established for amyloid-like microcrystals<sup>53</sup>. Figure 1.10 shows the detailed structural model obtained for this fiber, in which hydrophobic contacts inside the U-shaped monomer stabilize the peptide. Up to residue 16, the peptide is disordered, followed by beta-sheet stretches between residues 17-21 and 31-35: these rigid segments are united in a U-shaped monomer via hydrophobic contacts of residues 17, 19, 21, 30, 32, 34 and 36<sup>54</sup>.

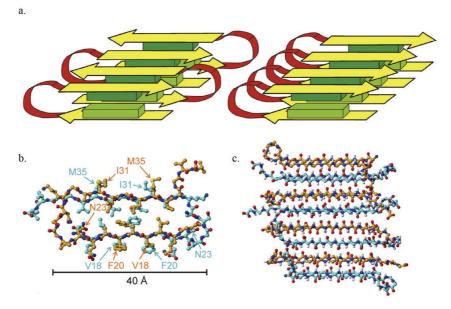


Figure 1.10 (a) On the left, a schematic view of a D23NA $\beta_{1-40}$  protofibril in antiparallel stacking. On the right, a rough model of the typical parallel protofibril found for wild type  $A\beta_{1-40}$ . Green boxes represent hydrophobic contacts, analogous to the heterosteric zippers proposed for amyloid-like microcrystals (b) (PDB 2LNQ) Molecular view of two (front orange, back blue) Iowa mutant monomers and the orientations of amino acid side groups. (c) A molecular backbone rendition of how the monomers pack relative to one another on a mature fiber: four monomers associate to form the fiber. Two layers are shown; therefore 8 monomers are depicted in 3D. Adapted from reference (54) with permission from the authors.

The Iowa mutant structure raises profound questions on how full length proteins and peptides pack along the fiber axis in the amyloid state. It is commonly held that amyloid fibers are defined by an in-register, parallel beta-sheet conformation, in which rigid segments are spaced by ~4.8 Å. The satisfaction of hydrophobic interactions that drive amyloid formation was proposed to be maximized in this parallel in register arrangement<sup>43</sup>. However, antiparallel intermolecular packing has been described for short peptides in the crystalline form<sup>55,56</sup> and for fibers made of short Aβ fragments 41,57. The argument for parallel arrangements rests largely on a two-dimensional interpretation of beta-sheet interconnectivity<sup>43</sup>, and contradicts the antiparallel findings of short segments which are, to a first approximation, two-dimensional (i.e. flat). Nonetheless, this argument has agreed with all models proposed for several larger proteins and peptides<sup>58,59</sup> until the model proposed for D23NA $\beta_{1-40}$  was published. The authors propose that the antiparallel version is thermodynamically metastable, because mixtures of both fibers culminate in the parallel conformation, via monomer exchange. It also indicates that the nucleation rate of less structured, anti-parallel D23NA $\beta_{1-40}$  oligomers is higher than that of parallel structures. This suggests that certain nuclei or oligomers can have an antiparallel conformation, which are challenging to isolate and study, but can be related to oligomeric toxicity<sup>54</sup>. Regardless the intricacies, this finding questions the paradigm of in register parallel beta sheets in mature fibers, and points towards less structured oligomers with a degree of antiparallel arrangement<sup>56</sup>, which in turn can have higher surface tension following classical nucleation and growth theory.

In addition to  $A\beta_{1-40}$  fibers, several other amyloidogenic peptides have been carefully studied. Each system poses its own experimental challenges: for example, two additional residues, isoleucine and alanine at positions 41 and 42, extend the  $A\beta$  molecule to its  $A\beta_{1-42}$  version that is less water soluble, thus more prone to aggregation. It is safe to assume that  $A\beta_{1-42}$  presents the same, if not greater, polymorphic behavior as the 40-residue species. The attempts to determine detailed structural models of  $A\beta_{1-42}$  fibers confirm this trend. Although hairpin U-shaped monomers<sup>32,60</sup> have been observed for  $A\beta_{1-42}$  fibers, recent works reveal superpleated serpentine-like monomeric arrangement<sup>61</sup> (Figure 1.11(a) and (b) respectively).

The earliest, and perhaps best-known A $\beta_{1-42}$  model was not obtained from ssNMR, but rather through quenched hydrogen-deuterium (H/D) exchange in solution-based NMR, along with mutagenesis and careful cryo-electron microscopy (cryo-EM). The model proposed by Lührs et al. revealed a disordered N-terminal up to residue 17, followed by two beta-sheet stretches (beta 1 and 2) connected by a loop that spans residues 26 to 30. This model resembles the A $\beta_{1-40}$  models, but displays key differences: namely the K28-D23 salt bridge that stabilizes the turn is intermolecular. In other words, the lysine 28 in molecule i establishes a salt bridge with the aspartic acid 23 of the neighboring molecule i+I. Figure 1.11(b) shows a remarkable image obtained in this work: a 3D model of a mature fiber, made of 4 protofilaments was built to scale, and the image was rendered in a blurred grey scale with 2 nm resolution. Then, they acquired negatively stained cryo-EM images of the fibers using ammonium molybdate to increase the electron density of the aqueous medium. The images obtained (Figure 1.11(b)) reveal discrete intertwined lines that the authors interpret as single protofilaments<sup>32</sup>.

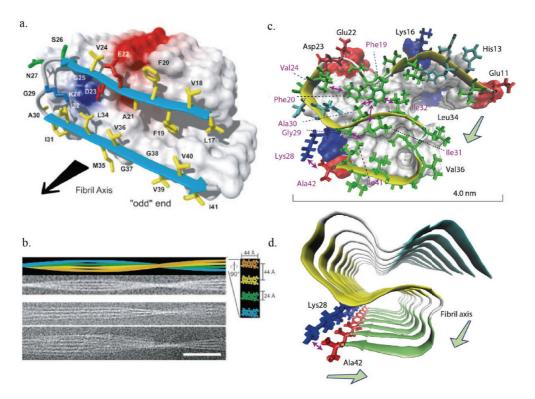


Figure 1.11 Different detailed structural models for  $Aβ_{1-42}$ . (a) (PDB 2BEG) A U-shaped model obtained through H/D exchange in solution NMR, mutagenesis and EM. (b) Simulation of a full fiber made of four protofibrils and the corresponding gray-scale rendition, and two examples of negatively-stained cryo-EM images showing remarkable similarity (scale bar 50 nm) (c) (PDB 2MXU) van der Walls surface rendition of S-shaped  $Aβ_{1-42}$  structure showing intramolecular contacts. Green side chains are hydrophobic. (d) View of in register parallel S-shaped monomers down the fibril axis, highlighting the unique K28-A42 salt bridge. Adapted with permission from references (32) Copyright© by the National Academy of Sciences and (61) Copyright© 2015, Rights Managed by Nature Publishing Group.

Detailed structural models of  $A\beta_{1-42}$  have been proposed using ssNMR by other groups  $^{46,60,61}$ . Similar to  $A\beta_{1-40}$ , separate groups have found different structures, however polymorphs were not reproducibly created and distinguished form one another, as done by Tycko and coworkers<sup>28</sup>. A recent model shows  $A\beta_{1-42}$  in a conformation that resembles the Osaka mutant shown in Figure 1.9: instead of the usual U-shaped monomer, the peptide adopts an S-like superpleated shape<sup>61</sup>. Three beta-sheet domains encompass residues 12-18 ( $\beta_1$ ), 24-33 ( $\beta_2$ ) and 36-40 ( $\beta_3$ ), which adopt a serpentine-like conformation relative to one another. Figures 1.11(c) and (d) show different representations of this structure, next to the U-shaped conformation proposed by Lührs et al. for comparison. The distinguishing feature of this configuration rests on the salt bridge between lysine 28 and the C-terminal carboxyl group of alanine 42. Such interaction has never been reported for  $A\beta_{1-40}$  and is somewhat surprising given the availability of other negative charges such as glutamic acid 3 in the disordered N-terminal. All other intramolecular stabilizing hydrophobic contacts are shown in Figure 1.11(c) with dotted lines.

 $A\beta_{1-42}$  fibers that adopted this conformation could not seed the growth of  $A\beta_{1-40}$  fibers with the same structure. The authors concluded that a structural requirement prevents cross-seeding between the two different types of  $A\beta$ : once a structure is formed, only peptides exactly congruent with the constitutive fiber monomers are able to join the conformation, which can explain the self-recognition of the amyloid state as discussed in the common ancestor hypothesis<sup>34</sup>. However, cross-seeding between  $E22\Delta A\beta_{1-40}$  (Osaka mutation) fibers and wild type  $A\beta_{1-40}$  showed that fibers made of the 39-residue mutant can seed the growth of wild-type  $A\beta_{1-40}^{62}$ . Whether the wild-type peptide adopts the 3D structure of the mutated version remains unknown.

In summary, the polymorphic nature of beta-amyloid (A $\beta$ ) peptides has been exhaustively characterized in the literature, and its structure-property relationships are far from being resolved. Rather than experimental error or inaccurate data interpretation, these different conformations for the same molecule reflect a complex energy landscape with several local minima. Depending on the exact conditions of sample preparation, the peptides adopt conformations with marginally different free energies<sup>47</sup>. Figure 1.12 illustrates several different *in vitro* detailed structural models for A $\beta_{1-40}$  and A $\beta_{1-42}$ . The arrows indicate the segments in a beta-sheet conformation, and as described in the amyloid-like microcrystal section, independent groups have studied different segmental polymorphism available to this sequence. Different segmental polymorphs can translate into markedly distinct 3D structures, which explains the diversity of fibers observed in a sample.

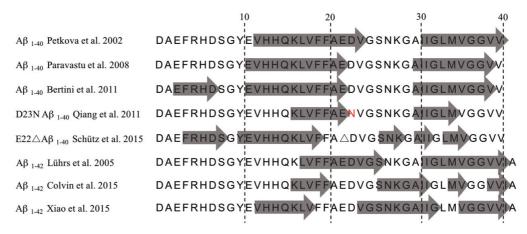


Figure 1.12 List of important segmental polymorphisms proposed by different groups in the past 15 years for the A $\beta$  sequence. All models are established by modelling the peptide under the constraints imposed by ssNMR and EM, except the Lührs et al. 2005 model that relied on a H/D exchange experiment.

#### 1.4.2 A structural model for α-synuclein

Synucleins ( $\alpha$ ,  $\beta$ , and  $\gamma$ ) are abundant in the pre-synaptic terminals of the central nervous system<sup>63,64</sup>. Their exact function is not fully understood, but they may play a role in synaptic plasticity and vesicle recycling<sup>65</sup>.  $\alpha$ -synuclein is the most abundant fibrillar species in the Lewy bodies found in dopaminergic neurons (and other types of neurons) of Parkinson's disease (PD) patients<sup>14</sup>. Mutations and overexpression of  $\alpha$ -synuclein results if familial, early-onset forms of PD, which reveals the possible causative role of this protein<sup>66</sup>.  $\alpha$ -synuclein is also found as an amyloid in the senile plaques of AD patients, and is correlated to different diseases, such as dementia with Lewy bodies, multiple system atrophy among others, collectively grouped as synucleopathies<sup>67</sup>.

The amino acid sequence of  $\alpha$ -synuclein can be separated into three regions: (i) the N-terminal region from residues 1 to 60 is amphipathic; (ii) the central region between 61 and 95, called the non-amyloid beta component (NAC), consists of a hydrophobic segment prone to beta sheet formation; and (iii) the C-terminal that contains several acidic amino acids, which gives  $\alpha$ -synuclein a net-negative charge in neutral pH. Figure 1.13(a) schematically depicts the sequence of  $\alpha$ -synuclein, showing these three main subdivisions. Although idiopathic PD remains unclear, several mutations, mostly in the N-terminal segment, have been reported to correlate with familial early-onset PD: for example, as shown in Figure 1.13(a), if threonine replaces alanine at position 53<sup>68</sup>, the disease manifests early, as an autosomal dominant trait in the families that carry the mutation. Several other point mutations in addition to gene duplication and even triplication renders the syndrome an autosomal dominant trait of how  $\alpha$ -synuclein is expressed<sup>14</sup>.

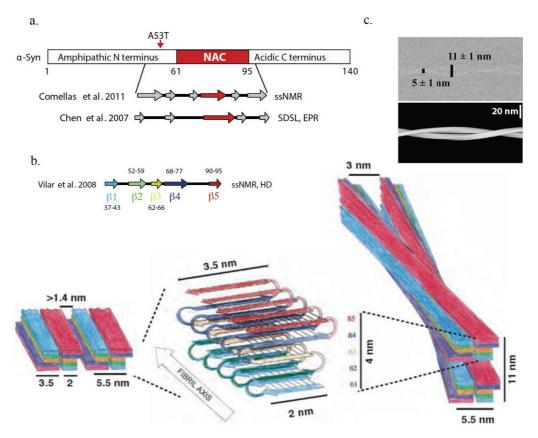


Figure 1.13 Possible structural constraints for α-synuclein. (a) Schematic subdivisions of the primary structure of α-synuclein, highlighting: the amphipathic N-terminal; the hydrophobic central part (NAC); and the negatively charged acidic C-terminal. The site of a mutation A53T is shown: most reported pathogenic mutations occur in the N-terminal. Two segmental polymorphisms for α-synuclein fibers reported by different laboratories are shown. (b) In a third model for α-synuclein in the amyloid state, the authors proposed a 3D model for the fiber. (c) Cryo-EM of twisted filaments and a 3 nm resolution model of it. The mature fiber structure was proposed using constraints from, H/D exchange experiments, ssNMR and cryo-EM. The cross-section of one of their proposed structures contains 4 beta-arcade monomers: in this model, the edge of the twisted fiber, which also corresponds to the thinnest diameter at the node (5 ± 1 nm) is made of solvent exposed beta sheets. This figure is adapted with permission from references: (30) Copyright © 2015, Rights Managed by Nature Publishing Group and (69) Copyright© by the National Academy of Sciences.

Figure 1.13 shows the general structural features that have been reported for  $\alpha$ -synuclein. Several groups have used the same techniques described for A $\beta$  molecular structure determination for  $\alpha$ -synuclein fibers with some degree of success<sup>59,69-71</sup>. Due to its length, several segments can adopt a beta sheet conformation, interconnected by loops, giving rise to a beta-arcade superpleated monomer. Figure 1.13(b) shows the structure proposed by Vilar et. al<sup>69</sup>, containing five beta-strands, that fold onto one another, establishing four heterosteric zippers that hold the monomer together. They found that the amino acid side-chains in the beta-1 and beta-5 strands were more solvent-exposed than those sitting at beta-2, 3 and 4. They proposed a 3D model of a mature fiber, in which the cross-section contains four beta-arcade monomers in several possible arrangements. Through careful cryo-EM analysis, they observed both flat fibers that did not twist and the ribbon-like structures depicted in figure 1.13(c). The

largest width of a twisted fiber was  $11\pm1$  nm, and the narrowest knot  $5\pm1$  nm (see Figure 1.13(c)). The peptide used to obtain the data that support this model is the fragment from residues 30 to 110: it contains the core fiber forming domain of  $\alpha$ -synuclein, and likely represents how the full-length  $\alpha$ -synuclein arranges in the amyloid state. Although segmental polymorphisms have been shown by other groups, the way beta-arcade monomers self-assemble to form a twisted fiber probably follows a structure similar to Figure 1.13(b).

If we approximate the object imaged under cryo-EM in Figure 1.13(c) to a twisted ribbon, according to their model, the edges of this ribbon correspond to solvent-exposed beta sheets. In other words, the smallest dimension of the twisting object is the length of two combined beta sheet surfaces: beta-1 and beta-5 (blue and red in Figure 1.13) establish an extended surface 5.5 nm wide. These two surfaces are always separated by about 11 nm, which means that the other, longer surface, of the twisted ribbon is made of loops and the disordered segments that protrude outwards from the fiber core.

#### 1.4.3 Amyloid fibers made of large proteins: the example of Tau

Another pathognomonic amyloid is found in the paired helical filaments (PHFs) formed by Tau, a microtubule-associated protein that plays an important role in axonal growth and function  $^{15,72}$ . The PHFs are intracellular amyloids that aggregate as neurofibrillary tangles (NFTs), one of the hallmarks of AD, along with the senile plaques and cerebral amyloid angiopathy  $^{73}$ . Like  $\alpha$ -synuclein, Tau is associated with a collection of neurodegenerative diseases that include Pick's disease, sporadic corticobasal degeneration, progressive supranuclear palsy among others, grouped as tauopathies  $^{74}$ . Tau is found in the amyloid state and can form fibers *in vitro*, but the detailed structural models for the core of Tau fibers are not as well-established as reviewed for A $\beta$ : the main difficulty is sample heterogeneity, because a given fragment of Tau forms polymorphic fibers in a single preparation, which gives poor spectroscopic data  $^{75}$ . Nonetheless, structural considerations for the complex interfaces generated by Tau in the amyloid state are shown in Figure 1.14.

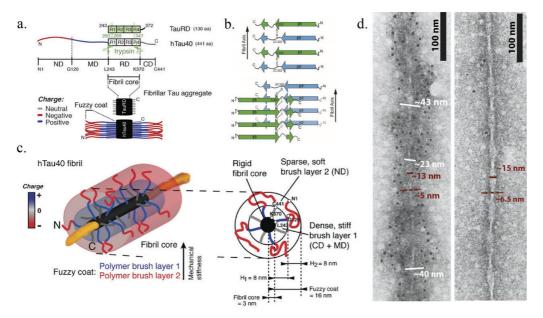


Figure 1.14 Considerations on Tau protein fiber structure. (a) Schematic depiction of the primary structure of Tau-441 and a truncated version, TauRD that lacks the disordered segments. It highlights the polyelectrolyte nature of the disordered tails that form the fuzzy coat. (b) A ssNMR model of a 99-residue core-forming fragment of Tau (K19), that includes R1, R3 and R4 from the scheme shown of the primary structure. It reveals an in register parallel beta sheet formed by the R3 segment: V306-S324. Two types of cysteine disulfide bridges are proposed: one that joins beta strands along the axis of the protofibrils, and another that unites two different layers. Reproduced from reference (75) Copyright © 2012, American Chemical Society (c) A schematic depiction of how the fuzzy coat surrounds Tau fibers, similar to a polyelectrolyte brush (d) Anti-Tau labeled nanoparticles (Immunogold) show a diffuse distribution surrounding the fibril core, consistent with binding to the disordered segments that constitute the fuzzy coat. On the right, the fibers were digested with Pronase, which the authors claim removed the disordered segments, thus eliminating immunogold labeling. Measurements in white show the distances between nanoparticles that associate to the fuzzy coat, and in red, the core of the fiber. Reproduced from reference (76). (a) and (c) are reproduced with permission from reference (77).

Similar to A $\beta$  and  $\alpha$ -synuclein, Tau can form an amyloid fiber with a twisted ribbon morphology. Because of its long disordered protruding segments, the surface of the amyloid fold is buried within a polyelectrolyte brush formed by the N-terminal domain that can be subdivided in two segments: (i) the negatively charged ND segment from residues 1 to 120, and (ii) the positively charged MD portion from 121 to 243. Figures 1.14(a) and (c) show how the N-terminal forms radially protruding disordered segments that can be approximated to a polyelectrolyte brush<sup>77</sup>. Figure 1.14(d) shows immunogold labeling that targeted regions of the disordered segments: when the fiber is treated with Pronase, the immunogold labeling no longer forms a cloud of particles around the fiber core<sup>76</sup>. The center-to-center interparticle distances in these images range from ~20 nm to ~50 nm, whereas the widest portion of the twisted ribbon measures ~15 nm, and the width at the knot is ~6.5 nm. The fuzzy coat may likely mediate how Tau fibers interact with other objects such as cell membranes<sup>77</sup> but it also provides an 'extreme' type of amyloid fiber that displays long disordered domains, to test whether our nanoparticles interact with the core of the amyloid fibers or if they scatter around

the disordered tails, as seen in Figure 1.14(d). The other two amyloid precursors reviewed so far (A $\beta$  and  $\alpha$ -synuclein) also have disordered protrusions, albeit much shorter.

#### 1.5 Structural considerations on the twisted ribbon morphology

The proposed detailed structural models discussed in the previous sections reveal that a single building block can adopt different morphologies in the amyloid state<sup>23,24,27</sup>. How these morphologies associate in 3D to form the mature amyloid fiber is not trivial to establish. In this thesis, we rely on several experiments, including cryo-EM images, to determine how the size and ligand shell of gold nanoparticles dictate their interaction with amyloid fibers. If an EM image is analyzed and compared to a model from the previous sections, one can arrive at somewhat straightforward conclusions. For example, when three strings of nanoparticles intertwine in space around an Aβ<sub>1-40</sub> fiber, the phenomenon is likely an adsorption onto an object that follows the 3-fold symmetric model, illustrated in Figures 1.6, 1.7 and 1.8<sup>28,78</sup>. On the other hand, we commonly observed two-fold symmetric fibers with a twisted ribbon morphology. Different groups have ascribed to these surfaces distinct components of the monomeric building blocks<sup>32,79,80</sup>. For example, the  $A\beta_{1-42}$  and  $\alpha$ -synuclein models, shown respectively in Figures 1.11(b) and 1.13, predict a twisted ribbon morphology, in which the edges (that we define as the smallest cross-sectional length), are made of extended solventexposed beta sheets. Other groups that used cryo-EM images to propose structural models for  $A\beta_{1-40}$  and  $A\beta_{1-42}$ , have indicated that the edges are made of amorphous N-terminal segments<sup>79</sup> 83. If all models are taken into account, three types of structure can sit at edges: solvent exposed beta sheets, loops and transitions between beta sheet segments and disordered tails and the partially disordered N-terminals proposed by cryo-EM. The latter were prepared in considerably different ways, for example, using 50 mM sodium borate at 4°C and pH 7.8<sup>39</sup>. The dry TEM images reported by these papers differ from the morphologies observed in the fibers used for ssNMR experiments, which means different objects were studied and reported. Figure 1.15(a) and (b) show the findings from cryo-EM reconstruction studies and the proposed structural models for  $A\beta_{1-40}$  and  $A\beta_{1-42}$ .

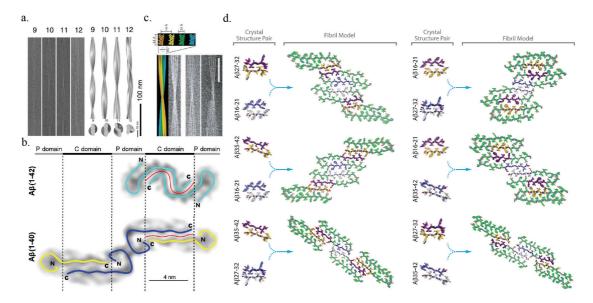


Figure 1.15 (a) Cryo-EM and reconstructed fibers for 4 or the 12 polymorphs observed in the same sample. Reproduced with permission from reference (79) Copyright © 2008 Elsevier Ltd. All rights reserved. (b) The proposed arrangement of the monomers in the twisted ribbon structures: on the top, a recent proposal for  $Aβ_{1-42}$  obtained from mass density analysis of cryo-EM images. On the bottom, the comparison to structures obtained by the same group for  $Aβ_{1-40}$  fibers. Adapted from reference (80) (c) Same image as in Figure 1.10(b) to compare the proposed arrangement of protofilaments in a twisted ribbon morphology under cryo-EM. While the models in (b) propose partially disordered N-terminals on the edges, the model in this image attributes solvent exposed beta sheets to these sites. These are dramatically different structures for the same peptide. (d) Stable zippers that can hold the Aβ monomers together: six combinations of four protofibrils are shown, four of which culminate in twisted ribbon morphologies that have solvent exposed beta sheets on the edges. The bottom two predict a combination of loops (or kinks) and 'open ends' on the edges. Reproduced from reference (26).

Figure 1.15 summarizes the different ways in which Aβ protofibrils can assemble to form a mature amyloid fiber. The protofilament is defined here as the sequence of folded monomers that form a single layer (a lamina), of the amyloid fiber: it is the unit with a ~4.7 Å meridional X-ray signal. In the protofilament, the beta sheet segments of the monomers are stacked in register and parallel to one another. The exception to this rule was shown in the Iowa mutant model (Figure 1.10), that showed an antiparallel inter-monomer arrangement in the mature fiber<sup>54</sup>. The way different protofilaments associate with one another in 3D establishes the mature amyloid fiber (a single protofilament can be the amyloid fiber itself). Figures 1.15(a)-(c) and (d) show different interpretations to the molecular nature of the surface on the edges of the twisted ribbon fibers. They are not mutually exclusive, and are probably accurate interpretations of the data acquired for their experiments. However, each experiment was done in different conditions: notably, the cryo-EM images in Figure 1.15(a)-(c) were acquired from samples prepared at lower pHs and high monomer concentration compared to all the ssNMR reviewed here, which can affect the structure of the fibers and cause the reported differences.

The A $\beta$  sequence establishes several types of steric zippers that can reconcile these different observations. The group of Prof. Eisenberg determined the structure of microcrystals made of different sequences from the A $\beta$  peptide, with the same approach described in section 1.3<sup>26</sup>. Figure 1.15(e) shows the repertoire of accessible morphologies when the steric zippers are used to tie together the detailed structural models for A $\beta$ <sub>1-40</sub> and A $\beta$ <sub>1-42</sub><sup>32,78</sup>. Four protofibrils are united via the favorable steric zippers in the A $\beta$  sequence, showing that both interpretations for the cryo-EM images in Figure 1.15(a)-(c) are possible. Most commonly, the smallest cross-sectional dimension, *i.e.* the edge of the ribbon, is a solvent-exposed beta sheet, as in the case proposed for  $\alpha$ -synuclein in Figure 1.13.

Although this reductionist approach can reconcile and provide a mechanism for polymorphisms, it does not 'predict' the 3-fold symmetric fibers shown in Figure 1.6. The landscape for amyloid polymorphisms remains vast, and no single mechanism seems capable of explaining all possible variations. The only complete amyloid fiber that has a high-resolution structural model is the prion-forming domain of HET-s(218-289)<sup>58</sup>, precisely because it shows little polymorphism, which enabled the determination of a high-quality structural model. Most disease-related amyloids come from proteins meant to adopt a native conformation that differs significantly from the amyloid fold, whereas the HET-s(218-289) protein belongs to a functional amyloid, that has been selected by evolution to adopt a particular amyloid conformation: this likely homogenizes samples of these fibers to a dominant morphology. Therefore, it is not surprising that in the amyloid state, several energetically equivalent morphologies are observed for disease-associated amyloids, which in turn causes different structures to exist<sup>47</sup>.

#### 1.6 Summary of proposed amyloid structures

This thesis shows how different types of water soluble gold nanoparticles interact with amyloid fibers, with an emphasis on the role of the nanoparticle ligand-shell. Several chemical functionalities that make the nanoparticles soluble in buffered conditions are tested: the surface chemistry of gold nanoparticles is the main determiner of this bio-nano interface. The size of the nanoparticle also affects their interaction with this class of biomolecules. The review offered thus far allows for the interpretation of the images presented in the remainder of the thesis.

The remainder of this chapter introduces the field of monolayer-protected metal nanoparticles, and shows how we have been using experiments and simulations to develop nanomaterials capable fusing with lipid bilayers. It combines the current state of the literature with my recent contributions to the field, both on the understanding of ligand phase-separation, and in the development of amphiphilic nanoparticles for the development of cell-penetrating nanoparticles.

#### 1.7 Introduction to metal nanoparticles

Gold nanoparticles have been intensively investigated for past two decades as one of the cornerstones of current-day nanoscience. Some of the fascinating properties of these materials have intrigued glass blowers of the past, as exemplified by the Lycurgus cup<sup>81</sup>, a 4<sup>th</sup> century AD dichroic glass cup. The unusual optical properties of this artefact rely on the presence of gold and silver particles that produce red color in transmission and green in reflection. Other glasses that incorporated metallic salts in their preparation, that form colloidal metal, display peculiar optical properties and have been used to manufacture ruby glasses<sup>82</sup>. The first account of "minuscule metallic particles" was given by Faraday in his Bakerian lecture in 1857, when he described unusual optical properties of suspended metallic species, especially when made of gold<sup>83</sup>. Evidence that these species were indeed minuscule metallic particles, denominated colloids, was given in 1861<sup>84</sup>, and consolidated by Turkevich in 1951<sup>85</sup>.

Colloidal science and interfacial phenomena have become a large field of study that spanned different areas of chemistry, physics, materials science and biology. It took the development of nanoscience to elucidate several recalcitrant questions in these fields. The transition in nomenclature to include the prefix "nano", meaning a  $10^{-9}$  scaling factor in the metric system, can be traced back to several origins<sup>86</sup>. The term "nanno" (with two n's) was first used in the scientific literature to describe findings in fossilized plankton<sup>87</sup>. The seed of nanoscience, however, is commonly attributed to Richard Feynman's talk in December of 1959, at Caltech, entitled "There's Plenty of Room at the Bottom", when he entertained the idea of manipulating matter atom by atom. This was achieved in 1989 by Eigler and Schweizer using a scanning tunneling microscope (STM) to spell "IBM" using xenon atoms on a nickel surface<sup>88</sup>.

There are varying degrees of stringency applied to the denomination of a material, device or structure as nano: some authors require the satisfaction of the atomic manipulation criterion<sup>86</sup>, while others accept the terminology on the basis of relevant size scales<sup>89</sup>. Whatever the criteria,

this nomenclature has burgeoned since the accomplishments obtained with the STM and has shaped research in the past 20 years with new techniques to manipulate and study matter at the nano scale. This impact includes a change in the traditional nomenclature of colloidal science that culminates in current-day nanoparticle research. Owing to this shift in approach, scope and techniques, recent works on nanoparticles differ substantially from the days of colloidal science: for example, only recently the importance of nanoscale structure to interfacial energy has been elucidated<sup>90</sup>.

#### 1.8 Overview of self-assembled monolayers and nanoparticles

Despite the interest in directly manipulating matter at the atomic scale<sup>88</sup>, the study of how molecules spontaneously self-organize is a cornerstone of nanoscience<sup>89</sup>. Thiolate molecules form self-assembled monolayers (SAM) on flat gold (Au) surfaces, because of an interplay between the robust S-Au bonds<sup>91</sup> and van der Waals interactions established between the molecules<sup>92,93</sup>. A rigid interpretation of the S-Au bond is unlikely to capture the dynamic coexistence of different bonding motifs that establish the gold-thiolate inteface<sup>92-94</sup>. Different sulfur containing species can form SAMs on gold: thiols (RSH), disulfides (RSSR) and even thioethers (RSR), where R stands for an alkyl or aryl group. In fact, the first reported sulfurbased SAM on gold was obtained using disulfides<sup>95</sup>, which then led to several studies on a variety of SAMs on gold. Figure 1.16(a) shows schematically the basic features that underlie a SAM on gold and Figure 1.16(b) depicts recent experimental and theoretical developments on the dynamic nature of the Au-S bonding motif on a SAM.

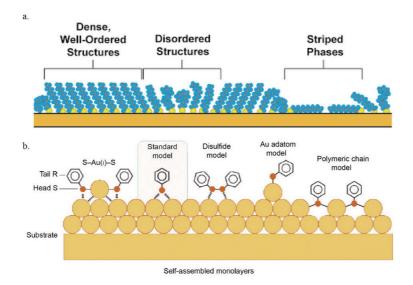


**Figure 1.16 (a)** Schematic view of a thiolate self-assembled monolayer on flat gold. On the right, at a low density, the lying down or striped phase, when the alkanethiols establishes a Au-S bond but adopt a configuration parallel to the surface. As the density of thiols increases, they adopt the standing up phase which can be ordered or slightly disordered. **(b)** Recently proposed bonding motifs between Au and S atoms. The standard model assumes a single sulfur on top of a hollow site on an unreconstructed gold surface. This conventional bonding has been questioned by several calculations and experiments that show: possible disulfide bonding; a sulfur on top of a Au adatom; or a sulfur-gold polymeric chain. On the very left, a motif backed by recent experimental data in which a RS-Au<sup>1+</sup>-SR staple is formed. Adapted with permission from references (a) (89) Copyright © 2005, American Chemical Society and (b) (91) Copyright © 2007, The American Association for the Advancement of Science

The interfacial properties of a SAM, for example wetting, are dictated by the molecular end groups of the constituent thiol. The behavior of SAMs made of different thiols in binary (or ternary and greater) mixtures on the surface posed a research challenge in the 1990s<sup>96,97</sup>. Stranick et al. showed that binary SAMs, depending on the sample preparation conditions, tend to phase-separate into nano-sized domains<sup>98</sup>. The Gibbs free energy of the system reaches a minimum through a trade-off between entropy maximization that drives random mixing, and minimization of enthalpy that is satisfied via favorable intermolecular contacts, that drives phase separation. The competing driving forces for separation and mixing result in nano-sized islands<sup>98</sup>. This thermodynamic trade-off is common in materials science and its 3D soft material archetype rests on the phase-separating mechanisms behind the intricate nanostructures adopted by block copolymers<sup>99</sup>.

When a binary self-assembled monolayer is confined to a small, highly curved 3D object such as a nanoparticle, geometric constraints affect how the molecules phase separate. When alkanethiols have a size-mismatch, there is an entropic gain for the taller ligands to access conformations otherwise unavailable in a side-by-side packing with homologous molecules <sup>100</sup>. This favors tall/short interfaces that, at suitable stoichiometries, manifest as linear alternating

domains of each molecule 100,101. Figure 1.17 summarizes schematically the driving forces behind phase separation in flat and curved binary SAMs, the predicted morphologies and STM images for each instance. Figure 1.17(a) shows a cross-sectional schematic representation of nanophase separation on a flat surface, followed by the predicted computational model of the morphology and the strikingly similar STM image of a surface covered by a mixture of 1butanethiol and 1-hexanethiol. The phase separation is evident, however, the domains are disordered. Figure 1.17(b) illustrates that when the two ligands are confined to a curved surface, the gain in free-volume, in other words, the increase in head-group conformational entropy drives ordered phase separation. This driving force favors tall/short molecular interfaces, which correspond to the formation of stripe-like domains. The two STM images correspond to 4 nm particles protected by 3-mercaptopropionic acid and 1-octanethiol. The lines of the taller molecule give the particle its striped morphology, despite some defects in the monolayer. Finally, when the particles are below a size threshold, enthalpy becomes the dominant parameter and calculations predict complete phase separation<sup>100</sup>. This Janus morphology was identified under STM imaging of a particle protected by 11-mercapto-1undecanol and 4-mercapto-1-butanol, seen in Figure 1.17(c)<sup>101</sup>. The data shown in Figures 1.17(b) and (c) result from our recent work in the investigation of ligand phase separation on gold nanoparticles using STM.

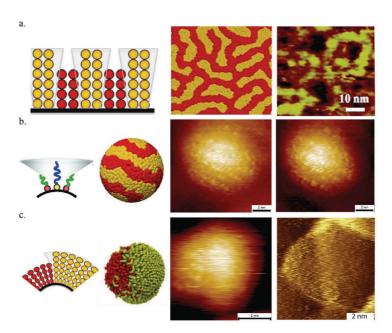


**Figure 1.17 (a)** Overview of binary SAMs on flat surfaces showing the phase-separation pattern predicted by theory and the STM image that matches the calculated morphology. **(b)** Schematic view of the free-volume gain that correlated to a conformational entropic gain, leading to the formation of stripe-like domains on a simulated nanoparticle. On the right, two images we have recently obtained at high resolution STM (trace and retrace) for 1-octanethiol and 3-mercaptopropionic acid

protected particles: the spacing between molecular end-groups across two lines is 1 nm, and within a line 0.5 nm. (c) Schematic representation for a monolayer on a particle in which the enthalpic component predominates, and total phase separation is both predicted by theory, and observed with STM. Reprinted and adapted from references (100) Copyright © 2007, American Physical Society and (101) Copyright © 2013, American Chemical Society.

It is possible that, similar to the amyloid fibers, different morphologies are available to monolayer protected gold nanoparticles (AuNPs), and perhaps, careful annealing can favor certain monolayer structures. Like in the amyloid case, the issue of property-structure relationship can be difficult to verify, but our group has successfully demonstrated the role of ligand morphology in several systems 90,102,103. A good example that summarizes this section and demonstrates a property dictated by nanoscale phase separation is shown in Figure 1.18. In this experiment the contact angle and the work of adhesion to displace water molecules from the vicinity of the surface are measured by amplitude modulated atomic force microscopy (AM-AFM) for mixed-ligand SAMs on flat gold and for films made of binary monolayerprotected gold nanoparticles. The molecules used are the hydrophobic 1-octanethiol (OT) and the hydrophilic 6-mercapto-1-hexanol (MHol). As the amount of MHol on the flat surface increases, the work of adhesion increases monotonically with composition (Figure 1.18(a) and (d)). When surfaces are made of the same molecules but on nanoparticles, the work of adhesion does not scale monotonically with the MHol content. This highlights the importance of nanostructure on a fundamental interfacial property. When nano-domains commensurate with the solvent correlation length form, the surface structure changes the work of adhesion at the molecular scale. Small hydrophobic regions intercalated with hydrophilic ones create pockets of solvent cavitation and confinement that increase the work of adhesion at intermediate compositions, followed by a collapse of the semi-classical behavior described by the Dupré equation: this observation was confirmed by molecular dynamics simulations. Naturally occurring complex amphiphilic surfaces such as proteins likely follow this type of wetting behavior, rather than a purely composition-dependent approach to interfacial energy<sup>90</sup>.

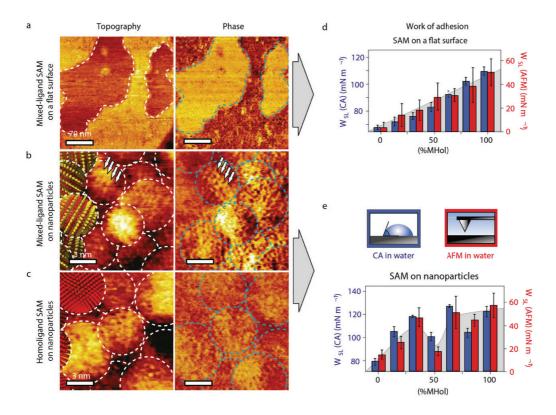


Figure 1.18 Experimental results for non-classical work of adhesion and contact angle (images obtained using atomic force microscopy, AFM). (a) Flat SAM of MHol and OT forms islands and domains larger than 5 nm, and the resulting work of adhesion of water is adequately predicted by the classical compositional approach. (b) When the nanodomains become commensurate with the water molecules themselves, a structural deviation from the classical approach to the work of adhesion if observed, and the results deviate by about 20% due to the nanostructure of the surface (c) Images of nanoparticles covered with only one ligand. (d) and (e) experimental results showing the deviation of property from a purely compositional approach. Reprinted with permission from reference (90) Copyright © 2009, Rights Managed by Nature Publishing Group.

#### 1.9 Amphiphilic gold nanoparticles: synthesis and characterization

The potential biomedical applications for this class of materials is enormous, because nanoparticle structural features can be tuned at the length scale of the building blocks of living organisms<sup>104</sup>. These applications span from drug delivery<sup>105</sup>, biosensing<sup>106</sup>, bio-imaging<sup>107</sup> all the way to direct uses as nanotherapeutics and antiviral agents<sup>108</sup>. In order to achieve the same breadth and utility that conventional molecular biomedical strategies enjoy, the unanticipated properties brought by nanomaterials need to be addressed. Furthermore, only by researching fundamental aspects of the *bionano interface*<sup>109</sup> can novel solutions be found to address old problems. One of the main challenges in working with nanoparticles is the production of species that are stable or soluble in physiological buffers and *in vivo*. Most of the synthetic approaches available for gold nanoparticles take place in hydrophobic conditions, and produce monolayer-protected AuNPs suitable for non-polar organic solvents<sup>110</sup>. Although many

synthetic routes exist, the standard approach depicted in Figure 1.19 consists of the dissolution of a gold salt in water, followed by phase transfer, addition of capping ligands and reduction.

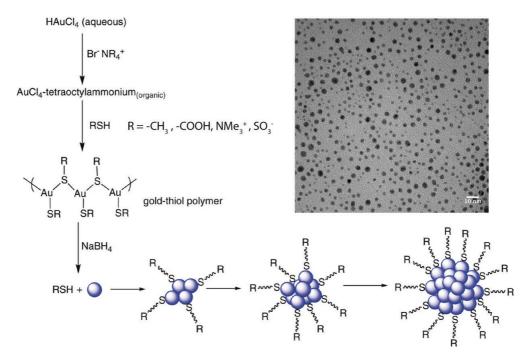
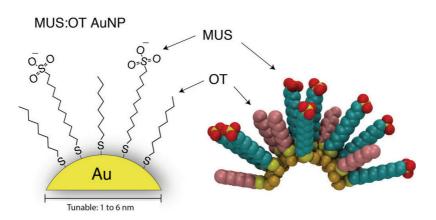


Figure 1.19 Simplified synthetic scheme of conventional gold nanoparticles. This synthesis relies on the dissolution of tetrachloroaurate ( $Au^{3+}$ ) in an organic solvent: typically, the gold salt is dissolved in water, and phase-transferred to an organic solvent using a surfactant. In this work,  $HAuCl_4\cdot 3H_2O$  is dissolved directly in ethanol, to which the thiol compounds are added. In the presence of thiols, the  $Au^{3+}$  undergoes a first reduction to form a gold-thiol polymer complex. The addition of a reducing agent, typically sodium borohydride ( $NaBH_4$ ) causes the nucleation of the nanoparticles, which then grow to their final sizes. A TEM of a typical synthesis performed for this thesis, using a sulfonated thiol is shown to illustrate the size distribution of the particles. Adapted with permission from reference (111) Copyright © 2009, American Chemical Society

Polar nanoparticles can be produced using the standard synthetic pathways<sup>110</sup>, which have typically been done with carboxylate and ethylene glycol terminated thiols. Our group has discovered that sulfonate terminated thiolates grant the particles remarkable buffer and *in vivo* solubility<sup>112</sup>. The ligand used to this end was 11-mercapto-1-undecanesulfonate (MUS), which when mixed with 1-octanethiol (OT) forms amphiphilic water-soluble nanoparticles, capable of diffusing through the lipid membranes of cells *in vitro*<sup>103</sup>. The TEM image in Figure 1.19 shows a typical nanoparticle batch made of particles covered exclusively by MUS, named here homo-ligand allMUS nanoparticles (allMUS NPs). Figure 1.20 illustrates the surface composition of hetero-ligand MUS:OT particles (MUS:OT NPs), and shows a molecular model of the same nanoparticle. Other groups have found different alternatives for buffer-stable nanoparticles, mainly using zwitterionic terminated thiols or cationic groups<sup>113,114</sup>. Previous work on SAMs had shown that zwitterionic head-groups reduce non-specific protein

adsorption<sup>115</sup>, which has been harnessed to produce *in vivo* stable nanoparticles, and is used in this thesis as a control particle in Chapter 3.



**Figure 1.20** Schematic view of the surface of a gold nanoparticle with a mixed SAM of MUS and OT. On the right, a simulation snapshot of the mixed SAM. The diameter of the gold core can be tuned both through synthesis and fractionation techniques. Image created by Dr. Reid Van Lehn for reference (116).

The synthetic scheme in Figure 1.19 is often referred to as the two phase synthesis. The phase transfer step can be skipped, and the gold salt (HAuCl<sub>4</sub>·3H<sub>2</sub>O) can be directly dissolved in ethanol followed by addition of the thiol mixture. After a short interval, typically 5 to 20 minutes, depending on the protocol, a saturated, filtered, ethanolic solution of sodium borohydride (NaBH<sub>4</sub>) is added drop-wise, which causes the thiol-gold complex to nucleate and grow into nanoparticles. We call this protocol the one-phase synthesis that can be used to produce a wide variety of monolayer-protected nanoparticles <sup>102,117</sup>. For particles covered with MUS and OT (the MUS:OT system), this synthesis typically yields a size distribution centered around 3 nm but with a high, condition-sensitive polydispersity index. To address this, when necessary, size-fractionations are performed using centrifugation in a sucrose gradient.

Furthermore, this synthetic approach can produce populations of ultra-small particles that are under-represented in conventional size-distribution analyses. For example, a TEM image of a sample is usually analyzed using an image processing software to automatically estimate all the sizes and report a size distribution histogram. Any nanoparticle characterization technique must be approached with care: small enough particles imaged on a conventional carbon film may not be sufficiently electron-dense to produce a contrast that the image processing software can detect. To circumvent this problem, other techniques can be used, for example analytical ultracentrifugation (AUC)<sup>118</sup> can capture detailed information on nanoparticle size distribution, but requires laborious data treatment. A simple alternative is the use of Scanning Transmission

Electron Microscopy (STEM) that is sensitive to the height of the particles, providing excellent contrast for these types of samples (Figure 1.21).

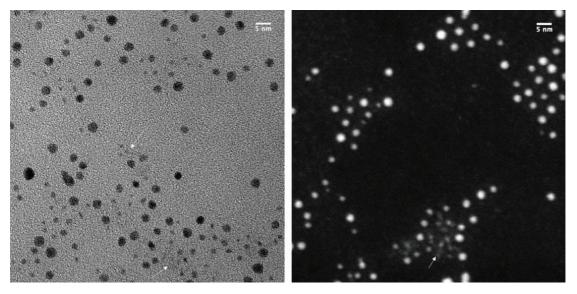


**Figure 1.21** Comparison between (left) a standard TEM image of a one-phase batch of allMUS nanoparticles, and (right) a STEM image of the same sample on the right. If acquired carefully, the standard bright-field TEM image can capture all particle sizes. Extremely small particles may appear as densities in a standard carbon grid. This can be addressed by using a thinner carbon grid, however, by switching the imaging mode to STEM, when possible, ultra-small particles become evident and sample characterization can reflect the presence of these objects that may respond for experimental findings. White arrows point to particularly small sub-nanometer particles, that are more evident under STEM mode. Images obtained in an FEI TALOS<sup>TM</sup> Electron Microscope.

Other groups usually synthesize analogous particles using a place exchange approach<sup>113</sup>. Typically, particles are prepared using the traditional two-phase method illustrated in Figure 1.19 and the desired ligand is place-exchanged onto their surfaces. Ideally, a nanoparticle protected by short alkanethiols is prepared (usually 1-pentanethiol), suspended in an appropriate solvent, for example, dichloromethane, and placed in contact with an aqueous solution of the target thiol under agitation. Longer thiolate molecules readily displace shorter ones, cover the particle, which makes this approach successful and creates homogeneous samples for a library of ligands<sup>114</sup>. Given our interest in mixed-ligand nanoparticles to study how surface nano-structure affects properties, it is difficult to control and reconcile the solubility of two disparate molecules in this kind of preparation, hence the preference for a direct synthetic approach that gives an exact ligand stoichiometry and allows us to reproducibly study mixed-ligand nanoparticles.

To synthesize larger (4-7 nm) less polydisperse nanoparticles, several conditions using a synthetic pathway designed for non-polar ligands were tested 119. The synthesis of nanoparticles

can be sensitive to several factors: ultimately, an interplay between the chemical potential of the different species in the flask and kinetic barriers determine the outcome. When all species are soluble during the synthesis, molecules and thiol-gold complexes can exchange across the different species to approach thermodynamic equilibrium. Nevertheless, when using two ligands with different solubility, exchange of material can be hampered by the high free energy cost for an insoluble species to transfer from one assembly to another: in others words, the ligand exchange in a bad solvent is not favorable. The particles are, to a first approximation, kinetically trapped. We have adapted the method by Zheng et al. that relies on the reduction of a gold phosphine precursor (Au<sup>1+</sup>), to produce MUS-based nanoparticles. Briefly, AuPPh<sub>3</sub>Cl was dissolved in a solvent mixture of 10% water in dimethylformamide (DMF) along with MUS and/or OT, and brought to 125°C. The mixture was allowed to equilibrate for 10 to 20 minutes, followed by the addition of a borane reducing agent (tert-butylammonium bromide, etc), in the same solvent mixture. The solution was allowed to stir for one hour, then cooled to room temperature and held at 4°C overnight. The nanoparticles precipitated as a black powder that was then washed via centrifugation-assisted decantation, followed either by dialysis or membrane centrifuge filtration. In this thesis, this method is referred to as the modified Stucky synthesis.

The combination of these two synthetic protocols, one-phase and modified Stucky, in addition to the sucrose-gradient fractionation<sup>120</sup> gave us reasonable control over the particle size distribution. Some nanoparticle parameters vary across separate syntheses, for example, the ratio between the two different ligands. This issue was addressed by fine-tuning the sample preparation for nuclear magnetic resonance (<sup>1</sup>H-NMR) ligand-ratio determination (Figure M.12 in methods). Similar to early works on SAMs<sup>97</sup>, the ratio of thiols added to the reaction does not necessarily correspond to that found on the monolayer. Longer alkanethiols form more stable SAMs because their chemical potential in the monolayer phase is lower than that of a shorter molecule. This can be explained by the satisfaction of intermolecular van der Waals interactions that scale with the length of the molecule, hence, the chemical equilibrium of longer alkanethiols favors the monolayer phase compared to its shorter counterparts. From our analysis of different syntheses, this rule seems to apply for MUS:OT particles made via the one-phase method, in which MUS was over-represented in the final particle ligand ratio. However, particles synthesized following the modified Stucky approach had usually a lower MUS to OT ratio than that used during the reaction. This indicates that a purely thermodynamic

explanation is unlikely to capture all relevant parameters determining this ratio. Figure 2.7 shows the results of the feed ratio versus calculated post-synthesis stoichiometry for several batches synthesized using the two different methods. The approach used to obtain these ratios is shown in the methods chapter. This chart is only representative of the nanoparticles we prepared in the past few years with these protocols; the system is sensitive to small variations, and numbers that do not follow this trend are not necessarily inaccurate.

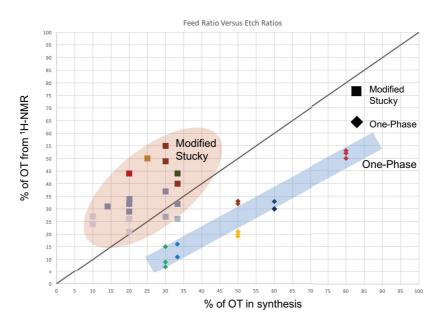
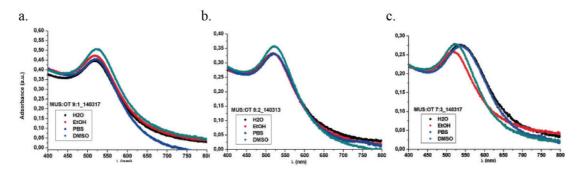


Figure 1.22 The horizontal axis shows the percentage of OT added to the reaction mixture, while the vertical gives the calculated ratio on the particles from the etched sample, measured by  $^{1}$ H-NMR (details in Methods chapter). Squares denote individual batches of modified Stucky syntheses and diamonds one-phase. Each point is the final ratio, and the instrumental error bar can be estimated between 2 to 5% depending on the quality of the NMR spectrum and how it was treated. The black line shows a f(x) = x function to help understand where the ratios fall respective to a faithful correlation between feed and calculated ratios. There seems to be a trend for one-phase, that lies below the expected ratio: however, more experiments are needed to determine how these compositions converge to the central line. The modified Stucky protocol is still under development, and recently we've succeeded in getting feed and calculated ratios to match. It must be highlighted that different people in different times may have obtained results outside the trends above: these reflect observations from syntheses conducted exclusively in the past 4 years.

These particles are amphiphilic, and their water solubility decreases as the amount of OT increases. For Stucky particles, the water-solubility threshold seems to be around 30-34% OT, but this value is slightly higher for one-phase batches. The mechanism behind this difference in solubility is still unclear, but can be due to a size-effect: given the same hydrophobic content, 1 nm NPs may be more soluble than a 5 nm one because of greater ligand end group mobility in small particles. These assessments are still qualitative, but carry an important message: particles with a high OT content can be solubilized by adding small amounts of an organic cosolvent (5% ethanol or DMSO) to the water or buffer. This means that biological experiments with hydrophobic nanoparticles, possibly carrying unusual nanostructures, are feasible. Figure

1.23 shows three different UV-vis spectra for particles synthesized via the modified Stucky method with feed ratios of 9:1, 8:2 and 7:3 that by <sup>1</sup>H-NMR were determined to be 8:2, 66:33 and 6:4. The first two batches are soluble in water, buffer and with added organic solvents, whereas the third only shows a narrow 520 nm plasmon resonance peak in the presence of added ethanol or DMSO. In water or buffer, the UV-vis signal is broad, which indicates aggregation and poor solubility.



**Figure 1.23** UV-vis spectrum of a nanoparticle batch in different solvent conditions (a) 20% OT (b) 30% OT and (c) 40% OT. (c) displays a broad peak in water and PBS buffer indicative of poor solubility, which is restored by the addition of ethanol or DMSO. In collaboration with Dr. Patrizia Andreozzi.

Finally, the nanoparticles can be fractionated by centrifugation using a sucrose gradient. For biological experiments, there is an advantage to initially work with polydisperse samples: if EM is involved, it is possible to identify size selectivity and subsequently engineer nanoparticles to address specific size-dependent questions. In other words, when the experiment is done with similar particles of different sizes, in case smaller or larger particles interact preferentially with a given structure, the use of a polydisperse sample can reveal in a single experiment size-dependent behaviors. On the contrary, if an experiment is designed to use monodisperse 5 nm NPs in a system that would preferentially interact with 2 nm NPs, the interactions would not be captured. Given that the two different synthetic methods (modified Stucky and one-phase) produce particles with distinct size distributions, the added benefit of fractionation provides a level of sample homogeneity otherwise impossible for these polar nanoparticles. Figure 1.24 shows TEM images of fractionated one-phase and modified Stucky allMUS and MUS:OT syntheses: the sample homogeneity is greater than in the images presented in Figures 1.19 and 1.21. The post-fractionation sample homogeneity may be important for future spectroscopic experiments involving nanoparticle-protein interactions, namely, using multi-dimensional NMR to pinpoint nanoparticle-protein interactions.

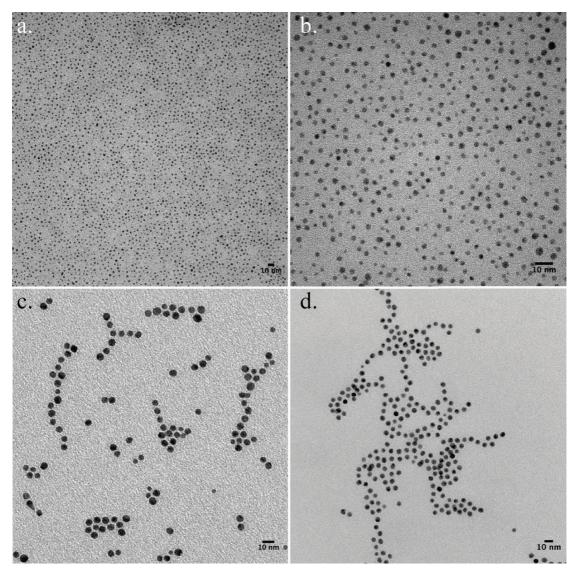


**Figure 1.24** Bright field transmission electron micrographs (TEMs) of **(a)** One phase fractionated allMUS NPs **(b)** One phase fractionated MUS:OT (30% OT by <sup>1</sup>H-NMR) **(c)** Modified Stucky MUS:OT (30% OT by <sup>1</sup>H-NMR) **(d)** Modified Stucky fractionated allMUS NPs. **(c)** was obtained using a Philips CM12 TEM, and the others using an FEI TALOS<sup>TM</sup> Electron Microscope.

#### 1.10 Amphiphilic gold nanoparticles: interaction with lipid bilayers

Evolution has selected lipids bilayers as the material to encapsulate and delimit the compartments of cell-based organisms. Briefly, lipid bilayers are made primarily of phospholipids and are permeable to small hydrophobic molecules such as CO<sub>2</sub> and O<sub>2</sub>, semi-permeable to water and impermeable to most charged species and large molecules<sup>121</sup>. Lipid membranes are controlled by meticulous cellular mechanisms, that inevitably include membrane-bound proteins<sup>122</sup>. The cell membrane, made of a lipid bilayer, topologically delimits the inside and outside of a cell. Most small foreign substances never enter the cell, but

are rather encapsulated by the membrane inside endosomes, thus remaining, technically, extracellular. The cell might then incorporate and process the foreign body, or eliminate it via exocytosis depending on the situation. Therefore, traversing the cell membrane is an enormous challenge: for example, even sugar molecules depend on specific channels to enter the cell and supply it with the energy needed for survival<sup>123</sup>. There are substances capable of disrupting cellular membranes, such as surfactants, viral related cell-penetrating peptides<sup>124-126</sup> and small oligomers of amyloid precursors<sup>127</sup>. Mature amyloid fibers are also membrane fusogenic, and prostate protein derived amyloid fibers have been reported to interact with cellular membranes and enhance HIV infectivity in the process<sup>128-130</sup>.

The possibility that nanoparticles interact with lipid bilayers became an important field of study, whether to assess toxicity, or to design particles that facilitate the delivery of therapeutic agents that are otherwise excluded from the intracellular space<sup>104</sup>. Initial studies showed that nanoparticles could not evade endosomal entrapment simply by virtue of size<sup>131</sup>, and most particles designed to improve drug delivery end trapped inside endosomes. In 2008 our group reported amphiphilic monolayer-protected nanoparticles capable of passively diffusing through cellular lipid membranes without disrupting them<sup>103</sup>. Nanoparticles covered by mixtures of MUS and OT readily entered cells when compared to homo-ligand allMUS nanoparticles or hetero-ligand analogues bearing a branched, stiffer alkanethiol (branched OT - brOT) instead of OT. Cell-penetration was also detected in samples kept at 4°C, when cells cannot use energy to perform endocytosis, which indicates a passive entrance mechanism for MUS:OT particles.

This phenomenon has been intensively investigated both through experiments and calculations<sup>132-135</sup>. In order for amphiphilic nanoparticles to enter cells, they must interact with lipid bilayers as an obligatory step to passively diffuse through the membrane. The thermodynamic framework for a NP to fuse into the bilayer core has been delineated <sup>133,134,136-138</sup> and reveals that hydrophobicity and size determine the integration of nanoparticles in a model lipid bilayer. Figure 1.25 shows a schematic view of the process and the total free energy change for moving a nanoparticle from an initial position in the solvent into the bilayer core. Thermodynamically, the problem can be stated as the minimization of the total Gibbs free energy of the system, as shown in equation (1).

$$\Delta G_{\text{total}} = \Delta G_{\text{phobic}} + \Delta G_{\text{insert}} + \Delta E_{\text{elec}} + \Delta E_{\text{thick}} - T\Delta S_{\text{conf}}$$
 (1)

In this equation,  $\Delta G_{phobic}$  is the system-solvation free energy change, and  $\Delta G_{insert}$  the free energy cost for charged ligands to interact with the bilayer core.  $\Delta E_{elec}$  is the free energy change due to electrostatic contacts, while  $\Delta E_{thick}$  accounts for the energy cost of altering bilayer thickness. The final entropic term relates to the changes in conformational entropy of the ligands upon bilayer integration. The main driving force is the first term that stands for the hydrophobic driving force that pushes the system towards the minimization of hydrophobic solvent exposed surface area (SASA)<sup>139</sup>.

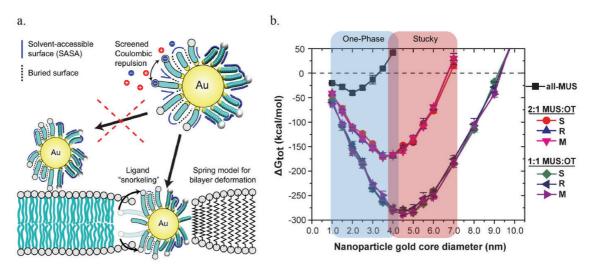
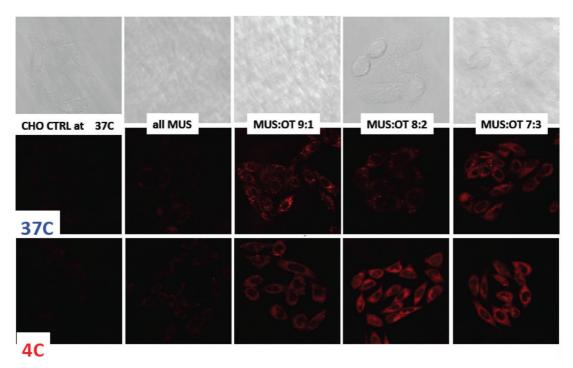


Figure 1.25 (a) Schematic representation of a typical MUS:OT gold nanoparticle and a lipid bilayer (in a spring model). The nanoparticle is shown using a standard Au-S bonding motif, the blue-green parts of the ligands and inside the lipid bilayer stand for hydrophobic groups. In blue the solvent-accessible surface area is highlighted: it constitutes hydrophobic surfaces exposed to water. Upon integration within the lipid bilayer, the ligands re-arrange in a conformation that maximizes hydrophobic contacts and exposes the charged ligands to the aqueous medium. (b) Depicts the free energy calculations for three different particle compositions (allMUS and MUS:OT 2:1 and 1:1) in addition to different morphologies that, thermodynamically do not differ in this system. Blue and red panels illustrate where the different synthetic protocols discussed fall in this formulation. Adapted with permission from reference (135) Copyright © 2013, American Chemical Society.

The thermodynamic approach in addition to careful experimentation demonstrated that amphiphilic nanoparticles can integrate into the lipid bilayer core<sup>120,135</sup>. As the nanoparticle partitions to the interior of the bilayer, the ligand shell undergoes a rearrangement that forces charged ligand head-groups to face the aqueous exterior, and favors hydrophobic contacts between SASA and the aliphatic chains in the lipid bilayer. This phenomenon resembles how some proteins integrate the bilayer through a process known as snorkeling<sup>140,141</sup> which is more accessible for flexible ligands in smaller particles. As the nanoparticle diameter increases, the surface curvature decreases and the ligands have less space to rearrange. This decreases the ability of larger particles to integrate the core of the lipid bilayer, eventually reaching a size cutoff, in which, the change in total free energy is zero (Figure 1.25(b)). These results highlight the importance of Figure 1.21, because small nanoparticles in an experiment designed to isolate

the effect of surface composition or structure can produce false positives, especially in fluorescence-based biological experiments that cannot distinguish signal from particles of different sizes.

Recently, as the synthetic protocol to produce sulfonated particles with a size distribution between 4-7 nm improved (the modified Stucky synthesis), we've observed the right part of Figure 1.25(b), highlighted by a red panel, in cell cultures. Particles synthesized using the Stucky protocol were tagged with the fluorophore BODIPY and incubated with cells at 37°C and 4°C, revealing the importance of hydrophobicity for cellular internalization, in agreement with the free energy curves. Figure 1.26 shows Chinese hamster ovary (CHO) cells incubated with progressively hydrophobic particles (4-7 nm in core diameter). At 4°C, the fluorescence scales with hydrophobic content, which agrees with the theory. These studies are still on-going, and will also include the effect of ligand-shell morphology on the cell-penetrating behavior of larger, Stucky-prepared gold nanoparticles.



**Figure 1.26** Chinese hamster ovary (CHO) cells incubated with BODIPY-modified gold nanoparticles. All particles were synthesized following the modified Stucky protocol. Clearly, nanoparticles that only contain MUS are not efficiently internalized by cells, whereas, as the amount of OT increases, the fluorescence signal increases, especially in the 4°C samples. Punctate signal correlates to endosomes, and is visible only at 37°C, when the cell can perform energy-dependent processes. This figure showed for the first time that modified Stucky-prepared particles could be effectively used for cellular internalization. The ligand ratios correspond to the feed ratio: the H-NMR ratios were approximately 20%, 30% and 40% OT. In collaboration with Dr. Patrizia Andreozzi, who performed the cell experiments.

Despite the invaluable insight offered by the free-energy approach to this problem, the mechanisms of nanoparticle-bilayer integration remained largely unknown. Free energy minimization cannot explain how the nanoparticles overcome barriers, for example, the unlikely first disruption of bilayer integrity for hydrophobic contacts to occur. The mechanism behind lipid bilayer integration has been recently elucidated using unbiased atomistic simulations and experiments on supported lipid bilayers<sup>116</sup>. allMUS and MUS:OT nanoparticles spontaneously fuse with lipid bilayers through defects and highly curved parts of the membranes. This mechanism is likely mediated by stochastic lipid tail protrusions, similar to those behind vesicle-vesicle contacts<sup>142-144</sup>. Figure 1.27 shows the free energy landscape for the fusion of nanoparticles into lipid bilayers and AFM images of suspended lipid bilayers (SLBs) before and after addition of MUS:OT 2:1 nanoparticles in buffer.

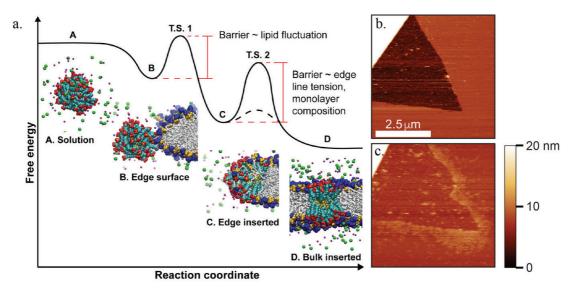


**Figure 1.27 (a)** Proposed pathway for defect-mediated bilayer integration of amphiphilic MUS:OT nanoparticles. Briefly, the nanoparticles start in a solvated state A, followed by a gain in free energy due to electrostatic attraction that drives the particle to state B. The lipid bilayer imposes an energy barrier related to the rearrangement of lipids to accommodate the incoming particle. Once fusion happens via a stochastic lipid tail protrusion, the particle reaches a metastable state C, where it finds itself "stuck" on the edge of the bilayer. Here, the transition state (TS2) is associated to the re-creation of the bilayer edge, but may also depend on nanoparticle properties. The particle then reaches state D when is can diffuse through the interior of the bilayer leaflet. **(b)** Shows a suspended lipid bilayer made of 1,2-dioleoyl-sn-glycero-3-phosphocholine (DOPC) before the addition of nanoparticles, and **(c)** shows not only that particles integrate the membrane through the edges, but are also capable of diffusing into the bilayer, corresponding to state D in the energy diagram. The ligands and nanoparticles used in this experiment come from my synthetic platform. State D was not observed in the experimental length scale, but was seen in 100s of minutes in AFM imaging. Energy diagram courtesy of Dr. Reid Van Lehn, and AFM images from Dr. Ricci, this material was published in reference (116).

AFM images of SLBs made of 1,2-dioleoyl-sn-glycero-3-phosphocholine (DOPC) showed that the nanoparticles did not interact with defect-free bilayers (data not shown). When the bilayers were prepared as islands, the edges swelled in the presence of allMUS and MUS:OT nanoparticles, which was confirmed by quartz crystal microbalance (QCD) measurements

(Figures 1.28 (c) and (d)): the amphiphilic particles inserted into the bilayer islands through the edges of the islands. These experimental findings agree with unbiased atomistic simulations that revealed the nanoparticles do not interact with the planar aspects of simulated DOPC ribbons, but rather insert through the edges. Figure 1.28(a) and (b) show the probable mechanism behind edge-on nanoparticle integration: a parameter p (the committor), correlated to the probability that a trajectory from state i to f successfully occurs is plotted with the hydration (H<sub>c-sol</sub>) of the aliphatic tails of the phospholipids. When these two parameters intersect in time, it indicates that a successful trajectory is correlated to a spike of aliphatic hydration, followed by its decay. In other words, aliphatic lipid tails stochastically protrude into the aqueous milieu, which is energetically unfavorable due to the hydrophobic effect<sup>139</sup>. These lipid tail protrusions happen continuously, and normally, the aliphatic chain resumes to its original position in the hydrophobic core of the lipid bilayer. However, if an amphiphilic nanoparticle such as MUS:OT is in the vicinity of the hydrated aliphatic chain, the unfavorable water-contacts can be mitigated by establishing a hydrophobic interaction with the aliphatic portions of the nanoparticle ligand shell. This mechanism, already proposed for vesicles 142 is the likely pathway for nanoparticle-lipid integration. In a more recent calculation, Van Lehn et al. predicted that nanoparticles can also insert into defect-free lipid bilayers if the nanoparticle brings a longer hydrophobic ligand capable of establishing a protrusion of its own 138.

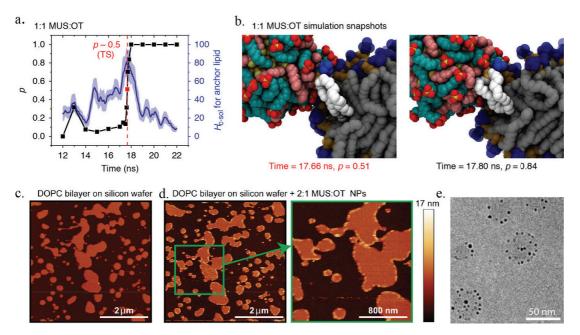


Figure 1.28 (a) Against time, both the committor p and the number of solvent-lipid anchor contacts  $H_{c-sol}$  are plotted. p correlates to the probability that a trajectory starting at an initial energy state i reaches a final state f before returning to i.  $H_{c-sol}$ 

sol quantifies the number of atoms in water molecules at a distance smaller than 0.5 nm from the aliphatic tail. The red vertical dotted line marks the transition states described in Figure 1.27, which corresponds to p values of about 0.5: the tipping point to return to the origin or to move onwards to the next state. These plots show that before reaching the interior of the lipid bilayer (p = 1), the transition state overlaps with a spike and abrupt drop in the unfavorable water-aliphatic interactions for the anchor-lipid ( $H_{c-sol}$ ). This means that the unfavorable water-aliphatic interactions are mitigated by a nanoparticle-lipid protrusion contact. This is the proposed mechanism of membrane integration for MUS and MUS:OT nanoparticles. (b) Simulation snapshots at crucial times for the integration of the nanoparticle into the lipid bilayer. (c) AFM in liquid of DOPC islands on silicon. (d) border swellings of the islands when MUS:OT 2:1 NPs are injected in the system. (e) A cryo-EM image of lipid vesicles with MUS:OT 2:1 nanoparticles integrated in (or adsorbed on) the bilayers. The ligands and nanoparticles were produced in my platform. Images (a) and (b) produced by Dr. Reid van Lehn and (c) and (d) by Dr. Ricci, published in reference (116). Image (e) obtained by Dr. Atukorale, published in reference (145), reproduced with permission from the Centre National de la Recherche Scientifique (CNRS) and The Royal Society of Chemistry.

Although these results elucidate the original finding of cell-penetrating nanoparticles, they do not address the issue of surface morphology like the experiment described in Figure 1.18 does. Neither the free-energy calculations, nor the mechanistic approach predicted differences that depended on surface structure. As in the case of proteins, subtle local structures <sup>146</sup> can manifest specific properties that in turn, dictate a structure-property relationship; determination of this, however, lies beyond the scope of these works. A detailed understanding of how surface structure affects the wetting behavior and how the nanoparticles interact with ions in solution can bring this type of research closer to the current view held for proteins.

On the other hand, these contributions help rationalize how MUS:OT nanoparticles, and perhaps, similar amphiphilic objects interact with cells. These nanoparticles attack the edges of lipid bilayers<sup>116</sup> and also insert into lipid vesicles (Figure 2.28(e))<sup>145</sup>. The latter can be attributed to the curvature of the membranes, which increases the probability of hydrophobic contacts favorable to nanoparticle-lipid fusion. Furthermore, once nanoparticles fuse with the lipid bilayers, they distort its neighboring area<sup>137</sup>, which creates a local defect that facilitates the incorporation of additional nanoparticles. This cooperative membrane fusion can explain the effective nanoparticle-vesicle fusion observed experimentally with vesicles<sup>135,145</sup>. Nonetheless, the nanoparticle-membrane fusion does not disrupt bilayer integrity, as calcein, a dye used to test membrane leakage does not enter cells or vesicles when exposed to fusogenic nanoparticles<sup>103,135</sup>.

Cells display complex lipid membranes that are, in reality, composites of lipids, proteins and sugar molecules under continuous change. Living cells offer a plethora of defects and membrane inhomogeneities through which these nanoparticles can fuse and penetrate the cell. Contrary to the initial assertion that nano-objects are incapable of traversing lipid membranes<sup>131</sup>, different works showed that carefully designed nanoparticles diffused through cell membranes<sup>103,147,148</sup>, which can be harnessed in several biomedical applications<sup>104</sup>. The

complexities of an organism need to be taken into account when translating *in silico* and *in vitro* findings to the *in vivo* environment. The basic knowledge generated by these experiments and calculations enable a rationale for applying these materials *in vivo*<sup>145,149</sup>.

#### 1.11 Conclusions

My contribution to the advancement in the understanding of how these particles interact with lipid membranes stems from my synthetic work. The details of the syntheses and how they were scaled-up to allow multiple experiments can be found in the methods section. To produce sufficient amounts of amphiphilic gold nanoparticles based on MUS, and the relevant controls (cationic, zwitterionic, etc), gram-scale ligand syntheses had to be implemented (see methods). The syntheses outlined in this chapter, and detailed in the methods section, have enabled systematic studies to investigate, not only how nanoparticles interact with lipid bilayers<sup>116,120,145</sup>, but also viruses and proteins: my work during the past 4 years provided the material base for several different projects. Moreover, we have incrementally improved the synthesis and characterization of these particles, providing guiding principles and methods for making modified Stucky and one-phase syntheses readily accessible for new group members.

There are still challenges: for instance, syntheses tend to produce polydisperse samples, which means that species with completely disparate properties come from the same preparation. Below a certain diameter (around 1.7 nm) the electron distribution across gold nanoparticles no longer resembles that of bulk gold, but rather behaves as a *superatom* with defined orbitals <sup>150,151</sup>. This is a simple example of a size-dependent property that can affect experiments that rely on the traditional surface plasmon resonance at 520 nm of colloidal gold: below a certain size, this optical behavior collapses into a molecular orbital behavior. The approaches described above, following proper characterization and the possibility of size fractionation increase the degree of certainty and control over the sample.

The amphiphilic gold nanoparticles described in this section have shown unique properties that can be harnessed in biological research<sup>113,152</sup>. Interestingly, these particles behave not only like cell penetrating peptides<sup>125</sup> but also like the oligomeric species of the amyloid precursors described in the first part of this chapter, that also interact avidly with lipid membranes<sup>127</sup>. Furthermore, mature amyloid fibers have been shown to interact with cell membranes<sup>128</sup> and viruses<sup>129</sup>, which are two areas of on-going investigation in our group. Chapter 4 will show how the class of sulfonated amphiphilic nanoparticles interacts uniquely with the extended

surfaces of amyloid fibers. Moreover, we will show that these nanoparticles behave as colloidal surfactants, and bind preferentially to small oligomers of amyloid precursors before covering the mature fibers. Because small oligomers are likely to have higher surface tension than full fibers, analogous to classical nucleation and growth theory, the nanoparticle avidly "attack" the small oligomers before covering the grown fibers. The underlying mechanisms of nanoparticle amyloid-nuclei and fiber interaction is likely similar to that found with lipid bilayers, as demonstrated using molecular dynamics simulations: hydrophobic forces dominate unanticipated adsorption motifs. The degree of order adopted by the nanoparticles on the surfaces of the mature amyloid fibers have never been reported for a bio-nano interface that relies solely on secondary forces.

# 2 Using nanoparticles for amyloid research: statement of the problem

Chapter 1 reviewed how the building blocks of amyloid fibers self-organize, highlighting the current state of the literature for the peptides and proteins studied in this work. It emphasized the wealth of 3D polymorphisms that a single protein or peptide can adopt in the amyloid state. It also introduced a class of amphiphilic gold nanoparticles and summarized our main results regarding their lipid-bilayer fusogenic properties. The general outline on how the nanoparticles are prepared was given in the second part of the first chapter, and the detailed syntheses can be found in the Methods chapter. This chapter briefly discusses the current approaches that enable the understanding of the amyloid state described in the first part of chapter 1. It then reviews how nanoparticles have been used in biology, especially in the context of immunogold labelling and the current ambitious developments that aim to use gold nanoparticles as aides in the molecular structure determination of proteins through cryo-EM imaging. Finally, it states the hypothesis of this thesis: is it possible to design the ligand shell of gold nanoparticles such that it interacts with specific features on the surface of amyloid fibers without the intermediation of an antibody? Such development can provide the biological community a novel tool in the study of the amyloid state and proteins in general, and improve our understanding of how nanoparticles interact with proteins.

#### 2.1 Current approaches in the study of the amyloid fold

Chapter 1 focused on the definition of the amyloid fold and the different proposed structures obtained from NMR studies and X-ray diffraction of amyloid-like microcrystals<sup>23,24,27</sup>. Other techniques are routinely used to study amyloids, such as Atomic Force Microscopy<sup>77,153</sup>, fluorescence microscopy<sup>154</sup>, fiber X-Ray diffraction<sup>155</sup>, Fourier transform infrared resonance (FTIR)<sup>156,157</sup>, circular dichroism<sup>158</sup> among many other biochemical manipulations and tools. Particularly important are amyloidophilic dyes such as Thioflavin T (ThT) and Congo Red, that undergo an enhancement in emission in the presence of amyloids<sup>159</sup>. Most kinetic studies of how amyloid precursors assemble into amyloid fibers use ThT as the reporter molecule<sup>159</sup> and several important parameters about amyloid formation can be derived from kinetic studies<sup>160</sup>, for example the role of secondary nucleation in the formation of  $A\beta_{1-42}$  fibers<sup>161</sup>. Electron microscopy is commonly used to assess fiber morphology and dimensions using negatively stained techniques to observe dry samples. Scanning transmission electron microscopy (STEM) and dark-field EM are routinely used to determine the mass-per-length of amyloid fibers<sup>162</sup>: these values are used as constraints in the simulations performed to propose

the structures of mature amyloid fibers using the molecular contacts determined with NMR. Cryo-EM provides a good method to observe amyloid fibers (as well as viruses, proteins and other biostructures) in their native solvated state. Excluding potential (but limited) artefacts that can occur during sample preparation<sup>163</sup>, such as the formation of crystalline ice that can damage the sample, a well-acquired cryo-EM image can be used to propose structural models of complex biological assemblies such as the F-actin-tropomyosin complex<sup>164</sup>, and amyloid fibers as discussed in chapter 1<sup>80</sup>. Figure 2.1 summarizes some of the most commonly used biophysical tools in the study of the amyloid fold, including two different uses of ThT to interrogate amyloid-related phenomena.

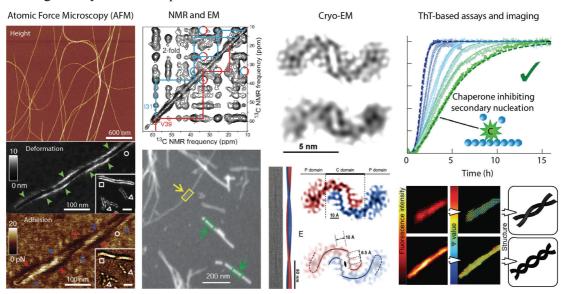


**Figure 2** From left to right, the most widely used (but not all) tools to study the amyloid fold. On the left, atomic force microscopy images (AFM) showing the typical 3D topographic images in dry state<sup>165</sup> and property-related imaging modes that can probe physical properties of the fibers<sup>77</sup>. As reviewed in chapter 1, NMR and dark field EM (most commonly STEM) to determine the mass-per-length of fibers are used to propose 3D structures of amyloid fibers<sup>39</sup>. Cryo-EM is successfully used to generate density maps that can be used to propose approximate structures of the fibers. The most commonly used probe for amyloid research is the dye thioflavin T (ThT), that can be used to track the kinetics of amyloid formation<sup>166</sup> or even to directly image the fibers and propose different polymorphs based on polarization-resolved fluorescence microscopy<sup>154</sup>.

#### 2.2 Use of gold nanoparticles in bio-electron microscopy.

The use of colloidal gold predates current-day nanoscience. The earliest documented use of gold nanoparticles for diagnostic dates back to 1912, when Dr. Lange reported that colloidal gold precipitated readily in the serum and cerebrospinal fluid of neuro-syphilitic patients<sup>167</sup>, an observation possibly related to the findings reported in this thesis. Rational approaches to control the assembly of gold nanoparticles using DNA were first reported in 1996<sup>168,169</sup>, shifting the paradigm in nanoscience towards controlled assembly of these nano building blocks. Meanwhile, gold colloids were routinely used as electron microscopy markers for

biological tissues from the 1970s onwards<sup>170</sup>. This technique relies on coupling suitable antibodies to colloidal gold, which is then added to microtomed tissue samples for electron microscopy, as schematized in Figure 2.2(a). Immunogold has been invaluable for immunocytochemistry, allowing biologists to identify spatiotemporal distribution of proteins in cells and tissues<sup>171</sup>.

Recently, the group of Roger Kornberg has recognized the enormous potential of using small gold nanoparticles as contrast agents in cryo-EM for protein whose structures cannot be determined with other techniques<sup>172</sup>. This approach relies on the conjugation of atomically precise 'ultrasmall' nanoparticles with the F<sub>ab</sub> fragment of an antibody, to establish 4 points in space that can be used to increase the resolution of the image reconstruction in cryo-EM<sup>173</sup>. This elegant approach to protein structural biology has one important caveat: the way nanoparticles interact with proteins, depending on the ligand shell that coats them, can influence the outcome. Can these non-specific interactions interfere with the way these molecular immunogold labels attach to the proteins and hence interfere with the interpretation of the image? Briefly, what properties on the nanoparticle ligand-shell determine its interaction with proteinaceous materials, and are there energetically favorable interactions for a given type of nanoparticle with certain structures on the surfaces of proteins? Figure 2.2 summarizes the immunogold approach, and shows a recent cryo-EM of neuraminidase 'decorated' with nanoparticles conjugated to the F<sub>ab</sub> segment of an antibody (Figure 2.2(b)).

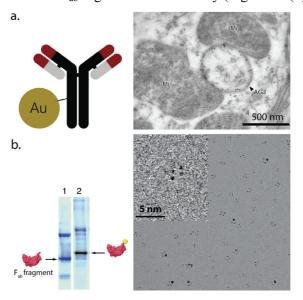


**Figure 2 (a)** Classical immunogold labeling approach. A gold colloid is conjugated to an antibody, which is then added to a microtomed sample, for EM imaging. On the right, a TEM of a heart cell with immunogold labels for connexin  $43^{171}$ . **(b)** Arguably the state of the art in the use of gold nanoparticles in biology: the conjugation of atomically precise gold nanoparticles to the  $F_{ab}$  fragments of antibodies, to label single proteins in 3D. The nanoparticles serve as a cryo-EM staining agent,

#### 2.3 Statement of the problem

Amyloid fibers have been extensively studied using the probes described so far. Following the rationale proposed by the Kornberg group, this thesis aims to establish the properties of a gold nanoparticle that allow it to interact discriminatively with mature amyloid fibers. In others words, given a twisted ribbon fiber, what are characteristics that lead the nanoparticles to adsorb preferentially to one facet of the cross-section of the fiber, and not the other? Amyloid fibers are arguably the most generic protein fold, accessible to several polypeptides as reviewed in chapter 1<sup>174</sup>: thus, to test the discriminative behavior of nanoparticles towards fibrous protein aggregates, amyloids provide a good common denominator. On the other hand, this limits our ability to interpret what structures the nanoparticles spontaneously adsorb onto, given the current uncertainties regarding the molecular structure of mature amyloid fibers. Nonetheless, it raises several opportunities to elucidate the contacts established between the ligands on the gold nanoparticles and the amyloid fibers, which can help the understanding of amyloid fiber structure.

It is impossible to predict how different parameters influence the way gold nanoparticles interact with amyloid fibers or proteins in general. To this end, different types of particles, that are colloidally stable in buffered conditions, have been tested with four types of amyloid fibers:  $A\beta_{1-40}$  and  $A\beta_{1-42}$ ,  $\alpha$ -synuclein and Tau-441. These polypeptides were chosen because of their relevance in neurodegenerative diseases (Alzheimer's, Parkinson's among others) and the different types of fibers they form. For example,  $\alpha$ -synuclein contains several acidic residues in the C-terminal, which renders it more electronegative than the other two types. Tau-441 has long disordered segments while  $A\beta$  has much shorter ones: these key differences enable us to study the interaction between different types of gold nanoparticles prepared via ligand synthesis, with fundamentally distinct, medically relevant, amyloid fibers. Several types of particles are tested, emphasizing first the role of charged end groups on the thiolate ligands that protect the gold core, followed by an in-depth analysis of the discriminative adsorption of small amphiphilic sulfonated NPs, that hold the potential to become a useful tool in the study of amyloids and proteins in general.

### 3 Interaction of charged gold nanoparticles and amyloid fibers

#### 3.1 Overview

Different types of water soluble monolayer-protected gold nanoparticles were prepared and tested with amyloid fibers made of  $A\beta_{1-40}$ ,  $\alpha$ -synuclein and Tau-441. Nanoparticles protected by phosphate-terminated thiols did not interact significantly with the fibers but aggregated with other nanoparticles. Cationic nanoparticles adsorbed to the particles cooperatively and indiscriminately, while zwitterionic nanoparticles did not interact, in agreement with the previous reports on the protein adsorption resistance of mixed charge surfaces  $^{114,115}$ . On the other hand, MUS and MUS:OT particles, adsorb onto the fibers, and depending on their diameter, do so discriminatively. The latter will be critically analyzed in the next chapter. This chapter shows how mature amyloid fibers interact with these different nanoparticles. Most findings here can be roughly explained by coulombic interactions, but other parameters are discussed such as hydrophobicity and the strength of the solvation shell that surrounds zwitterionic nanoparticles.

#### 3.2 Prior nanoparticle-amyloid fiber interactions

There are several reports of amyloid fibers decorated with gold nanoparticles. To our knowledge, apart from three exceptions<sup>175-178</sup>, all other gold nanoparticle decorated amyloid fibers result from immunogold staining. Researchers used immunogold to ascertain the nature of their fibrils or identify their association with other proteins, producing TEM images that resemble the data shown in this project<sup>179-181</sup>. Other groups, especially Prof. Linse's, has laid the foundations for amyloid-nanoparticle research, but did not focus on adsorption.

Previous nanoparticle-decorated amyloid fibers can be categorized as: (1) immunogold labelled samples, illustrated by Figures 3.1(d) and (e) (2) non-specific nanoparticle amyloid adsorption, seen in Figure 3.1(a)-(c), and (3) amyloid directed synthesis of metallic nanostructures<sup>178,182</sup>. The last item is less relevant for our results, and the reader can consult references (182) and (178). A non-specific interaction means that no bio-recognition or covalent bonding scheme was used. Instead, the interactions result from secondary forces such as electrostatic contacts, van der Waals forces and hydrogen bonds that determine how nanoparticles interact with amyloid fibers.

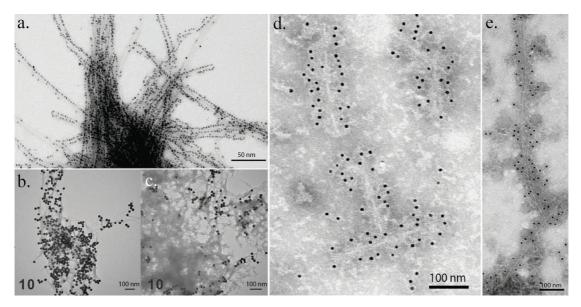


Figure 3.1 (a) Anionic colloidal gold used on  $Aβ_{1-40}$  fibers to demonstrate that, despite an overall negative charge, the fibers possess dense regions of positive charges on their surfaces. (b) Use of citrate stabilized gold nanoparticles to slow the formation of  $Aβ_{1-40}$  fibers showed, in the end, particles that associated randomly with the fibers. (c) The authors show that the particles interact with the fibers but not the amorphous non-fibrillar material seen in the sample. (d) Tau filaments from mouse model AD brain, immunostained with gold nanoparticles coated with antibodies BR134 and Tau-C3 (e) Use of nanoparticles coated with PER4 antibody to demonstrate that fibers extracted from Lewy Bodies of a patient with dementia were made of α-synuclein. Figure (a) reproduced with permission from reference (176) Copyright © 2007, American Chemical Society. (b) and (c) reproduced with permission from reference (175) Copyright © 2012 WILEY-VCH Verlag GmbH & Co. KGaA, Weinheim. (d) Reproduced with permission from reference (179) Copyright © 2008 American Society for Investigative Pathology. Published by Elsevier Inc. All rights reserved and (e) reproduced with permission from reference (180) copyright © by the National Academy of Sciences.

## 3.3 Cationic nanoparticles adsorb indiscriminately and cooperatively onto amyloid fibers

Figure 3.1(a) shows the published image that most resembles our own<sup>176</sup>. Yoshiike et al. argues that, despite being net-negatively charged (-3 at neutral pH),  $A\beta_{1-40}$  fibers have cationic regions along its surface, that respond for their interaction with anionic lipid bilayers<sup>183</sup> and cytotoxicity<sup>176</sup>. The study uses negatively charged colloidal gold to demonstrate the existence of discrete cationic features along the surface of the fibers. The image shown in Figure 3.1(a) is a dry TEM and reveals an ordered nanoparticle assembly on the edges of the fibers. They chemically modify basic amino acid side groups via glycation and acetylation (likely K16 and K28) to demonstrate that the particle-fiber binding is due to coulombic interactions, thus proving the existence of lines of positively charges on the surface of the fiber.

These lines are predicted by the detailed structural models reviewed in chapter 1, because the in register parallel packing of beta sheets can align lysine side groups (K16) along the surface of the fiber. The authors of Figure 3.1(a) may have adsorbed their negatively charged colloidal

gold onto these lines due to electrostatic attraction. We have observed a similar phenomenon with positively charged particles. Our results suggest that coulombic forces alone cannot explain how monolayer-protected gold nanoparticles interact with amyloid fibers: we have observed an aggregation behavior of cationic particles that contradicts Figure 3.1(a), in addition to other fiber-binding nanoparticles with disparate charges and ligand-shell compositions. From our results, in addition to coulombic interactions, the hydrophobic effect plays a definitive role in mediating how gold nanoparticles interact with amyloid fibers

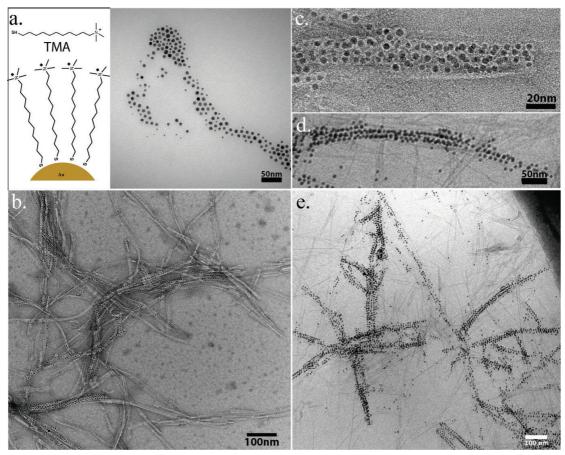


Figure 3.2 (a) Schematic representation of cationic nanoparticles, and the corresponding ligand, N,N,N-Trimethyl(11-mercaptoundecyl)ammonium Chloride (TMA) used in their synthesis. On the right, a bright-field TEM image of the particle batch used in these experiments. The size distribution is  $3.9 \pm 1.6$ nm: there are enough different NP diameters in this batch to capture eventual size-selectivity. (b) TEM of negatively stained (2% Uranyl acetate)  $A\beta_{1-40}$  mature fibers, with allTMA NPs. Aggregation and sedimentation was obvious in the sample: under EM, the particles bind cooperatively on the mature fibers, and seem to induce fiber-bundle formation. (c) Higher magnification of the same sample (bar 20 nm) (d) Crop from (e), a cryo-EM of the same sample, showing that the cooperative indiscriminate coverage of fibers and bundle formation are not drying artefacts. Images in (a), (b) and (c) were obtained in an FEI TALOS<sup>TM</sup> Electron Microscope and the cryo-EM image (e) and its crop (d) in an FEI Tecnai<sup>TM</sup> Spirit BioTWIN.

Cationic nanoparticles coated only with the positively charged thiolate molecule TMA, (N,N,N-Trimethyl(11-mercaptoundecyl)ammonium Chloride) were prepared following modifications on the Stucky protocol described in chapter 2, and detailed in the methods

section. A batch with size distribution of  $3.9 \pm 1.6$ nm was purified and characterized (see methods), dispersed in Milli-Q water and filtered through a 0.2 µm PTFE syringe filter to an approximate particle concentration of 2 mg/mL. Due to polydispersity, we report nanoparticle concentrations in mass per volume: it is difficult to determine molar amounts, but in the size range between 2 to 4 nm, a 1 mg/mL solution falls in the micromolar regime. A $\beta_{1-40}$  fibers were prepared following the protocol described in the methods section: briefly, after ultracentrifuging the monomeric solution, the concentration was adjusted to about 10 µM by absorbance using pH = 7.2, 13 mM sodium phosphate buffer (50 mM NaCl). The solution was agitated at 37°C (300rpm for the fibers in Figure 3.2) and fiber growth was monitored by thioflavin T (ThT) fluorescence and electron microscopy. Once mature  $A\beta_{1-40}$  fibers were formed, 10 µL of the nanoparticle stock solution was added to 90 µL of the fiber suspension. This step changes the ionic strength of the buffer, because the nanoparticle Milli-Q water vehicle dilutes the buffer. Although proteins can be sensitive to changes in salt concentration, this buffer-dilution is unlikely to affect our results. If it does, it has been a consistent parameter throughout the different experiments, which does not change comparisons between different particles. The mixture was then allowed to incubate at 37°C and 300 rpm agitation for periods from 2 to 12 hours. Figure 3.2 shows a 12 h incubation. The samples were analyzed and stored at 4°C.

Whenever TMA protected cationic gold nanoparticles were added to the fiber suspension, the solution turned slightly red, and macroscopic aggregation ensued within 5 to 10 minutes. The phenomenon can be described as flocculation, because discrete red aggregates formed and precipitated, clearing the supernatant. Vigorous agitation suspended these aggregates, but once the mechanical stimulus ceased, they sedimented to the bottom of the vial. Electron microscopy reveals that TMA-protected gold nanoparticles adsorbed cooperatively onto the fibers. Several undecorated fibers can be seen on the TEM grid, as depicted in Figure 3.2(b) and also under cryo-EM in Figure 3.2(e). Titration with higher nanoparticle concentrations, to test whether all fibers can be covered has not been done yet. Nonetheless, the observations made so far suffice to discuss the cooperative adsorptions of allTMA nanoparticles onto amyloid fibers.

Following Yoshiike's reasoning, cationic particles bind to the fibers because of an electrostatic attraction: the fibers are net-negative and the particles positive, therefore coulombic interactions dictate their association. This is probably the dominant driving force, but in

addition to the hydrophilicity conferred to TMA by the quaternary amine, the three methyl groups render it amphiphilic: for example, these particles are soluble in absolute ethanol. This observation suggests that hydrophobic interactions can be an additional driving force.

If the adsorption of negatively charged particles reveals the presence of discrete cationic regions, our observation indicates similar anionic regions or the absence of strong enough cationic features to repel allTMA nanoparticles. From the models described in chapter 1, the in register cross beta sheet arrangement can force charged side groups to concentrate along the body of the fiber, thus both cationic and anionic features can exist in this configuration. The amyloid fiber surface, depending on the constituent polypeptide and the polymorphism, can be a complex nanostructured zwitterionic surface. For  $A\beta_{1-40}$ , cationic rows of lysine 16 are as probable as anionic lines of glutamic acid 22, depending on the polymorph. In reality, high-density regions of both negative and positive charges can co-exist on the surface of amyloid fibers and can be responsible for many of their physicochemical and biological properties.

Our observation does not demonstrate the existence of specific anionic surface features on the  $A\beta_{1-40}$  fibril. Instead, it points to an electrostatic potential minimization via charge pairing and a cooperative adsorptive behavior. Once a nanoparticle lands on the fiber, it may lower the energy barrier for vicinal adsorption (likely by electrostatic shielding), which successively leads to total coverage. The nanoparticles do not seem to prefer edges or faces, but form multiple rows along the length of the fiber. Therefore, a combination of electrostatic attraction, hydrophobic interactions and charge screening allows cationic TMA-protected gold nanoparticles to cooperatively and indiscriminately coat  $A\beta_{1-40}$  fibers. This effect seems to be accompanied by a fiber-bundling behavior that may result from the elimination of repulsive interactions between different fibers. This is flagrant when the same experiment is performed with α-synuclein, as shown in Figure 3.3. In this case, the transition from randomly oriented fibers on the TEM grid, to bundles, correlates with the presence of allTMA particles. Figures 3.3(a) and (b) show two images of the same grid, in which undecorated fibers are randomly oriented, whereas the covered ones adopt collective bundled orientations. Depending on the preparation, amyloid fibers have a tendency to agglomerate and form bundles. But the intertwined rope-like aggregates observed in these experiments were mediated by the presence of allTMA nanoparticles. On the top part of Figure 3.3(b), the fibers are not densely covered by particles and lie separated on the grid, in different orientations. In the region where fibers are densely coated by allTMA nanoparticles, the fibers become interlaced.

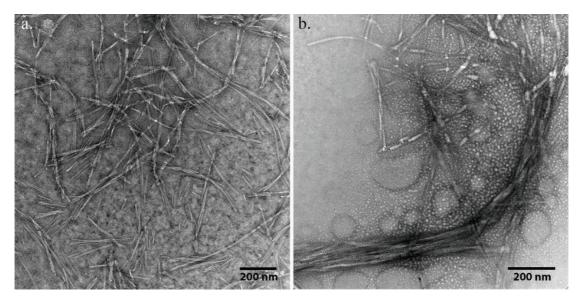


Figure 3.3 Interaction of  $\alpha$ -synuclein with allTMA nanoparticles. (a) Portion of the grid without allTMA particles. A few nanoparticles are visible in the center, but overall the fibers are clear and randomly distributed. (b) When  $\alpha$ -synuclein fibers interact with allTMA particles, they self-associate on the grid and form bundles of particle-decorated fibers. The dark loop in the image contains densely packed nanoparticle-fiber associations. Images obtained in an FEI TALOS<sup>TM</sup> Electron Microscope.

Figure 3.4(a) reveals that allTMA nanoparticles may first adsorb onto the edges of  $\alpha$ -synuclein fibers. This challenges the indiscriminate mode of adsorption attributed to these particles for A $\beta_{1-40}$  fibers. Perhaps, nanoparticle chains nucleate and grow on the surface of the fibers, because of the lower free energy barrier for vicinal adsorption. The inherent propensity of allTMA nanoparticles to aggregate in the presence of biomolecules may be related to this phenomenon. The interparticle distance along the edge of the fiber in Figure 3.4(a) is around 3.5 nm. The same approximate distance is measured for lines of particles in the cryo-EM image in Figure 3.4(c).

On the other hand, cryo-EM does not show evident edge-binding: the fibers may act as a scaffold that, upon drying, organizes the particles into the arrangement seen in the dry sample (Figure 3.4(a)). In liquid, (cryo-EM) the particles are less ordered, and once a chain of particles form, instead of following the contour of the fibers, they terminate abruptly (Figure 3.4(c)). This creates several short strings of particles that seem to follow an orientation, as highlighted by thin dotted white lines in Figure 3.4(c). Their similar orientations can stem from the helical nature of the fiber: once a line of particles begins to follow the edge, because of its stiffness, it

cannot continue along the fiber contour, so it truncates. Figure 3.4(d) shows fibers covered with nanoparticles, in which the particle superlattices appear less rigid and follow the curvature of the fiber. In these cases, the fibers are densely coated by the nanoparticles, without any preference to an obvious underlying fibril-morphology feature, hence the categorization of non-discriminative adsorption, despite the organization seen in Figure 3.4(a). The cryo-EM image captures the solvated state, so it is given more weight to develop the final interpretation.

The  $\alpha$ -synuclein fibers intertwine, either due to loss of inter-fiber screening, or gain of an adhesive property mediated by allTMA nanoparticles. This effect was also observed for A $\beta_1$ -40 fibers, but is more pronounced with  $\alpha$ -synuclein. The zeta potential of allTMA particles is about +40 mV (in water), and that of  $\alpha$ -synuclein fibers has been reported to be approximately -23 mV at neutral pH<sup>184</sup>. Therefore, fiber bundling may reflect a point of zero charge coprecipitation, whereby the allTMA nanoparticles screen the electrostatic repulsions between the fibers, causing the coated fibers to interlace; or the nanoparticles screen the repulsive interactions between different fibers, which leads to fiber-weaving. The bundles have not been as evident under cryo-EM: the ice was too thick around regions that potentially contained these structures.

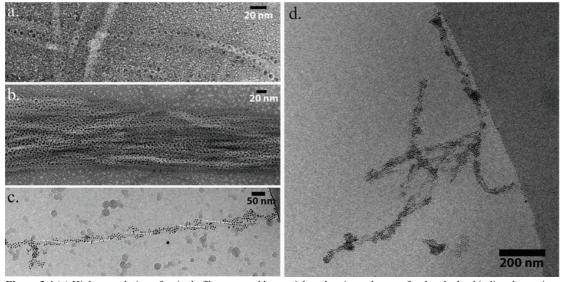
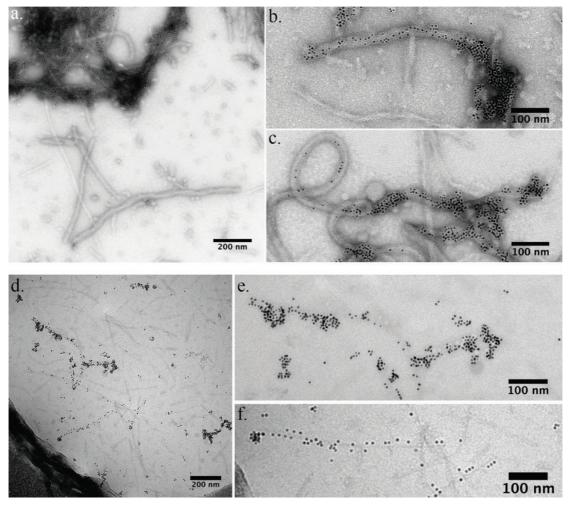


Figure 3.4 (a) Higher resolution of a single fiber covered by particles, showing a degree of ordered edge binding decoration. (b) Same image of a bundle of nanoparticle-covered fibers, in which the ordered adsorption is less clear. (c) Cryo-EM of a single α-synuclein fiber with allTMA nanoparticles: no specific morphology is discernible. (d) Cryo-EM of the same sample, showing full "disordered" coverage of the fibers. Images in (a) and (b) were obtained in an FEI TALOS<sup>TM</sup> Electron Microscope and (c) and (d) in an FEI Tecnai<sup>TM</sup> Spirit BioTWIN.

When Tau-441 fibers were mixed with allTMA nanoparticles, the macroscopic precipitation, described above as flocculation was not observed. The Tau-441 fiber preparation produced a high density of fibers, as seen in Figure 1.5(c). To accommodate for the higher number of fibers, the concentration of the allTMA nanoparticle stock solution was increased by a factor of 4. Despite this precaution, most fibers were free of nanoparticles. Both negatively stained dry TEM and cryo-EM images were taken for this sample, and looked similar. Figure 3.5 shows representative electron micrographs of Tau-441 fibers and non-fibrillar species in the presence of allTMA nanoparticles.



**Figure 3.5 (a)** Typical allTMA aggregate found in Tau-441 samples along the fibers. **(b)** Some fibers can be found with particles on their surfaces. **(c)** Another example of how allTMA particles distribute across a Tau-441 fiber sample. **(d)** Cryo-EM of the same sample, show several non-decorated fibers. **(e)** Higher resolution of the same sample. **(f)** Crop from **(d)** showing particles that line a fiber. Dry images obtained in an FEI TALOS<sup>TM</sup> Electron Microscope and Cryo-EM images FEI Tecnai<sup>TM</sup> Spirit BioTWIN.

Fibers of Tau-441 can be approximated to a rigid amyloid core, surrounded by a charged polymer brush. The protein is 441 residues long, but residues from 1 through 243 and from 370

to 441 tend to not participate in the cross beta sheet formation. Instead, they form a layer of disordered peptide chains called the fuzzy coat. It acts as a polymer brush with a positive interior and negative exterior at neutral pH, that determines the adhesive properties of the fiber<sup>77</sup>. The allTMA nanoparticles have a tendency to aggregate in the presence of proteins, and this can partly explain the agglomerates seen in the images. The properties of the surface of Tau-441 fibers dictate how allTMA particles interact with them, because the results differ considerably from the observations made with  $A\beta_{1-40}$  and  $\alpha$ -synuclein. allTMA nanoparticles probably interact with these fibers via electrostatic forces:  $\alpha$ -synuclein fibers have more electronegative surfaces, onto which cationic particles bind, which screens the inter-fiber repulsions and interlace them. Instead, the zwitterionic fuzzy coat that surrounds Tau-441 fibers favors peptide-water interaction<sup>146</sup> which generates a small driving force of adsorption.

# 3.4 Zwitterionic nanoparticles do not bind to amyloid fibers

The importance electrostatic interactions can be demonstrated by modifying the thiol end-group, with the introduction of a sulfonate moiety following the quaternary amine. This produces a sulfobetaine terminated thiol 3-[(11-Mercapto-undecyl)-N,N-dimethyl-amino]-propane-1-sulfonate<sup>115</sup> abbreviated here as ZW ligand (Figure 3.5(a)). Zwitterionic surfaces have been reported to resist non-specific protein adsorption<sup>115</sup>, and nanoparticles protected by these types of ligands do not form protein corona *in vitro*<sup>114</sup>. This class of ligands serves as an adequate control to assess the importance of electrostatic interactions between nanoparticles and macromolecules.

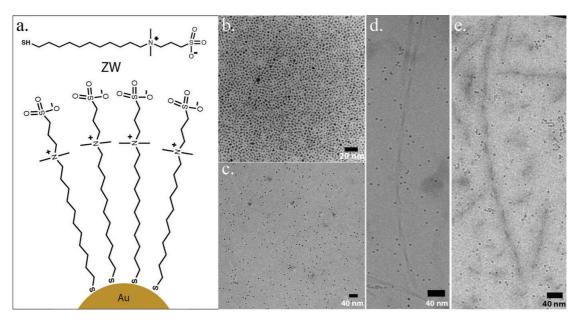


**Figure 3.6 (a)** Molecular structure of 3-[(11-Mercapto-undecyl)-N,N-dimethyl-amino]-propane-1-sulfonate, and a schematic depiction of the nanoparticle produced with it. (b) Dry TEM image of the nanoparticle batch,  $2.9 \pm 0.9$  nm. The particles cover the grid densely. (c) A cryo-EM image of the nanoparticles in the preparation with  $Aβ_{1-40}$  fibers. This image illustrates the colloidal stability of these particles, that distribute evenly through the buffer. (d) Crop of a Cryo-EM image of  $Aβ_{1-40}$  fibers to which ZW NPs were added. No binding is observed. (e) Crop of a cryo-EM of Tau-441 fibers, to which ZW NPs were added, no binding was observed on the fibers. Image (b) was obtained in an FEI TALOS<sup>TM</sup> Electron Microscope and (c)-(d) in an FEI Tecnai<sup>TM</sup> Spirit BioTWIN.

Zwitterionic nanoparticles (ZW NPs) were synthesized following a modification to the Stucky approach (see methods) which yielded nanoparticles of 2.9 ± 0.9 nm. In experiments with amyloid fibers, no aggregation or precipitation was observed. Instead, the samples maintained the red color of the nanoparticle dispersion, which indicates the particles are colloidally stable in the presence of amyloid fibers. Even centrifugation at 13000 g for 10 minutes did not create a red pellet: instead, a pale aggregate accumulated at the bottom of the tube, and the solution remained red. The fibers sedimented while the nanoparticles remained in solution. These nanoparticles have a zeta potential of -9.2 ± 0.2 mV, which, at a first glance, might explain their inertness towards amyloid fibers. Both fibers and particles are net-negative, thus mutually repellant. This explanation does not agree with (1) Yoshiike's results <sup>185</sup> and (2) the fact that MUS nanoparticles bind, and have a zeta potential ranging from -35 to -60 mV depending on NP size. These results show that negatively charged particles do adsorb onto the fibers, therefore, it is unlikely that the slight electronegativity of ZW NPs is responsible for its inertness.

These results must be interpreted in the context of protein-fouling resistant surfaces. Ethylene glycols (EGs) are the materials of choice for manufacturing protein-resistant surfaces <sup>186,187</sup>.

Zwitterionic surfaces resist non-specific protein adsorption more efficiently than EGs *in vitro* and *in vivo*<sup>114,187</sup>. Both moieties form hydration shells that need to be disrupted for a protein to adsorb, and the unfavorable rearrangement of water molecules exert a repelling force against protein adsorption<sup>188</sup>. Zwitterionic monolayers form dense electrostatically based water shells that must pay a high free energy penalty to accommodate a protein<sup>188</sup>. This culminates in a repellant force against protein-zwitterionic contacts, whereas the EG hydrogen bond based water network is suppler, hence exerts a smaller repellant force<sup>188</sup>.

To date, zwitterionic molecules ending in sulfobetaine or phosphorylcholine head-groups form the most efficient surfaces against non-specific protein adsorption. Mixing individually charged ligands on a surface can outperform the single-molecule zwitterions as indicated by Holmlin et al. 115. The zwitterionic nanoparticles used in these experiments with  $A\beta_{1-40}$  fibers (Figure 3.6(d)) and Tau-441 fibers (Figure 3.6(c)) do not interact with the fibers because the energy cost to rearrange the water shell around the zwitterionic groups generates a repulsive force that prevents them from adsorbing onto the fibers  $^{187}$ . Figure 3.7(a) shows how  $A\beta_{1-40}$ fibers form aggregates, without affecting the colloidal distribution of ZW NPs. These fiber aggregates differ from the allTMA NPs-induced  $\alpha$ -synuclein fiber interlacing. In this case,  $A\beta_{1-40}$  fibers have a tendency to aggregate which does not affect the stability of the ZW NPs. Figure 3.7(b) compares this aggregation to the evenly distributed Tau-441 fibers in solution. The zwitterionic nanoparticles are also well-distributed throughout the buffer, but show signs of local aggregation. The clear disconnect between particles and fibers in these images reveal why under centrifugation, a pale pellet is observed while the supernatant remains red, proving that nanoparticles remain in solution. To test if hydrophobic interactions can overcome the repulsive forces that prevent zwitterionic nanoparticles from interacting with amyloid fibers, we will introduce hydrophobic moieties to the nanoparticle monolayer.

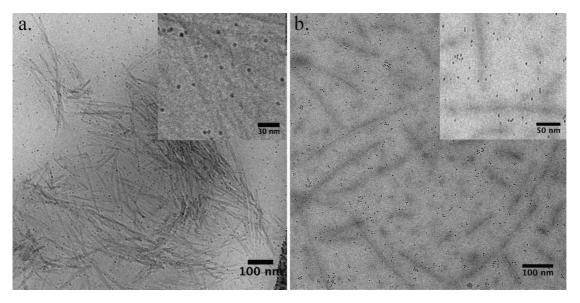


Figure 3.7 (a) Cryo-EM of  $Aβ_{1.40}$  fiber aggregate in the presence of ZW NPs. The nanoparticles are stable even in the presence of strongly aggregative species. Inset shows a crop from the same set of images to help visualize the nanoparticles (b) Tau-441 fibers with ZW NPs. In this case, the fibers do not aggregate as much among themselves, and the particles also remain well dispersed in solution. The inset is a crop from the same set of images, to help visualize the nanoparticles. Imaging Tau-441 fibers under cryo-EM posed a challenge: the focus plane of nanoparticles differed from the fibers. The inset if a compromise between both, to show the fibers and particles. Cryo-EM images obtained in an FEI Tecnai<sup>TM</sup> Spirit BioTWIN.

# 3.5 Negatively charged nanoparticles

We have shown that an adsorptive and aggregating phenomenon can be eliminated by chemically converting the positively charged quaternary amine into a zwitterionic sulfobetaine group. This chemical modification changed the aggregation behavior of the nanoparticles, and their interaction with amyloid fibers. Now, we show that anionic nanoparticles can effectively adsorb onto amyloid fibers, depending on their ligand shell composition: anionic particles with a higher hydrophobic content adsorb more effectively onto  $A\beta_{1-40}$  fibers, but this parameter did not alter the interaction with  $\alpha$ -synuclein fibers. These results suggest that hydrophobic interactions are important to generate nanoparticles capable of interacting preferentially with specific surface features of the amyloid fibers. Negatively charged nanoparticles can be synthesized using different types of ligands, terminated in head-groups such as carboxylic acids, phosphates and sulfonates. Nanoparticles protected by carboxylic acids are water soluble, but tend to precipitate in standard biological buffer conditions: this makes them ill-suited for these experiments. Phosphate and sulfonate headgroups confer buffer solubility to gold nanoparticles, rendering them good candidates for this work.

Figure 3.8 shows that nanoparticles protected by 11-Mercaptoundecylphosphoric acid (MUP) synthesized via the one phase method (bimodal distribution,  $2.74 \pm 1.32$  nm), despite good

buffer solubility, did not interact with the  $A\beta_{1-40}$  fibers, but rather, tended to aggregate. Figure 3.8(a) shows the chemical structure of the ligand and a schematic depiction of the nanoparticle. Figures 3.8(c)-(e) are cryo-EM images of allMUP NPs with  $A\beta_{1-40}$  fibers. Nanoparticle aggregation dominated the samples, and no obvious fiber-particle interactions could be observed. During sample preparation, the macroscopic behavior is reminiscent to that of allTMA nanoparticles. After addition of the red nanoparticle stock solution, the amyloid fiber suspension becomes red, followed, after 5 to 10 minutes, by the formation of a purple precipitate and a clear supernatant. Unlike the allTMA experiments, when the pellets were red, these form large purple flecks. In principle, these particles should interact with the proposed positive charges on the surface of the  $A\beta_{1-40}$  fibers <sup>176</sup>, but instead, the ionic content of the buffer probably screens inter-particle repulsions which in the presence of small amounts of A\(\beta\_{1-40}\) monomers and oligomers, drives aggregation. These particles have not been thoroughly studied, but these images serve as an example that gold nanoparticles do not interact with amyloid fibers simply by virtue of size, charge and buffer solubility. The properties of the ligand shell determine the bionano interface, as exemplified in the two previous cases. It is, however, possible that allMUP can adsorb onto other types of fibers.

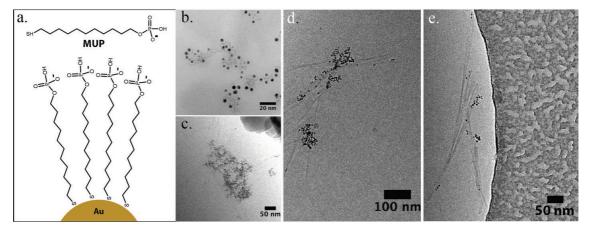


Figure 3.8 (a) MUP ligand and a schematic depiction of a gold nanoparticle protected by it. (b) TEM image of the nanoparticles after the synthesis. This batch had a bimodal size distribution, but overall, the sizes were  $2.74 \pm 1.32$  nm. This undesirable polydispersity is an advantage for this experiment, because it would allow us to observe size-dependent phenomena (c) Cryo-EM image of  $A\beta_{1-40}$  in the presence of allMUP NPs. The nanoparticle aggregate is the main feature in these samples. (d) and (e) Additional cryo-EM images of  $A\beta_{1-40}$  fibers and allMUP nanoparticles showing no organized interaction. Both fibers and nanoparticle aggregates are visible. (b) was acquired in an FEI TALOS<sup>TM</sup> Electron Microscope and the Cryo-EM images in an FEI Tecnai TM Spirit BioTWIN.

When the sulfonate-based nanoparticles described in chapter 2 were added to amyloid fiber preparations, we observed different modes of adsorption. The nanoparticle-fiber interaction depended on the size of the nanoparticles and ligand-shell composition. The negatively charged

allMUS and MUS:OT particles bind to all three fibers tested in this thesis, but the presence of OT in the ligand-shell improves the adsorption of small nanoparticles onto  $A\beta_{1-40}$  and Tau-441 fibers. When  $\alpha$ -synuclein fibers were used, we saw no significant differences between allMUS and MUS:OT under cryo-EM, but a size-selection phenomenon was detected: the smaller nanoparticles adsorbed onto the edges, while the larger ones aggregated in the surroundings.

When a batch of allMUS nanoparticles synthesized via the one phase method ( $2.42 \pm 1.77$  nm), was added to A $\beta_{1.40}$  fibers no discernible fiber adsorption was observed under negatively stained dry TEM imaging (Figures 3.9(c) and (d)). The particles were added to the fiber mixture and kept under 300-1000 rpm agitation at 37°C for 2 to 12h depending on the experiment: no precipitation was observed under these conditions. Only after overnight storage at 4°C, a red band or pellet developed, clearing the supernatant: this behavior varied across experiments. The sample was re-suspended (using vortex or pipetting), and grids prepared for negatively stained TEM imaging: Figures 3.9(c) and (d) show the typical image of allMUS NPs with A $\beta_{1.40}$  fibers. These particles did not seem to adsorb with any degree of order onto the fibers, and scattered particles could be seen over the grid, usually aggregated close to the fibers. However, when this sample was size-fractionated in a sucrose gradient (Figure 3.9(f)), which removes larger particles and decreases the polydispersity (2.65  $\pm$  0.92 nm) and potentially 'worse' particles, the same experiment revealed avid A $\beta_{1.40}$  decoration, as seen in Figure 3.9(f).

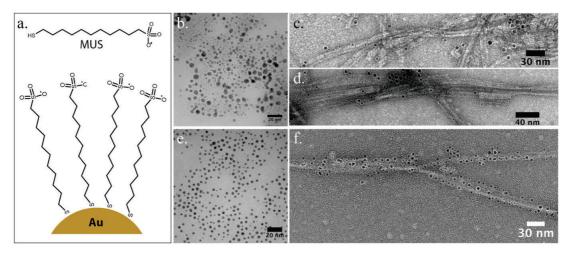


Figure 3.9 (a) Molecular structure of MUS ligand and schematic depiction of the allMUS nanoparticle. (b) TEM of a one-phase synthesized allMUS nanoparticle batch. The size distribution is wide (see methods). (c) and (d) Typical images of  $A\beta_1$ .

40 with the nanoparticles depicted in (b). In dry microscopy, some binding is detectable, but a lot of particles distribute randomly across the grid. (e) The same batch after fractionation, that eliminates most of the particles above 4 nm (2.65 ± 0.92 nm). (f) Using the fractionated nanoparticles, the  $A\beta_{1-40}$  fibers were decorated. Image (c) was acquired in a Philips CM12 TEM all others in an FEI TALOS<sup>TM</sup> Electron Microscope.

The addition of 1-octanethiol (OT) to the nanoparticle ligand shell changed their adsorptive behavior onto  $A\beta_{1-40}$  fibers. Different ratios of MUS to OT were used, as shown in Figure 2.7. In this work, to address the effect of nanoparticles on the aggregation kinetics of amyloid precursors, each MUS to OT stoichiometry was synthesized in triplicates. This means that separate nanoparticle batches prepared with MUS:OT ratios of 9:1, 8:2, 7:3 all the way to 1:9 and all OT were prepared, three times each, using the one phase method. A similar approach is on-going for Stucky particles, albeit more laborious. Unfortunately, experiments that rely on EM cannot afford the verification of each type of nanoparticle: electron microscopy is not a high throughput technique. Whenever we added MUS:OT nanoparticles with 10% and 30% OT by <sup>1</sup>H-NMR (feed ratio 7:3 and 1:1 respectively, see Figure 2.7 and Methods) to Aβ<sub>1-40</sub> fiber suspensions, they adhered onto the fibers as observed under dry negatively stained TEM. Given the observation made with allMUS nanoparticles, that size-fractionation changed adsorptive behavior, the same experiment was performed for an MUS:OT NP batch with 30% OT. No change in adsorption was observed between fractionated and unfractionated MUS:OT nanoparticles, i.e. small changes in polydispersity did not affect how these amphiphilic nanoparticles adsorb on the fibers. When the image in Figure 3.9(f) is compared to those in Figures 3.10(c), (e) and (f), the association between the MUS:OT nanoparticles and the fibers seems qualitatively tighter than fractionated allMUS. These observations indicate the importance of hydrophobicity in promoting the adsorption of 1-3 nm anionic particles onto amyloid fibers. Furthermore, the fractionation might be excluding low-quality nanoparticles with poor surface coverage, and large particles that induce particle-particle aggregation before they can reach the surfaces of the fibers. This may explain Figure 3.9(f): under cryo-EM, nanoparticles containing OT pack more densely on the Aβ<sub>1-40</sub> fibers, which confirms the observations made with dry TEM.

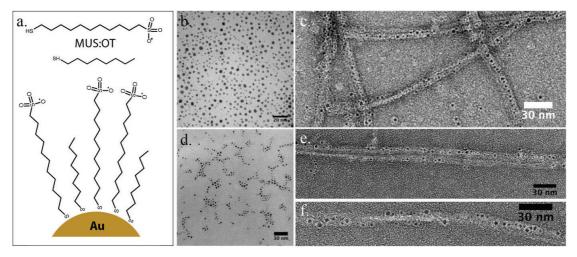


Figure 3.10 (a) Molecular structure of the ligands used: MUS and 1-octanethiol in addition to a schematic rendition of the nanoparticle ligand shell. (b) A TEM of an unfractionated batch synthesized via the one phase method  $(2.62 \pm 1.4 \text{ nm})$ . The OT content by  $^1\text{H}$ -NMR was 30% (the MUS:OT feed ratio in the reaction was 1:1) (c) Representative image of  $A\beta_{1.40}$  fibers in the presence of MUS:OT nanoparticles. The fibers were covered by nanoparticles that seemed to be embedded with the cores of the fibers. (d) The same nanoparticle batch after fractionation, which produced sizes of  $2.40 \pm 0.98 \text{ nm}$ . (e) and (f) show that fractionation did not change the adsorptive behavior. Image (c) was acquired in a Philips CM12 TEM, and the others in an FEI TALOS<sup>TM</sup> Electron Microscope.

In a prelude to chapter 4, to ensure the observations in Figure 3.10(a) is not a drying artefact, a series of cryo-EM images were obtained. These images confirmed that MUS:OT NPs cover fibers more densely than allMUS, and that small particles adsorb onto the edges of twisted ribbon fibers. Both types of particles adsorb preferentially on the edges of the fibers, but MUS:OT nanoparticles decorate these features at longer length scales, more reproducibly across different experiments and seem to establish a tighter association to the edge. We have tested both fractionated and unfractionated particles, in addition to several different batches to assess the differences between the two types of ligand shell. Qualitatively, MUS:OT nanoparticles have covered the fiber edges and highlighted the underlying fibril geometry more effectively than their allMUS counterpart. This phenomenon is discussed in detail in Chapter 4, under the light shed by Chapter 1 and molecular dynamics (MD) simulations. Electrostatic interactions may be the main driving force, establishing contacts between tightly packed rows of lysine 16 on the edges of the fibers and the negatively charged nanoparticles (zeta potential between -35 and -45 mV). However, the role of the hydrophobic ligands and the adsorption onto the edges of α-synuclein fibers suggest a different mechanism, as do the MD simulations.

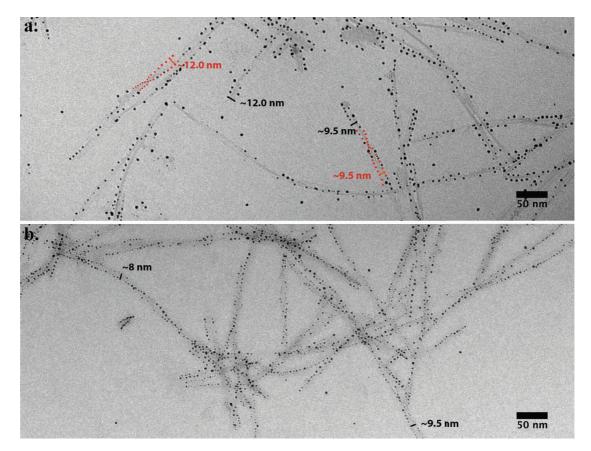


Figure 3.11 (a) Cryo-EM of  $A\beta_{1.40}$  fibers with fractionated allMUS NPs (Figure 3.9(e)). Generally, allMUS nanoparticles did not cover the fibers as densely as MUS:OT for these fibers. The distances from two pairs of particles sitting seemingly on the edges of the fibers are indicated on the figure. Red dots were drawn recapture the mode of binding seen in the next image, for MUS:OT particles. (b) Same fiber sample with MUS:OT NPs (30% OT), fractionated nanoparticles (Figure 3.10(d)) added to the sample. The fiber coverage is denser, and edge-binding is noticeable for certain fibers. The same concentrations were used in both experiments. Cryo-EM images an FEI Tecnai<sup>TM</sup> Spirit BioTWIN.

Figure 3.11 reveals that sulfonated nanoparticles adsorb onto the fibers. Unlike the cooperative and indiscriminate adsorption of cationic NPs, the allMUS NPs in Figure 3.11(a) are evenly distributed across different fibers, which agrees with an electrostatically driven interaction: nanoparticles find equally suitable counter-charges in different fibers. Close inspection of Figure 3.11(b) indicates that hydrophobicity, conferred to the nanoparticles by the OT ligands, induces a mode of nanoparticle-fiber adsorption never reported before. Yoshiike et al. reported dry images that resemble how cationic nanoparticles adsorb onto  $\alpha$ -synuclein fibers in Figure 3.4(a); but cryo-EM (Figure 3.4(c) and (d)) reveals a completely different morphology. Therefore, the way his nanoparticles bind to the fibers in solution is not known: the drying process can template the nanoparticles on the edges of the fibers, as discussed for allTMA particles on  $\alpha$ -synuclein fibers. Despite the utility of negatively stained dry TEM, the comparison between Figures 3.4(a) and (d) demonstrates that the dry state does not necessarily reflect how the species exist in the solvated state. For these reasons, the edge-binding on the

twisted ribbon morphology shown in Figure 3.11(b) is a novel supra-molecular assembly between two unrelated, yet similar materials. The cross-edge MUS:OT interparticle distances shown in Figure 3.11(b) fall in the 9 nm range. In the allMUS sample, it is difficult to find conspicuous cross-edge particle pairs to measure such distances (Figure 3.11(a)). So far, these values are not statistically rigorous, but to a first approximation, when similar fibers are compared, the interparticle distances for MUS:OT nanoparticles are about 1 nm lower than allMUS. Red dots were added to Figure 3.11(a) to illustrate how MUS:OT nanoparticles would adsorb onto the fibers, and the reported values correspond to the width of the fibers measured in ImageJ. The red dots were placed tangent to the limit of the electron-density that can be attributed to the fiber. However, the MUS:OT nanoparticles do not simply rest tangent to the edge, but appear convoluted with it: these particles form a tight interface with the edges of the fibers.

We added these two batches of particles, unfractionated (Figures 3.9(b) and 3.10(b)), to a preparation of  $\alpha$ -synuclein fibers: they both adsorbed onto the edges of twisted ribbons identically. Moreover, Figure 3.12 shows that  $\alpha$ -synuclein fibers exclude larger particles from a row of nanoparticles that delineates the edges of the fibers. The typical interparticle distance between a pair that sits on opposite edges is about 15 nm, which reflects the width of the fiber core.

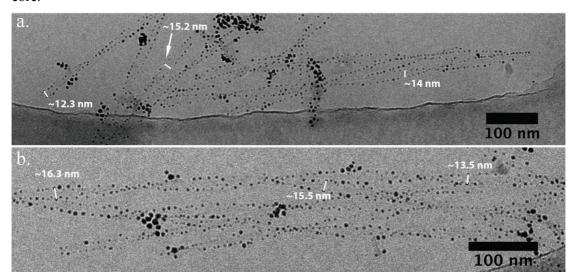
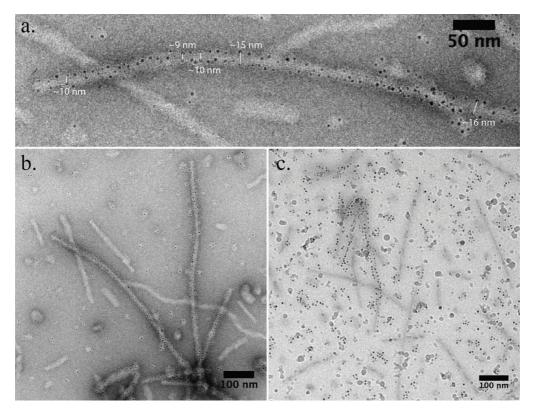


Figure 3.12 (a) Cryo-EM of α-synuclein fibers in the presence of allMUS unfractionated nanoparticles. Unlike  $A\beta_{1.40}$  fibers, allMUS adsorb efficiently onto the edges of these twisted ribbons, highlighting the helical pitch. There is a cutoff size of nanoparticles that cannot join the row of particles that follow the edge of the fibers (~4.5 nm). (b) Unfractionated MUS:OT (30% OT) nanoparticles behave no differently from allMUS when the fibers are made of α-synuclein, at least from the cryo-EM perspective. The same edge-on adsorption is observable, and the interparticle distances across the edges is similar between the two samples. Perhaps the two nanoparticles behave differently with α-synuclein fibers under other measurements. Cryo-EM images an FEI Tecnai<sup>TM</sup> Spirit BioTWIN. This imaged will be revisited in chapter 4.

Out of the 140 amino acids in  $\alpha$ -synuclein, the core of the fiber is commonly attributed to a central stretch of about 35 residues called the NAC region (non-amyloid β component)<sup>30</sup>. Different reports have shown the involvement of segments that span from position 35 to 98 in the formation of the fiber<sup>59,71</sup>, as described in chapter 1. A conservative estimate predicts two disordered tails: (i) an amphipathic 34 residue N-terminal that includes both negatively and positively charged moieties; and (ii) a C-terminal made of about 40 residues with a balance of 15 anionic groups, i.e., the number of basic residues subtracted from the acidic ones. The overall zwitterionic N-terminal and negatively charged C-terminal form disordered tails that surround the spine of the fiber. Figure 3.1(e) shows how immunogold, designed to recognize epitopes on these segments, produces a cloud of randomly distributed nanoparticles around, but not on the fiber. In Figure 3.12, the nanoparticles adsorbed onto the rigid core of the amyloid fiber, as highlighted by the interparticle distances across the edges. Because  $\alpha$ synuclein has a longer fiber-forming domain than  $A\beta_{1-40}$ , the measured interparticle distances are correspondingly larger; about 10 nm in Figure 3.11 and ~14 nm in Figure 3.12 (crude averages from manual measurements in ImageJ). The disordered side-segments may sieve the nanoparticles by size, which excludes larger ones (more detail in chapter 4) and may also help the allMUS NPs adsorb onto the edges. Nevertheless, these segments should repel negatively charged nanoparticles; instead, anionic particles adsorb more efficiently onto the edges of  $\alpha$ synuclein, which weakens a purely electrostatic interpretation of the phenomenon. The role of the C-terminal disordered segments can be tested in the future by cleaving it using enzymes.

MUS and MUS:OT nanoparticles also adsorbed onto Tau-441 fibers. The particles sat on the body of the fiber instead of interacting with the disordered side chains seen in Figure 3.1(d): in fact, immunogold labelling was used to demonstrate the existence of the fuzzy  $\cot^{76}$ . This adds to the observation made with  $\alpha$ -synuclein: these nanoparticles interact, most likely, with the cross beta sheet backbone, rather than the disordered segments that surround Tau-441 fibers<sup>77</sup>. Both allMUS and MUS:OT nanoparticles adsorbed, and depending on the fiber, the center-to-center distance between two particles on different sides of the amyloid varied from 7.4 to 16 nm (Figures 3.13 and 3.14). Again, allMUS nanoparticles did not decorate the fibers as effectively as its MUS:OT counterpart. Figure 3.13(c) shows a representative cryo-EM of the Tau-441 fiber preparation with 0.2 mg/mL fractionated allMUS nanoparticles (Figure 3.9(e)). Most particles formed aggregates of two to five particles, which likely underlines a connection with oligomeric forms of Tau protein.



**Figure 3.13 (a)** Negatively stained TEM image of Tau-441 fiber with allMUS nanoparticles. Tau fibers have long disordered segments that surround the fiber and are called fuzzy coats, to which the immunogold probes attach in Figure 3.1(d). The particles attach to the core of the fiber, as shown by the distances between nanoparticle-pairs in opposite sides of the fiber. Most are distanced by 10 nm. **(b)** A broader view of the same sample (image (a) is a crop of this one). Most fibers are not coated by the allMUS particles, instead, they seem to associate with oligomers. **(c)** Cryo-EM image of the same sample: most fibers are not covered by nanoparticles, which is to be compared to Figure 3.13(c). Image (b) ((a) is a crop of it) was acquired in an FEI TALOS<sup>TM</sup> Electron Microscope, and (c) in an FEI Tecnai<sup>TM</sup> Spirit BioTWIN.

Figure 3.14 shows that the same concentration of fractionated MUS:OT nanoparticles (0.2 mg/mL) decorated the bodies of the Tau fibers more effectively. Although other types of aggregates could be seen in the sample, this experiment reveals that MUS:OT nanoparticles have a higher affinity to the underlying interface of the amyloid fiber than its allMUS counterpart. Negatively stained dry TEM showed fibers with two rows of particles on each side: the distance between pairs of particles separated by the fiber varied between 7.4 to 12 nm. Figure 3.14(a) depicts some of these pairs and their distances measured in ImageJ. We compared the value found in dry images with the equivalent particle-particle distances found under cryo-EM, and in this case, the results were similar. In cryo-EM images (Figures 3.14(b)-(d)), the cross-edge interparticle distances varied from 9 to 17.6 nm. The small differences between dry samples and solvated ones may stem from a drying effect, or different types of fibers measured. The latter is true, because various types of fibers with different widths were

observed in the cryo-EM images. Unlike the well-defined edge-binding revealed by Figure 3.11(c) for  $A\beta_{1-40}$  and in Figure 3.12 with  $\alpha$ -synuclein, MUS:OT nanoparticles cover the body of Tau-441 fibers without following a conspicuous geometric feature. Tau protein is 10 times larger than  $A\beta_{1-40}$ , and contains cysteines that could bind nanoparticles via Au-S bonds even if they are committed to disulfide bridges. The fiber core is probably formed by a complex association of the amyloid-forming rigid core segment of the protein that adopts a superpleated serpentine-like monomeric form. Chapter 1 briefly described the structure of Tau-441 fibers, but reliable 3D models are not available. Nonetheless, when compared to the distribution of immunogold labels that target the fuzzy coat (Figure 3.1(d)), the results shown in Figures 3.13 and 3.14, demonstrate that MUS:OT, and to a lesser extent, allMUS nanoparticles interact with the core of the amyloid fibers. The disordered side chains may play a role, which can be verified by further experimentation, such as digesting away the fuzzy coat<sup>77</sup>. Nonetheless, this class of particles forms a favorable interface with the basic units of the amyloid fiber, possibly the solvent exposed cross-beta sheets.

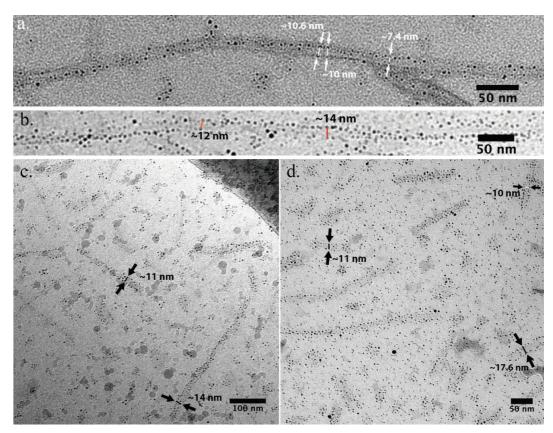


Figure 3.14 (a) Negatively stained TEM of a Tau-441 fiber covered by the same particles from Figure 3.10(d). When different particles form pairs separated by the body of the fiber, we've highlighted their distances, measuring the center-to-center interparticle separation. In this fiber, most values are around 10 nm, however a lot of "defects" prevents a long-range order claim (b) A crop from a cryo-EM image of a long Tau-441 fiber covered by unfractionated MUS:OT nanoparticles (~30%)

OT), showing similar cross-edge distances between pairs of particles. (c) Cryo-EM of MUS:OT NPs shown in Figure 3.10(d). These particles decorate the fibers more effectively than allMUS. (d) A 1 mg/mL solution of MUS:OT nanoparticles that showed complete fiber coverage and numerous non-fibrillar aggregates. The particle used in this image is an unfractionated batch of MUS:OT (~30% OT). Image (a) was acquired in an FEI TALOS<sup>TM</sup> Electron Microscope, and the others an FEI Tecnai<sup>TM</sup> Spirit BioTWIN.

### 3.6 Conclusions

This chapter has shown how different types of water-soluble nanoparticles interact with amyloid fibers. It starts from a dialogue with the preceding literature that relied on electrostatic interactions to demonstrate the existence of dense regions of positive charges on the surface of  $A\beta_{1-40}$  fibers. Such surface features agree with 3D detailed structural models of  $A\beta_{1-40}$  fiber, because the in register cross beta sheet motif can create a line of lysine 16 that points to the outside of the U-shaped monomer. Whether these facets are solvent exposed depends on the configurational polymorphism adopted by the protofibrils. It is unlikely that lysine 28 is exposed to the solvent and can form these cationic surface structures, because in all models reviewed, this residue is committed to salt bridges that stabilize the structure of the monomer. Of course, future work plans on using mutated sequences to test the role of these charged residues.

Our results show that positively charged nanoparticles, coated with quaternary amine headgroups can also adsorb onto  $A\beta_{1-40}$  fibers. We can interpret this result following Yoshiike's rationale<sup>185</sup>, to conclude that cationic particle adsorption demonstrates the existence of dense anionic features on the surface of the fiber. This interpretation does not contradict the structural models described in chapter 1, because the cross beta motif can group acidic residues into rows of solvent exposed anionic surface features on  $A\beta_{1-40}$  fibers. For example, the glutamic acid at position 22 can form a row of negative charges, which has been described to sit on the edges of a twisted ribbon morphology for  $A\beta_{1-42}$  fibers<sup>32</sup>. Nonetheless, under cryo-EM the cationic allTMA nanoparticles do not conspicuously adsorb on the edges of the fibers. The dry samples show a degree of edge-binding, which can be a consequence of the drying process: as the sample sets on the surface of the grid, the fibers template the deposition of the nanoparticles that are attracted by the edges of the fibers. In the negatively stained samples, the electron density comes from the uranium atoms of the dye (uranyl acetate) and the core of the nanoparticles: the fiber no longer exists in its solvated form. This urges the interpretation of cryo-EM images, that capture the solvated state via vitrification of the sample. Under this imaging mode, certain fibers have a high density of allTMA nanoparticle coverage, without

any signs of preferential docking. Figure 3.2(d) and (e) show that multiple parallel rows of particles completely cover the fiber. Moreover, they accumulate in certain fibers, which leaves several others free of particles. We call this behavior a cooperative adsorption, which can be influenced by the aggregation propensity of these particles in the presence of biomolecules<sup>189</sup>. The role of monomers and oligomers cannot be discarded: once in the solution, the particles can interact with the non-fibrillar species, and co-aggregate with them. The fibers offer a linear template, onto which the nanoparticles (or nanoparticle-oligomer complexes) can collectively adsorb, minimizing the excess surface energy of the system.

The cationic particles do not follow any fundamental geometric constraint of the fibers, other than its linear nature. For these reasons, we refer to allTMA nanoparticle-fiber adsorption as indiscriminate and cooperative. In other words, they do not conspicuously adsorb onto any feature of the fibers, but collectively cover individual fibers, leaving others free of any particles. A simple electrostatic explanation is unlikely to capture this phenomenon because simple charge pairing would distribute the nanoparticles across different fibers evenly. Instead, lines of particles nucleate and grow on the surface of the fibers: growth is likely mediated by the same driving forces that drive aggregation in the presence of globular proteins<sup>189</sup>. The circular dichroism (see methods) of mature fibers did not change in the presence of cationic nanoparticles, which indicates no detectable alterations in the secondary structure of the peptides. However, it is possible that the nanoparticles change the local environment, which favors the adsorption of the neighboring site, in what has been termed vicinal adsorption. Whatever the case, when sufficiently screened, these nanoparticles form aggregates and the net-negative fibers may simply provide a template onto which they can accumulate.

The same rationale can be used to explain how allTMA nanoparticles interact with  $\alpha$ -synuclein fibers. In this case, the fibers are more electronegative than  $A\beta_{1-40}^{184}$ , which leads to faster aggregation. Once covered by cationic nanoparticles, the individual  $\alpha$ -synuclein fibers interlace with one another, forming bundles (similar to ropes) of multiple fibers. This phenomenon can be the consequence of a co-precipitation phenomenon, in which, the allTMA nanoparticles screen the electrostatic forces that prevent fibers from aggregating. The mechanisms that lead the fibers to interlace escape the current discussion: simple charge screening cannot explain the level of fiber weaving observed in Figures 3.3(b) and 3.4(c). When allTMA nanoparticles were added to Tau-441 fibers, the linear aggregation was a rare

finding. Figure 3.5 shows that random aggregates predominate in the presence of Tau. The non-fibrillar proteins and oligomers probably induced the nanoparticle aggregation before they could interact with the fibers.

To test the importance of coulombic forces in the adsorption of gold nanoparticles onto amyloid fibers, a sulfobetaine terminated thiolate was synthesized. These ligands offer a zwitterionic end-group that render the nanoparticle, to a first approximation, neutrally charged. However, zeta potential measurements show a slight negative charge: two different batches of zwitterionic particles had zeta potentials of  $-2.4 \pm 0.5$  mV and  $-9.2 \pm 0.2$  mV. The latter was used in these experiments, and showed remarkable colloidal stability in the presence of all amyloid fiber preparations. A flocculation-like phenomenon was observed when all other nanoparticles were added to the fiber suspensions. In this case, even centrifugation (13,000 g for 10 min) only created a pale pellet, while the supernatant remained red. All images collected with these particles showed evenly distributed nanoparticles that did not interact with the amyloid fibers. The charge-neutrality is probably not responsible for this behavior: an additional experiment using PEGylated neutral nanoparticle needs to be done to confirm this claim. Previous studies indicate that zwitterionic surfaces form strong hydration shells that prevent non-specific protein adsorption 115,190,188,187,114. These types of head-groups form an electrostatically mediated water shell that is more cohesive than its hydrogen-bonded counterpart found in ethylene glycol coatings<sup>187</sup>. The disruption of this water shell is energetically unfavorable, which manifests as a force opposing the contact with a protein. We hypothesize that the same phenomenon causes the colloidal stability of our zwitterionic nanoparticles in the presence of amyloid fibers and their non-fibrillar species. This hypothesis is difficult to challenge experimentally, because we lack the means to demonstrate this proposed water shell and then verifiably disrupt it.

When we studied how negatively charged nanoparticles interact with the fibers, the reductionist coulombic approach did not provide a straightforward interpretation of our observations. We prepared two types of negatively charged gold nanoparticles. The first, protected by a phosphate group, precipitated in the presence of  $A\beta_{1-40}$  fibers, and has not been tested yet with other proteins. The second was the sulfonate-based particles discussed in chapter 2: these particles revealed that electrostatics alone cannot explain all binding phenomena. Using the same concentration, particles protected only by the MUS ligand did not adsorb onto  $A\beta_{1-40}$  and

Tau-441 fibers as efficiently as its MUS:OT counterpart. The two particles only showed the same behavior when added to the anionic α-synuclein fibers, which, again, goes against a purely electrostatic explanation. Amyloid fibers of full-length peptides often have disordered side chains, which in the case of Tau protein form large fuzzy coats<sup>76</sup> that have been described as charged polymer brushes (Figure 1.13) <sup>77</sup>. Our results indicate that MUS-based nanoparticles adsorb onto the spine of the amyloid fiber, and not diffusely around the disordered segments, as in Figure 3.1(d). The brushes might contribute to nanoparticle adsorption, but do not constitute the final interface between nanoparticles and amyloid fibers. Instead, allMUS and MUS:OT nanoparticles adsorb onto the rigid fiber core, that is made of a cross beta sheet motif. Cryo-EM reveals that small MUS:OT nanoparticles discriminate the edges of fibers that adopt a twisted ribbon morphology in 3D. The edges of twisted-ribbon fibers made of  $A\beta_{1-40}$  or  $\alpha$ synuclein were effectively decorated by these particles. Only electrostatics cannot explain these observations, because of the importance of ligand-shell hydrophobicity brought about by 1octanethiol ligands in the adsorption onto  $A\beta_{1-40}$  fibers. Our results neither confirm nor contradict the image shown in Figure 3.1(a). Instead, it reveals that the interaction between nanoparticles and amyloid fibers depends on the properties of the nanoparticle ligand shell and on the amyloid fiber.

Chapter 4 shows that a phenomenon similar to the lipid bilayer fusogenic behavior described in chapter 2 may drive this discriminative adsorption. Experiments show that the amphiphilic nanoparticles described in the previous chapter bind to the edges of the twisted ribbon amyloid fibers and follow their underlying geometric constraints. Molecular dynamics calculations predict favorable contacts between the ligand-shell of these nanoparticles and parts of the beta-sheet of the protofibrils or the elbow of the U-shaped monomer.

# 4 Discriminative adsorption of amphiphilic gold nanoparticles onto amyloid fibers

#### 4.1 Introduction

Chapter 3 covered how water soluble gold nanoparticles interact with amyloid fibers. It systematically provided experimental evidence that electrostatics alone cannot explain how nanoparticles behave with these protein assemblies. Instead, several parameters, including coulombic interactions, hydrophobic forces and the organization of water molecules in the ligand shell dictate how this nano-bio interface<sup>109</sup> occurs. This offered insight for the design of immunogold labels to prevent non-specific interactions; apart from zwitterionic nanoparticles, all other ligand shells investigated showed some degree of interaction or aggregation in the presence of amyloid fibers and the corresponding non-fibrillar species. It also introduced an unanticipated phenomenon: sulfonated nanoparticles adsorbed preferentially onto the edges of amyloid fibers with a twisted ribbon morphology. The helicity of these ribbons was highlighted by the presence of the sulfonated particles in the case of  $A\beta_{1-40}$  and  $\alpha$ -synuclein fibers imaged under cryo-EM. Moreover, it showed that the presence of 1-octanethiol in the ligand shell improves the decoration of amyloid fibers made of  $A\beta_{1-40}$  and Tau-441.

This chapter tackles the discriminative adsorption of MUS:OT and allMUS nanoparticles onto amyloid fibers. This class of nanoparticles does not adsorb onto all the interfaces generated by the amyloid fold. Instead, they dock on the edges of fibers that adopt a twisted ribbon morphology, in a process we call discriminative adsorption. The total free energy of the system is minimized when the nanoparticles attach to a particular structure on the surface of the fibers. For example, small MUS:OT nanoparticles arranged into either two or three intertwining lines of particles, that agree with two basic polymorphs described in chapter 1<sup>28,31</sup>. Unlike cationic nanoparticles, that completely cover the fibers, sulfonated particles follow the geometry of these supra-molecular assemblies: this is only possible if the nanoparticles interact with an underlying ordered surface feature. This chapter shows a set of different experimental conditions that either favors or eliminates this behavior.

Both size and ligand-shell composition affect the ability of these nanoparticles to adsorb onto the edges of the fibers. The larger (4-6 nm) allMUS and MUS:OT nanoparticles, synthesized using the modified Stucky method, did not adsorb onto the edges of the fibers as conspicuously as one phase prepared NPs. Furthermore, in polydisperse samples, the smaller nanoparticles

adsorbed more efficiently onto these features; this agrees with atomistic molecular dynamics (MD) simulation that showed favorable binding for smaller particles. Following the model used by van Lehn et al.  $^{135}$  a set of three nanoparticles was built: 2 nm allMUS, 2 nm MUS:OT (30% OT) and 5 nm MUS:OT (30% OT). These particles were in placed in the vicinity of model protofilaments of  $A\beta_{1-40}$  and  $A\beta_{1-42}$ : the 2 nm particles spontaneously adsorbed onto the protofilaments in the simulation timescale, whereas 5 nm particles had to overcome a 3.5 kcal/mol energy barrier to bind to the  $A\beta_{1-42}$  model.

The insights gained from these calculations and experiments enable the proposal of verisimilar binding geometries. It is impossible to unambiguously establish the binding sites at a molecular scale relying solely on microscopy and calculations; nonetheless, this system satisfies the requirements to determine ligand-peptide contacts using nuclear magnetic resonance<sup>38</sup>, which opens opportunities for future experiments. The impact of this discovery is two-fold: first it sheds light on the rapidly growing interest to use gold nanoparticles for protein structure determination<sup>94,173</sup>. Here we describe an antibody-free method to mark discrete structures on a protein assembly. Second, given the current search for substances that recognize and bind to amyloid fibers<sup>177</sup>, in addition to the drugs already in phase 3 clinical trials that target the mature amyloid<sup>191,192</sup> the description of a class of materials that recognizes discrete surface features can become a useful tool in amyloid research.

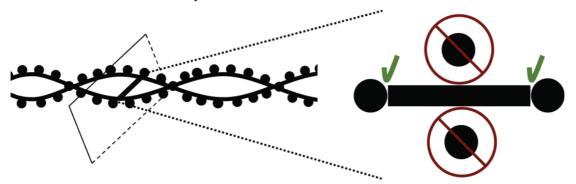


Figure 4.1 Schematic of the problem: why do MUS and MUS:OT nanoparticles bind to the edges of amyloid fibers and not on the longer facets? Here the fiber is oversimplified as a flat twisted ribbon, with a rectangular cross section. How the constituent monomers assemble to form the core depicted by the rectangle can be proposed using the detailed molecular structures described in chapter 1. Such models differ from the results proposed by high-resolution cryo-EM reconstructions  $^{80}$ , which render this assignment challenging. Regardless of what the particles adsorb to, the results match the current disagreements in the literature. Disordered segments are omitted, but likely play role, especially in the case of α-synuclein and Tau protein. Experiments show that the particles probably sit on the rigid backbone of the fibers. Not drawn to scale.

## 4.2 Cryo-EM results with $A\beta_{1-40}$ : binding and non-binding conditions

The results are shown sequentially, to illustrate the experimental conditions that produced images with edge-binding and what parameters erased the phenomenon. All experiments with

A $\beta_{1-40}$  were done by preparing a monomeric solution of the peptide at ~10  $\mu$ M, unless otherwise noted. The fibers were allowed to grow in 96-well plates, or inside Eppendorf tubes in a thermomixer at agitations that ranged from 300 to 1000rpm at 37°C for 12 h: the condition is specified in the caption of each figure. Growth was monitored by ThT fluorescence and negatively stained dry TEM imaging. We have also performed fiber growth in the presence of the different types of nanoparticles in a plate reader to assess their effect on fiber formation kinetics. Examples of the kinetic curves are shown in the Methods section (Figures M.16 and M.18). Under regular TEM and cryo-EM, the fiber-NPs species from co-growth or post-addition showed little differences: the NP ligand shell and diameter has determined the decoration of fibers by the nanoparticles. Preliminary data indicates that the type of nanoparticle can change the length of the fibers, and under AFM imaging, their thickness. Here we focus on the cryo-EM results that allow us to visualize the metallic core of the nanoparticles, and the silhouette of the fibers. Figure 4.1 shows an experiment in which 10  $\mu$ L of 1 mg/mL unfractionated allMUS nanoparticles was added to 90  $\mu$ L of the mature amyloid fiber solution: the mixture was agitated for 12 h under 1000 rpm at 37°C.

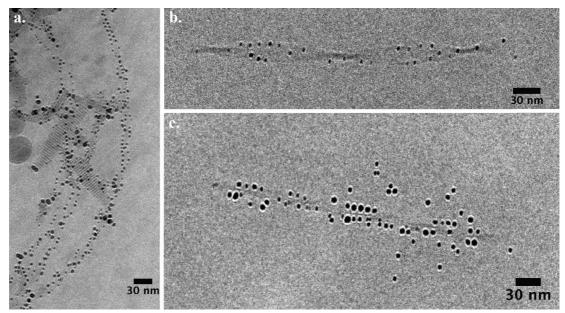


Figure 4.2 Unfractionated allMUS nanoparticles added to mature  $A\beta_{1.40}$  fibers. (a) This image is somewhat an exception: it shows the allMUS particles  $(2.42 \pm 1.77 \text{ nm})$  binding to the edges of this type of fiber. With  $A\beta_{1.40}$  this has not been the rule. This image also shows that larger particles are excluded from the row of NPs that cover the edges of the fibers. Striated structures have been observed in allMUS unfractionated samples, and we do not know their nature. (b) and (c) Typical finding on  $A\beta_{1.40}$  fibers with unfractionated allMUS nanoparticles. Images acquired in an FEI Tecnai<sup>TM</sup> Spirit BioTWIN.

When fractionated allMUS ( $2.65 \pm 0.92$  nm) nanoparticles were used, the overall observations did not change. The fiber preparation followed the same protocol, and the only significant difference may stem from a higher effective concentration of nanoparticles in the fractionated

experiment. In other words, unfractionated particles contain a higher amount of larger NPs, that are heavier. The particle stock solution is prepared gravimetrically, that is, a 1 mg/mL solution is prepared based on the mass of the nanoparticle powder, which can cause a higher effective nanoparticle concentration for fractionated samples. Figure 4.3 shows typical images of sparsely covered fibers. The TEM characterization of the NPs used in these two experiments can be found in Figures M.13 and M.14.

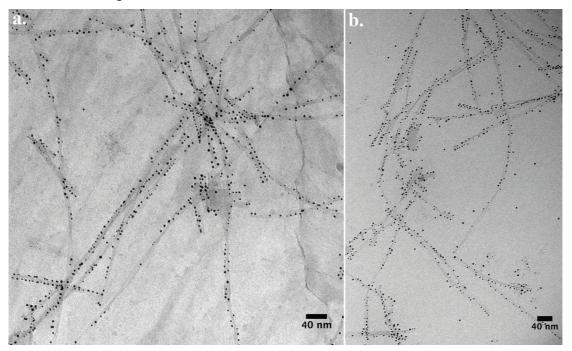


Figure 4.3 Fractionated allMUS nanoparticles, added to  $A\beta_{1-40}$  fibers. (a) Some edge-coverage was observed in this sample and seen in fibers in the center of the image or lower left. (b) The typical aspect shows fiber binding, but no decoration that highlights underlying geometric fiber properties. Images acquired in an FEI Tecnai<sup>TM</sup> Spirit BioTWIN.

MUS:OT (30% OT) unfractionated nanoparticles ( $\sim$ 1-4 nm) were added to the same type of A $\beta_{1-40}$  fiber preparation. Overall, the macroscopic behavior of the sample was similar to allMUS: the solution was homogeneous during agitation, and upon storage at 4°C, or even room temperature, a red solid precipitated to the bottom of the vial. This effect was absent only in two types of nanoparticles: ZW NPs and MUS:OT NPs with 10% OT composition. Figure 4.4 shows clear edge-adsorption of these MUS:OT NPs that displayed a typical center-to-center interparticle distance across the fiber of 11 nm, at the widest part of the ribbon. The distance between neighboring NPs on the same chain oscillate between  $\sim$ 5-6 nm, to 12 nm, as illustrated in Figure 4.4(b).

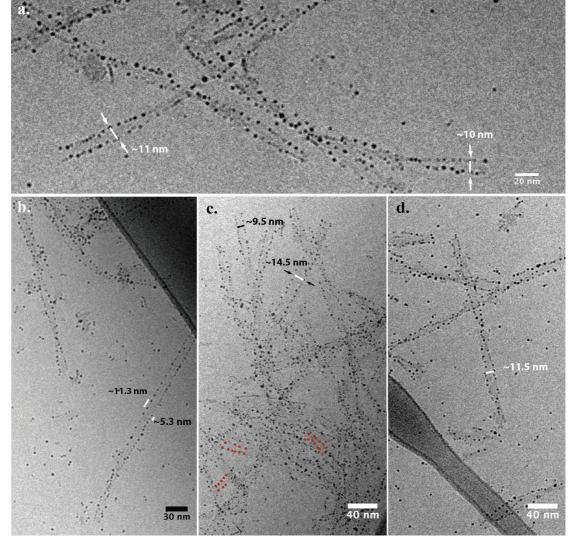


Figure 4.4 Different views of  $Aβ_{1-40}$  fibers with MUS:OT (30% OT) nanoparticles adsorbed on their edges. (a) This image shows two measurements of the center-to-center distances between nanoparticles that sit on different sides of the twisted ribbon. The fibers can be wider than the values reported here, but these sizes were the most commonly observed. (b) Different helical pitches are often reported for amyloid fibers, and used to categorize them. This image shows a fiber that does not "twist" and two distances between neighboring nanoparticles on the edges. (c) A common finding in regions with a high density of fibers: when they aggregate, it can be difficult to distinguish single fibers, but the particle binding is still observable. Red dots were placed on top of nanoparticles that sit on candidate single fibers that are difficult to distinguish. (d) On the bottom of this image, three lines of particles can be seen around one fiber, which may be indicative of a 3-fold symmetric  $Aβ_{1-40}$  polymorphism. Image acquired in a JEOL 2200FS by Dr. Davide Demurtas.

The images shown in Figure 4.4 have been reproduced in several different experiments, as will be shown in the next section. We have searched for experimental conditions to prevent this type of edge-adsorption onto  $A\beta_{1-40}$  fibers from happening. The experimental parameters that prevented the particles from adsorbing effectively were: (i) decreased time of incubation, (ii) presence of 1% fetal bovine serum and (iii) nanoparticles synthesized using the Stucky method. This last item is still under investigation: from the definition given here to discriminative

adsorption, the MUS:OT (33% OT) Stucky nanoparticles may be adsorb onto the same sites as their smaller counterparts. The "discriminative" qualifier used to describe the mode of adsorption is morphological and qualitative: when nanoparticles clearly delineate the twisted ribbon morphology, it receives this qualifier. Nonetheless, the nanoparticles shown in Figure 4.5(d) may have adsorbed onto the same sites as their smaller counterparts, but in these conditions do not form long chains of on the edges of the fibers. Figure 4.5 summarizes the findings under these conditions.

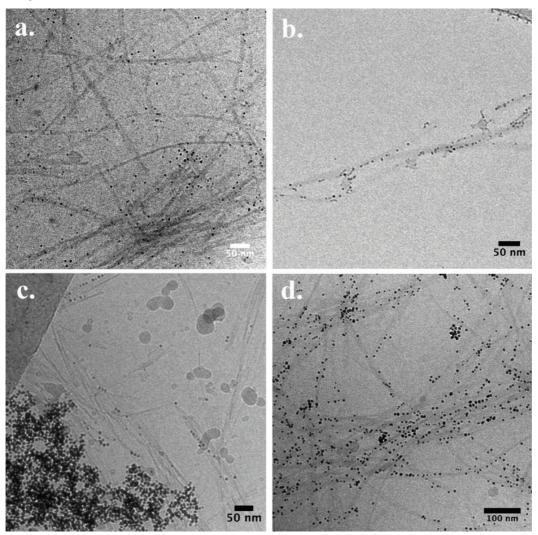


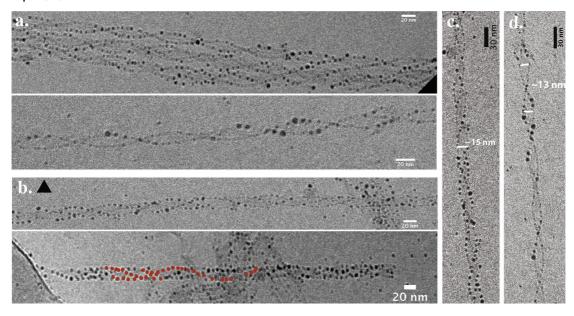
Figure 4.5 Experimental conditions that have prevented discriminative adsorption of MUS:OT NPs onto  $Aβ_{1-40}$  fibers. (a) Presence of 1% FBS: caused nanoparticle aggregation. (b) Shorter incubation time: sample shaken for 2h at 37°C. All other experiments had 5 to 12 h incubation periods. Some binding is seen, but not comparable to Figure 4.4. (c) allMUS Stucky nanoparticles (4.82  $\pm$  1.83 nm). Particle aggregation was observed and only a few nanoparticles landed on the fibers. (d) Stucky MUS:OT (33% OT) nanoparticles (5.0  $\pm$  1.0 nm). The addition of OT to the nanoparticles increased their adsorption onto the fibers. All images acquired in an FEI Tecnai<sup>TM</sup> Spirit BioTWIN.

Figure 4.5(c) and (d) reveal that nanoparticle diameter and more importantly, the ligand shell composition determine the adsorptive behavior of MUS-based nanoparticles on  $A\beta_{1-40}$  fibers.

This finding remounts to Figure 1.25(b), that showed the importance of nanoparticle diameter in their propensity to fuse with lipid bilayers. Larger nanoparticles have lower ligand mobility, which may prevent them from interacting with the available amyloid surfaces. The MD calculations showed this behavior, in addition to the larger electrostatic repulsions between allMUS and 5 nm MUS:OT 7:3 NPs, that can disfavor the formation of particle chains on the edges of the fibers. The proteins present in FBS can eliminate the adsorption via different mechanisms. For example, the nanoparticles can interact with serum proteins, forming a protein corona that prevents the ligand shell from contacting other surfaces. Alternatively, serum proteins may competitively bind to the fibers, preventing nanoparticles from adsorbing onto them: a combination of these two effects is possible. Recently, the dissociation constant between albumin and MUS-based nanoparticles has been experimentally calculated, and corresponds to a binding energy around -70 kcal/mol (unpublished data). If the MD calculations are correct, the binding energies between these nanoparticles and the amyloid fibers range from -23.04 to -65.16 kcal/mol: therefore, in the presence of albumin, the nanoparticles may favorably bind to the abundant globular proteins. If the particles are not covering the fibers because they first interact with serum proteins, an increase in the amount of NPs that surpasses the globular protein binding sites, can generate NPs free to interact with the fibers. An analogous experiment has been performed with Tau-441, but the competition is between non-fibrillar material and fibers of the same protein. It is difficult to envision an experiment with these techniques to address the possibility that the fibers are covered by serum proteins thus preventing NP adsorption. Figure 4.5(b) points towards an endergonic adsorption: the samples need agitation at 37°C to yield covered fibers.

The adsorption of nanoparticles onto the edges of the fibers has been observed across different sample preparations: the phenomenon has been reproducible apart from the conditions shown in Figure 4.5. How the monomers arrange in space to constitute the amyloid fiber is difficult to establish, as reviewed in chapter 1. Nonetheless, during our experiments, we have observed two conspicuous morphologies: two and three fold symmetric twisted objects. Figure 4.6(a) and (d) show 2-fold symmetric fibers with two intertwining chains of nanoparticles that correspond to the helicity of a twisting ribbon. The 3-fold symmetric fibers were less abundant in our sample preparations, but Figure 4.6(b) and (c) show three intertwining chains of nanoparticles: care must be exercised because the intertwining lines are 2D projections of NPs on a 3D twisted triangular prism. For a ribbon it suffices to measure the largest dimension to obtain its width. For the three-fold symmetric fiber, the three 'sinusoidal' lines (see red dots in

Figure 4.6(b)) trace how the nanoparticles arrange in 3D along a twisted pyramidal prism: vertices and faces are symetrically equivalent in the 2D projection. In this case, the longest center-to-center distance between a pair of particles on opposite sides (~15 nm) can correspond to the distance between particles sitting on the faces or the vertices of this twisting prism. The three-fold symmetric model for  $A\beta_{1-40}$  predicts a ~7 nm facet for such prism<sup>28</sup>; if the center of a particle is 3 nm from the surface it interacts with (gold core radius plus ligand shell), simple geometric considerations would make the center to center distances fall in the 9 nm rage for vertex interactions, and ~7 nm for face-on interactions. These calculations and approximations need to be made with great care: Figure 4.15 depicts an approach to this problem, but this section simply introduces the finding of two symmetries in the same sample. To our knowledge, the 3-fold morphology has only been shown under cryo-EM once, with dimensions that did not match the ssNMR models<sup>79</sup>. Our sample was prepared at 37°C under 1000 rpm, which according to the literature<sup>28,47</sup>, favors the two-fold symmetric species. Three fold symmetric fibers were usually described in quiescent preparations<sup>31</sup> and also in brain-derived  $A\beta_{1-40}$ <sup>33</sup>.



**Figure 4.6** In the same sample, with  $Aβ_{1-40}$  fibers and MUS:OT (10% OT) nanoparticles, the two polymorphs commonly described in the literature were easily detectable. (a) A bundle of twisted ribbon fibers and a single one on the bottom. Careful inspection can help distinguish between three-fold symmetric fibers from overlapping two-fold fibers. (b) Two examples of three-fold symmetric fibers that co-exist in this sample with the other polymorph. The triangle indicates the symmetry in the the axis of the fiber. Red dots were placed on top of NPs to illustrate the 'sinusoidal' pattern adopted by single chains of particles in the 2D projection plane of the image. (c) Longest width found for a center-to-center NP distances in a 3-fold symmetric fiber. (d) The same type of distance on the same image on (a). Images acquired in an FEI Tecnai<sup>TM</sup> Spirit BioTWIN.

The observation that nanoparticles can highlight the underlying geometry of two different polymorphs led us to attempt a sample preparation that results in three-fold symmetric fibers.

Following Paravastu et. al. 28, 50μM of Aβ<sub>1-40</sub> monomeric solution was prepared, and allowed to fibrillate under quiescent conditions at room temperature. Fiber growth was monitored by negatively stained TEM. After one month under these conditions, the sample had abundant fibrillar material, and we faced a conundrum: agitation at 37°C is necessary to decorate the fibers, but it has been reported to cause a morphology shift from 3-fold to 2-fold symmetric fibers<sup>47</sup>. Also, the results from Figure 4.6 showed that it was possible to find 3-fold symmetric fibers in the conditions necessary for nanoparticle adsorption. Thus we added 10 μL of 1 mg/mL MUS:OT (30% OT) one phase nanoparticles to 90 µL of the fiber solution, and kept it under 300 rpm at 37°C overnight. The sample showed nanoparticle adsorption, as depicted in Figure 4.7(a), but did not resemble Figure 4.6(b): no fibers with three chains of particles could be detected, but most fibers had a single line of particles running through one side. The sample was then returned to the thermomixer and agitated at 1000 rpm and 37°C for 48h: many monodecorated fibers (i.e. only one side) remained, but wide, conspicuous twisted-ribbon two-fold symmetric fibers had nanoparticles on both edges (Figure 4.7(b)) in additions to a few 3-fold symmetric fibers (bottom panel of Figure 4.7(b)). Although these are microscopy findings, that risk being statistically unrepresentative, thorough imaging revealed a clear difference between the samples before and after the 48h agitation.

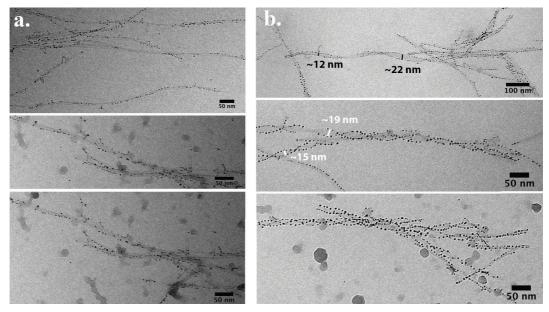


**Figure 4.7 (a)** Quiescently prepared  $Aβ_{1-40}$  fibers with MUS:OT (30% OT) added, after 12h at 300 rpm and 37°C. Most fibers had particles only on one side, and several short strings of particles protruded from the main fiber. This can be indicative of secondary nucleation. **(b)** Same sample after 48h under 1000 rpm at 37°C eliminated, for the most part, the string-like protrusions and generated edge-decorated twisted ribbon fibers. The fibers were considerably wider than the ones reported in previous figures and seen in other experiments starting with 10 μM monomer concentration. The bottom panel shows a possible three-fold symmetric fiber. The experiment aimed favoring three-fold symmetric fibers, but instead showed a complex fibernanoparticle interaction, and possible secondary nuclei in the quiescent preparation. Images acquired in an FEI Tecnai<sup>TM</sup> Spirit BioTWIN.

# 4.3 Nanoparticle adsorption onto α-synuclein is size dependent

One phase synthesized allMUS and MUS:OT NPs adsorbed equally onto  $\alpha$ -synuclein fibers. This experiment revealed another phenomenon: an apparent size selectivity of the adsorption on the edges of these fibers. A more comprehensive analysis of this data is on-going, but initial results suggest that the polydispersity index PDI (or simply dispersity,  $\Theta$ ) of nanoparticles adsorbed onto  $A\beta_{1-40}$  fibers is higher than of those adsorbed on  $\alpha$ -synuclein fibers. PDI can be defined in different ways, for example as the ratio between weight and number average molecular weights for polymers; but in colloidal science, the ratio between standard deviation and mean size is a common assessment of size distribution<sup>110</sup>. From analyzing two sets of images, one for  $A\beta_{1-40}$ , shown in Figure 4.6, and the set of images that contains Figure 4.7(b), the PDI of the NPs on the edges of  $A\beta_{1-40}$  fibers is approximately 0.53 and for  $\alpha$ -synuclein 0.44. A more comprehensive image analysis will refine these preliminary values, but inspection of an image such as Figure 4.6(a) shows that  $A\beta_{1-40}$  fibers accommodate different sizes of particles. On the hand, larger ( $\sim$ 5 nm) nanoparticles are excluded from the edges of  $\alpha$ -synuclein fibers (Figure 4.9), and size mismatches seem to cause defects on the linear NP superlattices that form on the edges (see arrows in bottom part of Figure 4.9(b)).

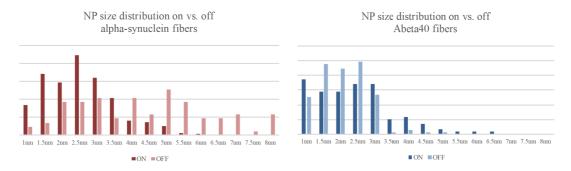
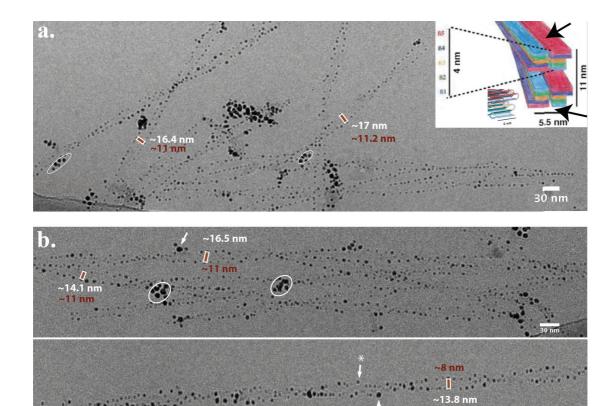


Figure 4.8 Size distribution of nanoparticles on the edges of the fibers and distributed across the sample.  $\alpha$ -synuclein fibers seem to "select" small nanoparticles that can dock on its edges. As seen in Figure 4.6, there is no significant difference between the diameters of the nanoparticles adsorbed onto  $A\beta_{1-40}$  fibers and those in the rest of the image. These measurements require more data points to quantitatively reveal a size-dependent phenomenon. So far, the comparison between Stucky and one phase NPs suffices to demonstrate the role of nanoparticle diameter on fiber adsorption.



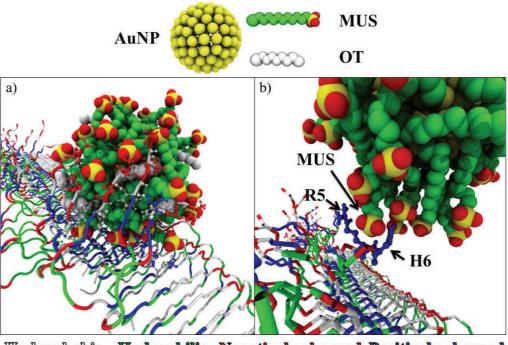
**Figure 4.9** α-synuclein fibers with a twisted ribbon morphology were equally decorated both by **(a)** unfractionated allMUS nanoparticles and **(b)** unfractionated MUS:OT (30% OT) nanoparticles. The size distribution on the surface of these fibers is slightly lower than those on  $Aβ_{1.40}$  fibers. Larger particles seem to disrupt the chain of particles on the edge of the fibers as indicated by arrows with asterisks. Excluded larger NPs are shown with white circles. The typical center-to-center distances between NPs on different sides, on the widest portion of the ribbon, are indicated in the images. The white rectangle shows the nanoparticle distance and the inner red rectangle the approximated distance between the nanoparticles surfaces, as estimated in these images: the defocus does not allow for a precise assignment, and an error between 0.5 to 1 nm must be considered. On the other hand, the center-to-center distances are reliable: the nanoparticles serve as a cryo-EM contrast imaging agent. The inset in figure 1 comes from reference (69) and was explained in Figure 1.12 in chapter 1. Their model places the solvent-exposed beta sheets on the edges of the twisted ribbons, and our nanoparticles are spaced by about 11 nm (surface-to-surface): if our sample corresponds to their model, the NPs are probably interacting with the cross-beta motif and not with disordered tails or surface loops. Images acquired in an FEI Tecnai<sup>TM</sup> Spirit BioTWIN.

The size distributions of particles on the edge of each type of fiber, and on the overall sample is shown in Figure 4.9. More image analysis is needed to ensure the reliability of this analysis, but the plots agree with image inspection. Figure 4.8 shows the particle size distribution in the  $\alpha$ -synuclein image in which a size cutoff occurs between 3 and 4 nm, while A $\beta_{1-40}$  fibers accommodate a greater variety of sizes. These results agree with the molecular dynamics simulations that predicted a greater binding energy for 2 nm allMUS and MUS:OT (7:3) NPs in comparison to 5 nm MUS:OT (7:3) NPs: thus, it is expected to find a bigger amount of smaller nanoparticles on the edges of the fibers.

## 4.4 Insights from molecular dynamics simulations

In collaboration with Dr. Francesco Tavanti and Prof. Alfredo Alexander Katz, the interaction between monolayer-protected AuNPs with A $\beta_{1-40}$  and A $\beta_{1-42}$  proto-filaments was simulated. AuNPs with core diameters of 2 nm and 5 nm were built according to the previous work of Van Lehn et al. <sup>135</sup>. The monolayer composition and the core diameter were designed to create three types of NPs: 2 nm allMUS, 2 nm MUS:OT 7:3 and 5 nm MUS:OT 7:3. The A $\beta_{1-40}$  proto-filament comes from the ssNMR work of Petkova et al. <sup>78</sup> and the A $\beta_{1-42}$  from the H/D exchange experiments by Lührs et al. <sup>32</sup>. The system is placed in a cubic box with the height of the proto-fibril, which is equivalent to constructing a continuous proto-filament.

AuNPs bound spontaneously to  $A\beta_{1-40}$  and to  $A\beta_{1-42}$  during the simulations. The 2nm and the 5nm AuNPs interact with the beta-1 region of  $A\beta_{1-40}$  making stable contacts with the amino acids from histidine 12 to phenylalanine 20. In simulations with 2 nm NP with a ligand-shell composition of MUS:OT 7:3, the amino-acids in the  $A\beta_{1-40}$  tail interact with the AuNP after binding. Up to 4 disordered tails grab the AuNP especially through alanine 2 and phenylalanine 4 due to hydrophobic interactions: in the same region, two positively charged amino acids, asparagine 1 and 7, could make electrostatic interactions with the negatively charged MUS ligands, but they remain far form the sulfonate groups. When 2 nm allMUS NPs are used, an  $A\beta_{1-40}$  disordered tail seems to mediate the interaction with the NP driving the binding to the beta-1 region. The first interaction happens through a contact between an MUS ligand with arginine 5 and histidine 6 as shown in Figure 4.10(b). Then the NP is close enough to the protofilament to interact with the beta-1 region and form a stable contact with that facet. The binding site found here, spanning from histidine 14 to phenylalanine 20 ( $^{14}$ HQKLVFFA $^{21}$ ) is compatible with the predicted binding site ( $^{16}$ KLVFFA $^{21}$ ) of drugs and peptides described in the literature  $^{193,194}$ .



Hydrophobic Hydrophilic Negatively charged Positively charged

Figure 4.10 On top, the representation of the AuNP and of its ligands. (a) a snapshot of the simulation of the 2 nm MUS:OT 7:3 NP, bound to the beta-1 region of the A $\beta_{1-40}$  proto-filament, interacting with 5 disordered tails. (b) Arginine 5 and histidine 6 grab a sulfonate group in the early steps of binding with allMUS NPs. Amino acids are colored according to the legend at the bottom of the figure.

To better understand how these nanoparticles interact in the vicinity of a similar cross beta sheet structure, a simulation using the  $A\beta_{1-42}$  proto-filament was also performed. All 2 nm NPs interacted directly with the elbow of the folded monomers ( $^{27}$ NKGAI $^{31}$ ), that links the two beta strands. First the NP interacts with hydrophilic residues near the C-terminal of the beta-1 strand. After 20ns, the NP moves toward the region with hydrophobic amino acids closer to the N-terminal region of the beta-2 strand. Figure 4.11 shows this mode of approach, observed in both types of 2 nm NPs that we denominated 'side binding', which is equivalent to contacting the loops described in chapter 1. This configuration is characterized by ligand shell interaction with glycine, alanine and isoleucine, illustrated in Figure 4.11: the nanoparticle remains stable for more than 100ns suggesting that this is a possible stable binding site for small MUS-based gold nanoparticles.

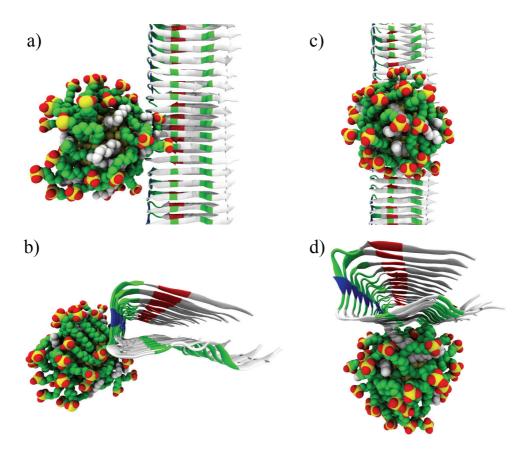


Figure 4.11 (a) and (b) show different views on the side-binding motif, in which the nanoparticle finds an energy minimum via interaction with the elbow of the monomers. (c) and (d) show different views of the stable interaction the NPs establish with the beta-2 segment.

The other binding site is located on the beta-2 segment (<sup>31</sup>IIGLMVGGVVI<sup>41</sup>), shown in Figure 4.11(c) and (d), a region characterized by a sequence of hydrophobic amino acids. The nanoparticle interacts with the N-terminal portion of the beta-2 strand, and after 10 ns moves along the beta sheet region. By establishing contacts with the hydrophobic side groups of isoleucine 31, glycine 33, methionine 35, glycine 37, valine 39 and isoleucine 41 the NPs remained bound on this beta sheet for more than 100 ns. On the other hand, the 5 nm diameter NP is never bound to the proto-filament over the 100 ns simulations suggesting the existence of an energy barrier.

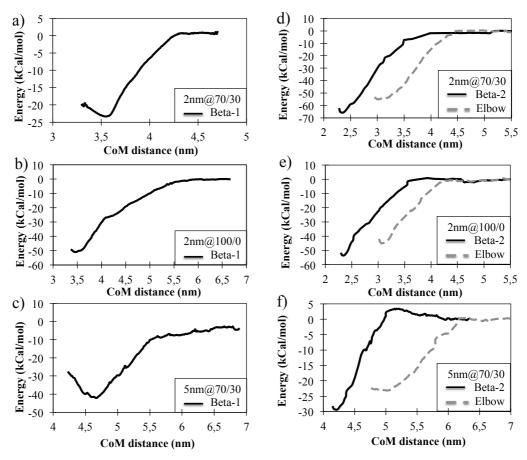


Figure 4.12 (a), (b) and (c) show the free energy of binding for the three types of nanoparticles approaching the beta-1 strand of an  $A\beta_{1-40}$  proto-filament. The energy gain is highest for 2 nm allMUS and 5 nm MUS:OT 7:3 NPs, which contradicts our comparative nanoparticles studies. (d), (e) and (f) show the different binding energy profiles for the nanoparticles to interact with the elbow (dashed curves) and the beta-2 segment (solid line). These results agree with our experimental findings, because they show a higher gain in free energy of binding for 2 nm MUS:OT 7:3 NPs.

## 4.5 Possible binding motifs

Analysis of the images obtained for the three types of amyloid fibers studied in this thesis shows remarkable similarities in the center-to-center nanoparticle distances between two different edges on the amyloid fibers. The 'extreme' type of disordered segment-containing fiber is made of Tau-441, followed by  $\alpha$ -synuclein and then  $A\beta_{1-40}$ . The case of Tau presented in Figure 1.14(d) shows that, if the nanoparticles adsorbed on the disordered segments, their center-to-center distances would oscillate in a cloud of particles distanced from ~23 nm to 50 nm on the opposite sides of the fiber. Instead, Figures 3.13 and 3.14 show that the center-to-center nanoparticle distances coincide with the dimensions measured for the Pronase-digested Tau-441 fiber (~11 to 16 nm). This means that our amphiphilic nanoparticles traversed the fuzzy coat to adsorb onto the rigid core of the PHFs. The same is true for  $\alpha$ -synuclein, and the center-to-center nanoparticle distances match the length scale of the amyloid fibril core (Figure

4.9). Figure 4.13 shows schematic differences between the disordered 'tails' that protrude from these different types of amyloid fibers, and the consistent center-to-center distances between NPs on opposite sides of the fibers. The disordered segments may play a role, for example, in the size-selection of NPs adsorbed onto  $\alpha$ -synuclein. Experiments that use smaller peptides are on-going, but we chose to show the effect on relevant full-length polypeptides to demonstrate that the adsorptive phenomenon occurs at the rigid backbone of the fiber. The MD dynamics simulation revealed a degree of interaction between the ligand shell and the N-terminal of A $\beta_1$ -40, so the disordered tails may contribute to the adsorptive behavior, but the nanoparticle's final interaction is determined by the rigid backbone.

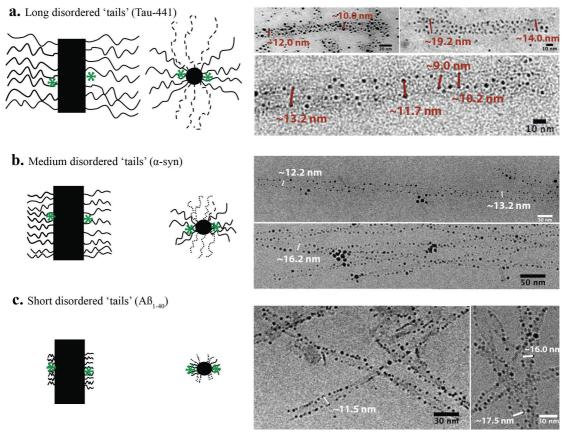


Figure 4.13 Comparison of the center-to-center distances between MUS:OT NPs on opposite sides of three different amyloid fibers. Green asterisks indicate proposed site of adsorption. (a) A schematic rendition, reminiscent of Figure 1.13, showing that fibers made of Tau-441 protein have long disordered tails that protrude radially outwards. As reviewed in chapter 1, the 'tails' form the fuzzy coat that surrounds the fiber core, analogous to a polyelectrolyte brush. Nonetheless, the distances measured fall in the ~12 nm regime: comparison to immunogold labelled fuzzy coats in Figure 1.13(d) shows MUS:OT NPs interact with the core of the fiber. (b) A depiction of α-synuclein with 'intermediate' disordered segment length: in this case, as reviewed in chapter 1, the long C-terminal is negatively charged, which should repel the MUS:OT NPs. Again, the particles seem to establish an interface with the core of the fiber. (c) In the case of  $Aβ_{1-40}$ , most models (except those derived by cryo-EM  $^{195}$ ) predict a disordered N-terminal between 9 to 17 residues long: we assume in this image that such segments are sufficiently shorter than their equivalents in α-synuclein and Tau-441. Left-hand panel in (c) was acquired by Dr. Davide Demurtas in a JEOL 2200FS, the others in an FEI Tecnai<sup>TM</sup> Spirit BioTWIN. The lower panel in (a) is a negatively stained TEM acquired in an FEI TALOS<sup>TM</sup> Electron Microscope.

The molecular dynamics simulations show that the nanoparticles bind favorably to the beta-1 strand of an  $A\beta_{1-40}$  monomer. However, the energy minima found in the simulations do not correlate with the comparisons found between the different nanoparticles experimentally. We have shown that one phase MUS:OT NPs (30 or 10% OT) adsorb discriminatively onto the edges of amyloid fibers with a twisted ribbon morphology. Moreover, we have observed binding to three-fold symmetric fibers, that, according to the detailed molecular structural models, expose the beta-1 strands to the solvent, while the beta-2 segments face inwards, establishing hydrophobic contacts via methionine 35. The model proposed by Lührs et. al. for  $A\beta_{1-42}$  predicts beta-1 or beta-2 segments as the interfaces of the edges in a twisted ribbon morphology model. If this is accurate for the fibers studied in this project, a nanoparticle-beta-2 contact on the edges of the twisted ribbon morphology could reconcile both the simulations and the experimental observations.

During this thesis work, there was no technique to unambiguously characterize the arrangement of the proto-filaments that compose the fibers, and except for NMR the options seem limited. Given the observations made in the images and the insight from the MD calculations, the nanoparticles bind preferentially either to the beta-1 stretch or the elbow of the U-shaped monomers. Both structures are necessarily tied to the geometry of the fiber, and self-correlate in space via a screw symmetry, although flat fibers are often observed. What sits on the edges, that interacts with allMUS and MUS:OT nanoparticles cannot be unambiguously determined with the current approaches. A hypothesis was already given for  $\alpha$ -synuclein fibers, in Figure 4.9, based on the geometric constraints of the model by Vilar et. al.<sup>69</sup>. The same can be done for A $\beta_{1-40}$ , but as reviewed in the first chapter, there are too many possibilities: whichever way our nanoparticles adsorb onto the fibers, they do so in absolute agreement with the current disagreements in this field.

Figure 4.14(a) shows a fiber splitting longitudinally into two thinner fibers, half the width of the original one (or equivalently, two thin fibers that coalesce into a wider one). The nanoparticles occupy all available edges, that can be formed either by the elbows of the monomers or by solvent-exposed beta sheet segments. The inset in Figure 4.14(a) shows a cross section of a fiber, proposed by ssNMR, in which four U-shaped monomers stack to create a cross-section of 6 by 8 nm: the smallest 6 nm dimension corresponds to solvent exposed beta-sheets (beta-1) <sup>28</sup>. Figures 4.14(b) and (c) show two different possible arrangements that could

explain the longitudinal fissure in the fiber, that in turn generates fresh interfaces onto which the NPs adsorbed. The interpretation offered in Figure 4.14(b) matches both the MD calculations and the dimensions measured in the cryo-EM image. Such measurements need to be done carefully because slight beam misalignments or depending on the relative position of the focal plane and the sample, distortions can occur. However, the nanoparticles offer conspicuous guiding points for cryo-EM images, and center-to-center measurements can be done at the resolution of the technique. The main question becomes the distance between the center of the NPs and the underlying surface. In Figure 4.14(a), the distance between the surfaces of two NPs was measured in ImageJ (red), and gave a value ~8 nm, whereas the center-to-center distance was 12.6 nm. If the rationale in Figure 4.14(b) is correct, the distance between the center of a NP and the underlying fiber surface is approximately 2.3 nm: this value varies with nanoparticle diameter and possible heterogeneities in the tightness of the adsorption across different NPs.

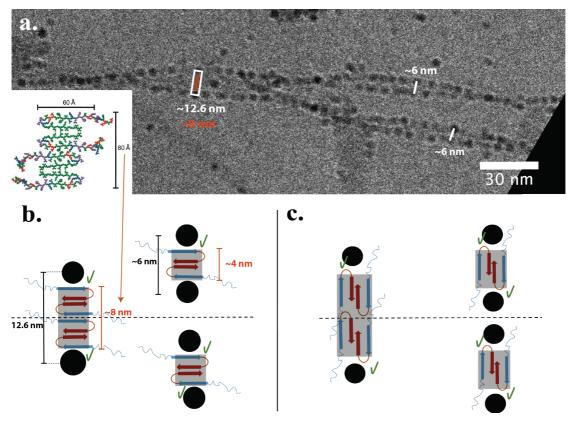
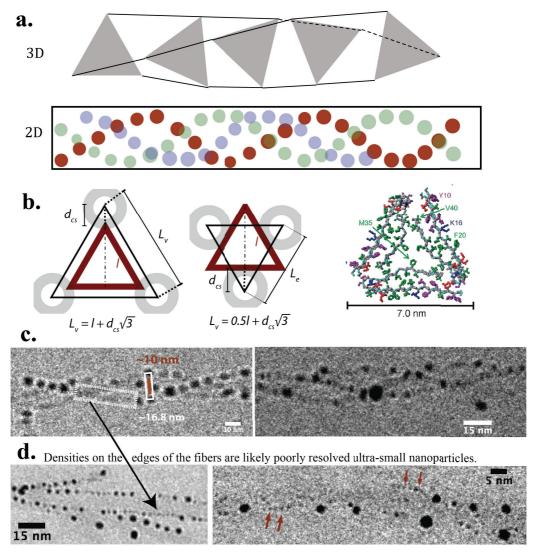


Figure 4.14 (a)  $A\beta_{1.40}$  fiber that from left to right, split into two fibers, or, from right to left, coalesce into one. Although we've shown that the adsorption process takes time (agitation at 37°C), this fiber, that "splits into" two smaller twisted ribbons, has its edges immediately covered by the nanoparticles. The nanoparticles act as surfactants that minimize the excess surface free energy of the unfavorable interfaces created by the rigid edges. Another possibility is that the disordered tails disfavor adsorption in the regions they occupy, because the nanoparticle would reduce the conformational entropy accessible to the disordered tails, by reducing the free volume. Images acquired in an FEI Tecnai<sup>TM</sup> Spirit BioTWIN.

Following the approximations offered in Figure 4.14, we turn to the the 3-fold symmetric fibers. As discussed in the presentation of such polymorphs in Figure 4.6, this type of morphology can be approximated to a twisted triangular prism; the 2D projection of the nanoparticles that sit on the surfaces of such prism produce three intertwining chains of NPs, as illustrated in Figure 4.15(a).



**Figure 4.15** The 3-fold symmetric polymorph. (a) A simplistic representation of a triangular prism in 3D and the 2D projection of beads that sit on its surface, to clarify the observation in the cryo-EM images. (b) Two proposed binding motifs: on the vertices (elbows and beta sheet-disordered segment interfaces) or on the faces of the triangular cross-section. The expressions given of  $L_v$  correspond to the center-to-center NP distances on a triangular cross section of side length 1. The detailed structural model proposed from reference (28). (c) Shows two crops of cryo-EM images of candidate 3-fold symmetric fibers. The longest measured center-to-center NP distances was ~16.8 nm, whereas the face-to-face inner NP distance was ~10 nm. (d) Images of fibers with ultra-small NPs in focus. The set of images that contains the 3-fold symmetric fibers is not in focus with the plane of the NPs. The electron-density observed in the edges, where no nanoparticles seem evident, may be caused by nanoparticles with ~1nm diameters. The image on the left shows a high resolution of the same batch of NPs on a different fiber preparation, whereas the image on the right shows a synthesis designed to produce a population of sub-nanometer NPs, and the red arrows point to their presence on the edges of the fibers. The electron densities on the edges in (c) are likely caused by these small NPs. Images acquired in an FEI Tecnai<sup>TM</sup> Spirit BioTWIN.

Currently, how the nanoparticles sit on the triangular prism established by the core of the fiber is largely inconclusive. In the 2D plane of the cryo-EM images, the maximum center-to-center NP distances is equal to  $L_{\nu}$ , the distance between two nanoparticles on the cross-section of the triangular prism. This value depends on the values of  $d_{cs}$ , the distance between the center of the NPs and the subjacent surface, and on the size l of the triangular cross-section, which is determined by the  $A\beta_{1-40}$  monomer. From inspection, it is clear that vertex-binding generates larger interparticle distances in the 2D projection than the face-on motif. Furthermore, there are no tools to verify that the 7 nm value proposed for this polymorph corresponds to our sample or is even a realistic value in the solvated state; also the monomers can arrange in this symmetry, but with segmental or even configuration polymorphisms that expand the triangular cross section. If we assume l = 7 nm and  $d_{cs} = 3$  nm, the vertex and face-on configurations would give values of 12.2 and 8.7 nm respectively: neither match our measurements, but the former is closer. If we assume an l of 10 nm, these values rise to 15.2 and 10.2 nm. This suggests that our measurements agree better with an expanded version of the fiber-NP object in a vertex-on association. More detailed analysis of this data may clarify this issue, but it must be stressed that a rigid commitment to the 7 nm dimension may be unrealistic in the solvated state: an estimation of the effective size will be performed to clarify this issue.

For  $\alpha$ -synuclein fibers, we have concluded that the NPs sit on the solvent exposed beta sheets on the edges. The same was proposed for twisted-ribbon  $A\beta_{1-40}$  fibers; however, (for now) the 3-fold symmetric species suggests a nanoparticle adsorption that does not involve docking onto the solvent exposed beta-sheets. In this case, the interaction with loops and the interface between beta-sheets and disordered segments would be the site of adsorption, which agrees with the MD simulations that found favorable interaction between the NPs and the loops of the  $A\beta_{1-42}$  monomers (Figure 4.11(a) and (b)). The models available in the literature range from slightly different, as shown for the detailed structural models in chapter 1, to simply incompatible, as depicted in Figure 1.14(a) and (b) from the work of the group of Prof. Grigorieff<sup>79,195</sup>. If our samples corresponded to his models, the nanoparticles would interact with edges made of partially disordered N-terminals. However, how can this be reconciled with the systematic observation of edge-binding on fibers made of  $\alpha$ -synuclein? These contradictions are currently beyond the possibilities of our experiments, but these nanoparticles can become a great aid in the structural determination of amyloid fibers. Moreover, the

determination of a realistic cross-sectional size for the 3-fold symmetric fiber can strengthen the beta-sheet adsorption motif.

Perhaps the nanoparticles do not bind to a particular solvent-exposed conformation of betasheets or elbows, but rather to a combination of both features at their interface, which could explain the observation made with the 3-fold symmetric fibers. Although an unambiguous conclusion cannot be reached, the evidence for beta-sheet binding compels the assertion that this is the driving force behind the discriminative adsorption of MUS-based NPs onto these fibers. The agreement between our cryo-EM images and the model for  $\alpha$ -synuclein proposed by Vilar et. al.<sup>69</sup>, in addition to the results from the MD simulations that predicted favorable NP interaction with the beta-1 faces of  $A\beta_{1-40}$  protofilaments support the possibility that these NPs adsorb preferentially onto solvent exposed beta sheets. The only evidence from our own experimental work against this hypothesis came from the 3-fold symmetric fibers, but the calculations may be incorrect, or the solvated size may be greater than 7 nm. Nonetheless, as reviewed exhaustively in Chapter 1, there are enough disagreements in the literature of structural models for amyloid fibers, in addition to the possibility that the monomers adopted different conformations throughout our experiments, the calculations made in Figure 4.15 alone do not disqualify the hypothesis, but rather make us reluctant to reach an overarching definitive conclusion. Whatever the case, our NPs have consistently agreed with the current disagreements in the field.

## 4.6 Competitive binding and $A\beta_{1-42}$ secondary nuclei

Figure 4.5(a) showed that the presence of FBS prevented the discriminative adsorption of MUS-based gold nanoparticles on the edges of amyloid fibers. The phenomenon could be due to a competitive adsorption, in which the nanoparticles are first consumed by globular proteins: in case the number of particles increases, they would be free to adsorb onto the fibers. A similar experiment has been performed, by adding different types and amounts of MUS and MUS:OT nanoparticles onto a Tau-441 preparation. Figure 4.16(a) and (b) show different regions of a sample that contained 0.1 mg/mL of fractionated allMUS NPs. The fibers were rarely decorated by nanoparticles, but non-fibrillar species were covered by three or more particles throughout the sample. Tau contains cysteines which man mediate the interaction with gold particles via Au-S bonds. When MUS:OT (30% OT) particles were used, also at 1 mg/mL the oligomers and some fibers were covered (Figure 4.16(c)). If the nanoparticle concentration is increased ten-fold the fibers are completely covered along with several other aggregates. The non-

fibrillar species are more favorable adsorption sites for the nanoparticles: as these sites are filled, the supernumerary particles can then occupy other sites, namely those exposed by the surface of the fiber.

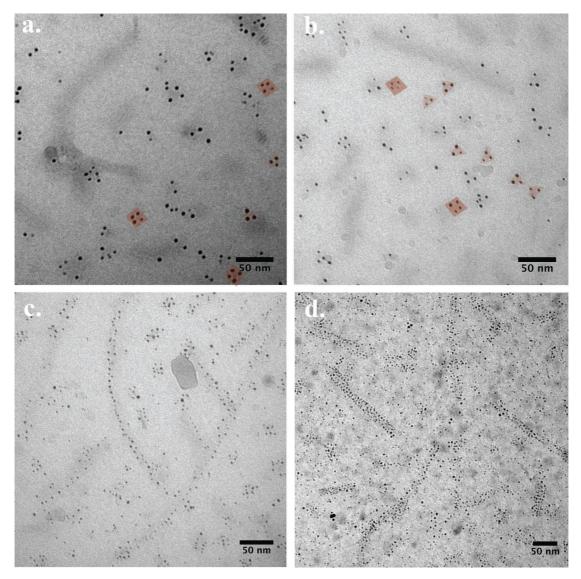


**Figure 4.16** Cryo-EM of samples that with changes in the amount and type of nanoparticles in the same Tau-441 preparation. (a) and (b) show images of the same sample, with 0.1 mg/mL allMUS NPs. Decorated fibers were rare, the silhouettes of thick fibers can be see, free of particles. Trimers and tetramers of NPs were abundant in the sample and highlighted in red. (c) When MUS:OT (30% OT) NPs were used, the fibers started being covered, but small aggregates were visible throughout the sample. (d) When the final NP solution (MUS:OT 30%OT) was 1 mg/mL, the fibers were completely covered, along with several types of smaller aggregates. Images acquired in an FEI Tecnai<sup>TM</sup> Spirit BioTWIN.

A similar phenomenon has been consistently observed whenever the experiments presented in this thesis were attempted with  $A\beta_{1-42}$ . Small nanoparticle chains that protrude from the body of the fibers were observed in all occasions when we worked with  $A\beta_{1-42}$  and in one occasion

with  $A\beta_{1-40}$ : when the fibers were allowed to grow quiescently, at room temperature from a 50 $\mu$ M monomeric solution. Instead of covering the fibers as was observed for all three peptides studied, the nanoparticles covered structures reminiscent of the recently described secondary nuclei on the surface of  $A\beta_{1-42}^{153,161}$ .

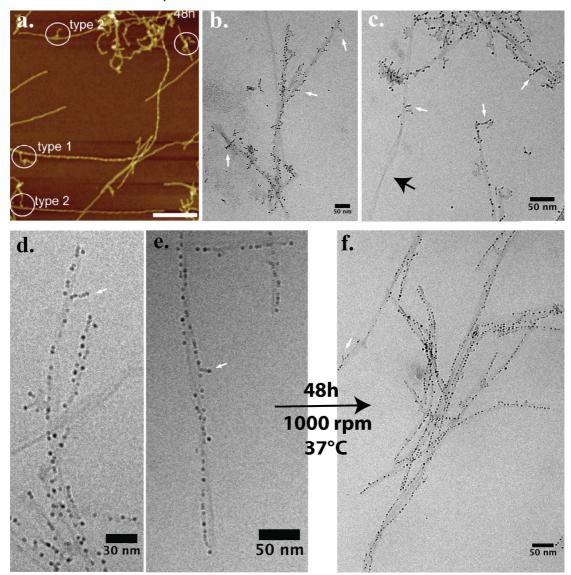


Figure 4.17 (a) Reproduced from reference (184) an AFM image showing secondary nuclei protruding from the surfaces of  $A\beta_{1-42}$  fibers. (b) and (c) show similar protruding strings of nanoparticles, that can correspond to secondary nuclei. The black arrow indicated a twisted ribbon fiber that otherwise is coated by MUS:OT nanoparticles on the edges. (d) and (e) show similar such strings on an  $A\beta_{1-40}$  preparation that used 50  $\mu$ M monomeric solution under quiescent conditions. Several small such protrusions were identifiable throughout the sample, but not as conspicuously as in the  $A\beta_{1-42}$  experiments. (f) Shows that after agitating the same sample over a 48 h period at 1000 rpm at 37 °C, the aspect of the fibers changed, and discriminative adsorption could be observed, without as many protruding strings.

These two experiments may correlate to the findings with FBS: MUS-based nanoparticles adsorb first to oligomeric species to which it has higher affinity. This is not a mere tautological claim: MUS-based nanoparticles may be acting as colloidal surfactants, and first adsorb onto

objects with high surface tension. The secondary nucleation that protrude from the  $A\beta_{1-42}$  fibers have been correlated with toxicity, and so are oligomeric species of proteins such as Tau<sup>15,166</sup>. Furthermore, it has been hypothesized that early nuclei have structures that deviate form the cross-beta sheet motif, which makes their surface more unstable<sup>24,53</sup>: this correlates to the traditional description of nucleation and growth. Nuclei have to pay high surface tension penalty, and only growth can placate the Gibbs free energy of the material, with the favorable bulk free energy thus overcoming the unfavorable surface tension. One way to stabilize small nuclei, such as the nanoparticles used in this thesis, is with surfactants, capable of decreasing the excess surface tension to stabilize these objects. Figure 4.16 and 4.17 reveal that the MUSbased NPs act, to a first approximation, as surfactants that first bind to high surface energy nuclei, oligomers and secondary nuclei, to then occupy the sites to which they have remarkable affinity on the surface of the amyloid fibers. This finding may be helpful to study and visualize secondary nucleation in experiments that search for substances that aim to eliminate this process. Evidently such scenario urges careful controls: for example, the nanoparticles could interact with the candidate substance that can block secondary nucleation, which could hamper the utility of the NPs in this context. Finally, to our knowledge, secondary nucleation of Aβ<sub>1</sub>- $_{40}$  has not been reported: the images in Figure 4.17(d) and (e) may reveal that  $A\beta_{1-40}$  fibers are also capable of nucleating secondary nuclei on their surfaces, but significantly less than  $A\beta_1$ . 42.

## 4.7 Conclusion

Although the behavior of the nanoparticle that gave this thesis its name has been studied in greater depth, it might be the last finding that holds potential applications for these new materials. The discriminative adsorption itself might be able to reconcile two fields that have been producing disparate structural molecular models for amyloid fibers: the spectroscopic community<sup>23,24</sup> and the cryo-EM structures proposed for Aβ fibers<sup>80</sup>. The nanoparticles presented in this thesis, that in Chapter 2 were shown to fuse with lipid bilayers, may serve as a cross-instrumental probe, whereby they facilitate cryo-EM structural assignments and also reveal ligand-shell peptide interactions in dully isotopically labelled samples for NMR studies: the nanoparticles can add a constraint to the system to disambiguate, for example, the nature of the edges of the fibers. We have briefly shown the presence of ultra-small nanoparticles in Figure 4.15(d): this corresponds recent progresses in the attempt to produce atomically precise MUS-based nanoparticles, that would greatly increase the quality of a structural determination

effort that joins spectroscopy and electron microscopy. Finally, these nanoparticles seem to act as spherical surfactants that cover early unstable nuclei and oligomers (Figures 4.16 and 4.17). This can become a tool for amyloid researchers to study, not only mature amyloid fibers, but also oligomers under controlled conditions. More importantly, this thesis shows a novel phenomenon: regardless the utility, it presents a new scientific fact at the interface of two complex nascent fields. This work has systematically approached how the chemical properties of the ligand-shell dictates the amyloid-nanoparticle interface, and showed a remarkable level of supramomecular structure through the self-assembly of ordered proteins-nanoparticle objects without the use of peptides or other linkers to create such structures: this alone is a novel accomplishment in the field of supramolecular chemistry that merits profound investigation and the determination of the nature of the discriminative adsorptive behavior.

## 5 Outlook and future work

The results presented in this thesis belong to a larger project that can provide a novel tool in the study of amyloids and proteins in general. This work was exploratory and phenomenological in nature, and it offers a good starting point for other researchers to design experiments to probe the interaction between amyloids, proteins and metallic nanoparticles. It has also systematically shown the role of charged end groups at the bionano interface with amyloids: for example, to avoid non-specific adsorption (thus false positives), this thesis provides enough evidence that zwitterionic surfaces are ideal coverage for the colloidal gold used in immunogold labelling. We have also seen that small MUS:OT nanoparticles allowed us to easily distinguish two and three-fold symmetric  $A\beta_{1-40}$  fibers. This has introduced a potential tool to study dynamic amyloid phenomena, for example, to verify the presence of secondary nuclei, onto which the nanoparticles adsorbed preferentially when Aβ<sub>1-42</sub> fibers were used. Furthermore, the advances in electron microscopy, for example, the possibility of imaging in liquid 196, open the possibility of studying how amyloid fibers behave in real time in 3D. In this case, the nanoparticles described in this thesis would act simultaneously as immunogold staining and an analogue of dyes such as thioflavin T. The use of the gold-thiol bond to perform further modifications on the nanoparticles, such as the introduction of antibody fragments or any other chemical modification can be easily exploited to take advantage of the non-specific phenomena described in this work.

## 5.1 Determination of MUS:OT adsorption site onto the amyloid fibers

This thesis has raised, through experiments, a fundamental question that was tackled in chapter 4: what is the feature on the edges of the amyloid fibers onto which small sulfonated amphiphilic gold nanoparticles adsorb? How come these nanoparticles do not also sit on the other facet of the twisted ribbon amyloid fibers? Unfortunately, a detailed review of the literature did not allow us to conclude, unambiguously, what type of supramolecular structure the nanoparticles bind to. As outlined in chapter 1, different motifs have been ascribed to the edges of the ribbons, such as solvent exposed beta sheets, or the loops that connect different beta sheet segments in the polypeptide sequence. The amyloid samples used in this work were not prepared and characterized completely, to allow for an unambiguous 3D model on which one could ascribe a specific sequence or structure to the edge of facet of the ribbons. Nonetheless, these types of particles may help determine the nature of the edges, and add an additional constraint on the experimental sets ups used to simulate the 3D structure of amyloid fibers using data from NMR and electron microscopy. One 'brute force' approach to solve this

question is to synthesize isotopically labelled (<sup>13</sup>C) MUS or OT ligands and amyloid fibers (<sup>13</sup>C and <sup>15</sup>N) and perform the NMR and cryo-EM experiments. According to our simulations, the fiber-nanoparticle interaction satisfied the requirements for this experiment to succeed: the ligand-peptide contacts are below 8 Å and there are about 1.5 ligand per peptide chain, as depicted in Figure 5.1. This means that this laborious and potentially costly experiment is, so far, justifiable both from the experimental results and the insights from the molecular dynamics simulations.

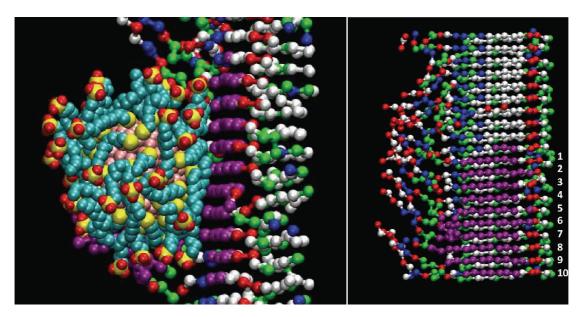


Figure 5.1 Snapshots from the simulation between MUS:OT nanoparticles and  $A\beta_{1.40}$  protofilaments. According to the simulations, the ligand shell that establishes contact with the solvent exposed beta sheets (beta-1 segment) compresses the ligand to maximize ligand-peptide contacts. This means that there are several ligand-peptide contacts that fall below the 8 Å threshold for good NMR signal. The side view on the right shows in purple, the stretches of the peptide that, in the MD calculations, established this type of contact with the ligands on the nanoparticles. Given appropriately isotopically labelled samples, one can envision an experiment that visualizes the nanoparticles on the edges of the twisted ribbons, and establishes, via NMR, the ligand-peptide contacts, thus determining which residues are exposed on the edges and what conformation the nanoparticles seem to discriminatively adsorb to: solvent exposed beta sheets or other less rigid structures? This concept can be extended to the other fibers, such as  $\alpha$ -synuclein that so far, lacks reliable 3D models.

Other approaches can be adopted to tackle the site of adsorption, or the type of protein structure the nanoparticles preferably bind to spontaneously. Ingenuous use of less expensive NMR techniques, that escape the expertise of the author might clarify these questions. For example, instead of the non-trivial isotopic labelling of the ligand shell, one could simply include in a typical NMR-based amyloid structural determination study, a cryo-EM session in the presence of our nanoparticles. In this context, more could be said about the nature of the edges on such samples, which would strengthen the argument for a mode of adsorption. This type of experiment would not be a direct measurement of intermolecular contact, but could provide reliable and accessible information regarding this unanticipated discriminative behavior.

Indirect evidence can also be obtained by forming microcrystals as described by the Eisenberg group. In this case, the anisotropic microcrystals display beta sheet facets parallel to the long axis, and their cross section (a fractured crystal) is made of packed layers of the constituent monomers. The crystals can be prepared, and their structure verified to match those published by Eisenberg's group. The nanoparticles can be incubated in the presence of these crystals, followed by imaging such as cryo-EM, AFM, among other possibilities. If the nanoparticles form organized lattices on the lateral facets of the microcrystals, it strengthens, but does not prove, the hypothesis that in the absence of oligomers and other lower-order amyloid aggregates, the nanoparticles form ordered arrays upon adsorption onto solvent exposed beta sheets.

Ultimately, we have experimentally discovered that sub-4 nm MUS:OT nanoparticles, and allMUS as well in the case of  $\alpha$ -synuclein, adsorb discriminatively onto the edges, and only the edges of twisted ribbon amyloid fibers. The main question now is: what are the supramolecular protein structures that these nanoparticles prefer to adsorb to, in the absence of factors such as serum proteins, lower order oligomers and secondary nuclei? Whatever the mechanism, this is in itself a reproducible and falsifiable scientific fact that merits further investigation.

# 5.2 Immediate utility of MUS:OT NPs for amyloid research: dynamics and secondary nucleation

Several studies can be performed using these nanoparticles as EM markers or tags to demonstrate amyloid-related phenomena. Of immediate interest, and currently under investigation, is the use of liquid state TEM to visualize how the fibers behave in their native solvated state. The nanoparticles provide the electron density necessary to visualize the fibers, and such experimentation would be virtually impossible without these NPs. In this context, these nanoparticles act as an EM analogue to ThT. Another experiment on the line if the verification of the utility of MUS:OT nanoparticles as markers for secondary nucleation in A $\beta_{1-42}$  fibers. As shown in figure 4.17, we currently believe that the nanoparticle protrusions from fibers made of A $\beta_{1-42}$  correspond to secondary nucleation recently described in the literature 153,161. It has been hypothesized that the surface of the fiber acts as a catalyst to the formation of new, secondary fibers. In addition to the observation that the nanoparticles tend to bind first to small oligomers and these secondary nuclei, we plan to take advantage of this

behavior to use the nanoparticles to verify the absence of secondary nucleation. One strategy, currently underway, is the use of the protein chaperone BRICHOS that has been reported to block the secondary nucleation process<sup>166</sup>.

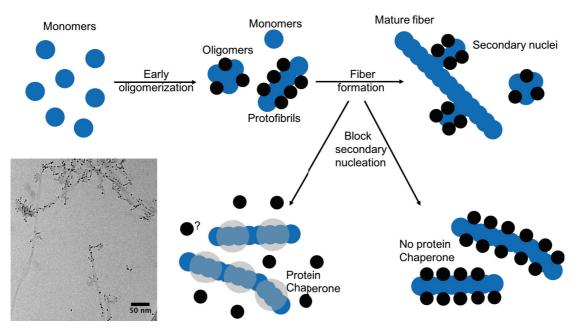


**Figure 5.2** Schematic representation of an experiment that uses the MUS:OT nanoparticles tendency to adsorb onto oligomers and secondary nuclei to test for the absence of such protrusions in the presence of a secondary nucleation blocker. Depending on the nature of the blocker, it is difficult to predict the outcome. The more favorable binding sites offered by the secondary nuclei may vanish, and the nanoparticles will assume their location on the edges of the mature fibers. Or, if the fiber is then covered by a protein chaperone, or another complex biomolecule, we expect at least to no longer observe the discrete nanoparticle protrusions from the surfaces of the fibers. Nonetheless, it is possible that in the presence of a protein-based secondary nucleation blocker such as the BRICHOS protein, that nanoparticles aggregate onto this third protein in the system and yield inconclusive results.

## 5.3 Different physical properties across distinct polymorphs

So far, attempts to establish different physical properties between polymorphs of  $A\beta_{1-40}$  has shown little difference between the two and three-fold symmetric variants<sup>47</sup>. It is possible that the choice of monomer for such experiments was such that, the difference between the polymorphs studied was not significant. Whenever working with Tau-441, and more recently Huntintin, we have noticed that some types of fibers are readily covered by the nanoparticles, whereas others are not. This effect is flagrant in image 3.13, in which certain Tau fibers are completely covered by the MUS particles, whereas other fibers that appear morphologically different, are free of particles. This can be an indication that, for larger amyloid precursors capable of forming diverse polymorphs, the surface properties of the amyloids can be probed using, for example, AFM to determine properties such as adhesion<sup>77</sup> that may depend on the polymorph. This type of experimentation should become routine in collaboration with an AFM

group capable of carrying out such measurements, because it can produce data immediately relevant to the debate of amyloid polymorphisms. The nanoparticles can act as a guide to identify one polymorph from another, in a morphologically-based classification. We anticipate this will become a persistent observation whenever large proteins are used as amyloid precursors. On a final note, we did observe coated and uncoated fibers in the quiescently prepared A $\beta_{1-40}$  samples, shown in Figure 4.17(d)-(f), but this may be a consequence of a lower particle count relative to the available amyloid surface. Nonetheless, the potential for polymorph-dependent surface property determination (adhesion, deformability, etc) cannot be ruled out for fibers made of  $A\beta$ . Such studies can be relevant to understand the pathologic role of amyloids as different surface properties, correlated to different polymorphs (or strains) can yield different interactions with cellular membranes and other biomolecules, correlating to the severity of the disease. There is already evidence that different clinical presentations in two patients correlated to different structures of the  $A\beta_{1-40}$  fibers<sup>33</sup>. This is likely a common phenomenon throughout amyloid pathogenicity and its biophysical underpinnings are amenable to good use of AFM experimentation and the use of our nanoparticles to identify different polymorphs.

## 5.4 Additional experiments: fiber modifications and mutations

Some of the observations in this thesis were not fully addressed experimentally. For example, in chapter 3, in the discussion of Figures 3.3 and 3.4 it is stated that  $\alpha$ -synuclein fibers carry many negative charges, which could explain its prompt interaction with cationic particles and the formation of nanoparticle bundles. Further experimentation is needed to use electrostatics as the sole reason behind this observation. The disordered C-terminal that carries most of the acidic residues that under neutral pH confer the fiber a negative charge can be cleaved enzymatically, and the experiment can be re-performed with the allTMA nanoparticles. If the bundling phenomenon vanishes, it is a strong indication that indeed electrostatics play the major role in forming these 'almost ropes' of  $\alpha$ -synuclein mediated by the allTMA NPs. Furthermore, a careful zeta-potential measurement can be performed to verify whether the bundling and subsequent flocculation coincides with a point-of-zero charge precipitation.

Although the adsorptive behavior has been repeated across considerably dissimilar fibers, with discriminative adsorption of small MUS:OT nanoparticles on the edges of twisted ribbon amyloid fibers, the effects of mutations on the sequence of the polypeptides on this phenomena

have not been challenged. For example, the substitution of positively charged residues such as lysine at position 16 or 28 can challenge the idea that the nanoparticles are simply attaching to favorable lines of counter-charges on the surface of the fibers. Such manipulations must be done with care, because the substitution of lysine 28 for example, can change completely the structure of the fiber, and render the wild-type and the mutant incomparable. Again, it would be best to perform this type of experiment in collaboration with an NMR group to have the full characterization of the fibers, and more confidence in the interpretation of the cryo-EM images and results. The use of mutants and truncated versions of amyloid precursors such as Tau and Huntintin are already underway, and so far, the main observation falls in the discussion proposed in section 5.3. It is difficult to anticipate how subtle mutations can influence the nanoparticle-amyloid interactions, especially after observing strikingly similar phenomena using completely different amyloid precursors such as  $A\beta_{1-40}$  and  $\alpha$ -synuclein. So far, an explanation revolving a stable adsorption onto a general feature such as solvent-exposed beta sheets is favored over specific amino acid sequence recognition.

## 5.5 Other experiments and biologically relevant studies

During this thesis, several techniques were employed to study the interaction between the different nanoparticles and the amyloid precursors and fibers. Due to the different properties of the two classes of materials studied, several difficulties arose. For example, depending on the type of nanoparticle used (MUS or MUS:OT), they had different affinities for the chips of Biacore surface plasmon resonance machines. This made experimentation challenging and results inconclusive. The attempt to separate nanoparticle-amyloid aggregates using size exclusion chromatography was unsuccessful: apparently the nanoparticles have a high affinity for the stationary media (Superdex 200) and do not move through the column. Nonetheless, progress has been made in forming NP monolayers on gold chips for Quartz Crystal Microbalance (QCM), which means we can finally study the role of the ligand shell on the affinity between amyloid precursors and the nanoparticles.

Furthermore, there has been a lack of biologically relevant studies. Initially, there was no room for such experiments because the interactions between all the nanoparticles described in this study and the amyloid fibers and their precursors are completely unknown. Now that these interactions are understood, *in vitro* studies can be performed to assess, for example, we it is possible to decorate fibers intracellularly. Furthermore, we can study whether nanoparticles that have stabilized amyloid formation (MUS:OT 9:1) can have a chaperoning effect and

#### 5.6 Final remarks

The vast majority of potential applications for the discoveries described in this thesis will be judged and evaluated by the scientific community at large, through reproducibility of the experiments and progressive experimentation towards both scientific insight and practical applications. It is impossible to envisage the ramifications of a project of this nature in the long term. Furthermore, this has been only a first step in the systematic understanding of how nanoparticles interact with fibrous protein materials. This work will continue being carried out with other bio-fibrillar materials such as collagen and actin fibers, to better understand what nanoparticle properties dictate such interactions. Only the results will tell how these interactions take place, but so far, the discriminative adsorption described in chapter 4 is unique to small MUS:OT gold nanoparticles and amyloid fibers. It is possible that other small nanoparticles behave identically, say, pegylated or sufficiently soluble carboxylated AuNPs. It is also possible that small MUS:OT AuNPs also adsorb discriminatively onto other fibers, such as actin, or even on viruses and smaller proteins. Such results would only confirm an underlying hypothesis approached by this thesis: small amphiphilic nanoparticles adsorb preferentially to specific proteinaceous interfaces. Finally, we believe it rests on the amyloid community to use our nanoparticles in their research. Figure 5.3 shows a simple Venn diagram of how we see the potential utility of these nanoparticles in the study of amyloid fibers, as a potential cross-technique probe, that can reconcile observations made in cryo-EM with spectroscopic measurements obtained by NMR specialists. The engineering of the nanoparticles will be improved to fine tune their size distributions and improve our knowledge on the nature of their ligand shell, which will only improve the quality of this novel potential tool in biology.

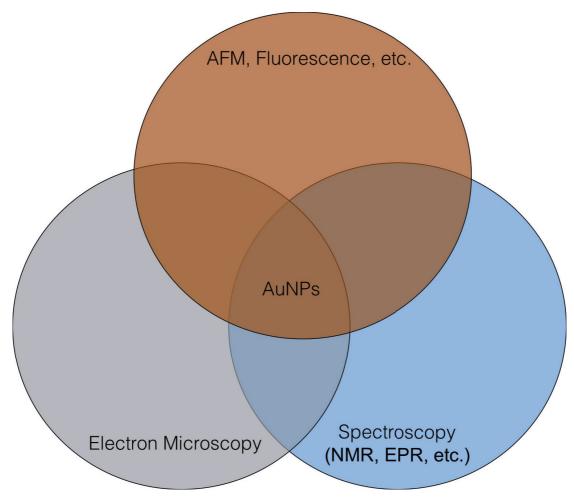


Figure 5.3 A Venn diagram of how we see the possible role that nanoparticles of the type described in this thesis can play in the study of amyloids and other proteins. Such AuNPs are amenable to several chemical modifications that render them flexible tools to study different aspects of challenging topics such as amyloidosis. For example, in this thesis, we've shown how by simply adding MUS:OT AuNPs we could readily identify two and three-fold symmetric  $A\beta_{1-40}$  polymorphs. More in-depth and careful experimentation hold enormous potential for the use of these novel materials in the efforts to understand biological macrostructures and other complex systems through a multi-instrumental approach.

## M. Methods

Unless otherwise indicated, all chemicals were purchased from Sigma Aldrich. Only the <sup>1</sup>H-NMR spectra of final products, key to this project, are shown. All <sup>1</sup>H-NMR were acquired in a Bruker Avance 400 MHz or in an Avance III 400MHz. Yields and mass spectra are not reported in this version. This section intends to enable anyone to reproduce the results showed in this thesis, and explain how experiments were made. It is not an orthodox organic synthetic chemistry report, nor an exhaustive description of each sample. Instead, it explains in sufficient detail how to prepare and characterize the nanoparticles. It also shows the difficulty in finding experimental techniques amenable to both amyloid fibers and nanoparticles, and examples of the results obtained routinely in kinetic assays of amyloid growth.

## M.1 Ligand synthesis

#### M.1.1 Synthesis of sulfonated ligands

Figure M.1 shows the synthetic route used to produce gram-scale sulfonated thiols, modified from reference<sup>103</sup>.

Figure M.1 Synthetic route amenable for gram-scale sulfonated thiolate molecules. During my thesis work, I have produced molecules with x = 4, 5, 6, 7, 8, 10 and 11. For large scale syntheses, the UV irradiation step may need longer illumination.

The modifications to the original synthesis<sup>103</sup> of MUS is described below. A gram-scale synthesis is outlined, adaptable to scales from 1 to 40 g of precursor. A synthesis using 25 mL of the precursor is described.

**Sodium undec-10-enefulfonate:** 11-bromo-1-undecene (25 mL, 111.975 mmol), Sodium Sulfite Na<sub>2</sub>SO<sub>3</sub> (28.75 g, 227.92 mmol) benzyltriethyl-ammonium bromide (10 mg) were added to a mixture of 200 mL methanol and 450 mL DI-water (4:9 MeOH:H<sub>2</sub>O ratio) in a 1 L round bottom flask. The mixture was refluxed at 102°C for 48h. The mixture was extracted

with diethyl ether 5 times, (5 x 400 ml), and the aqueous phase was evaporated in a rotary evaporator. The white powder was dried under high vacuum, suspended in pure ethanol and filtered. The methanolic solution was evaporated, and the process was repeated twice, to decrease the amount of inorganic salts. Usually, about 33 g of white, methanol soluble power was collected at this scale. <sup>1</sup>H-NMR (D<sub>2</sub>O): 5.76 (m, 1H), 4.78 (m, 2H), 2.69 (t, 2H), 1.53 (m, 2H), 1.11 (br s, 12H).

Sodium 11-acetylthio-undecanefulfonate: Sodium undec-10-enefulfonate (33 g, 147.807 mmol) was dissolved in 500 ml of methanol. A 2.6 times excess of thioacetic acid (27.324 mL, 384.3 mmol) was added to the solution and stirred in front of a UV lamp overnight (12h). The solution was evaporated in a rotary evaporator until the solid residue turned orange-red. The solid was washed with diethyl ether, until no colored material could be removed. The solid was dried under high vacuum, and then dissolved in methanol producing a yellow solution. About 3 g of carbon black was added to the solution, vigorously mixed, and the mixture was filtered through celite in a fluted filter paper. The filtered solution was clear, the solvent completely evaporated and about 35 g of white solid was collected. <sup>1</sup>H-NMR (D<sub>2</sub>O): 2.69 (t, 4H), 2.17 (s, 3H), 1.53 (m, 2H), 1.39 (m, 2H), 1.11 (br s, 14H).

11-mercapto-1-undecanesulfonate (MUS): Sodium 11-acetylthio-undecanefulfonate was refluxed at 102°C in 400 mL of 1M HCl for 12 h. 200mL of 1M NaOH was added to the final solution, additional 400 mL of DI-water was added to create a 1 L volume. The clear solution was kept at 4°C and crystallized overnight. The viscous white product was centrifuged down in 50 mL falcon tubes, and dried under high vacuum. 12 g (about 30% yield) of methanol soluble MUS is collected from this purification step. More material can be extracted from the supernatant of the centrifugation step, by reducing volume and keeping it at 4°C. <sup>1</sup>H-NMR (D<sub>2</sub>O): 2.69 (t, 4H), 2.34 (t, 3H), 1.53 (m, 2H), 1.39 (m, 2H), 1.11 (br s, 14H). Calculated mass 290.42 g/mol.

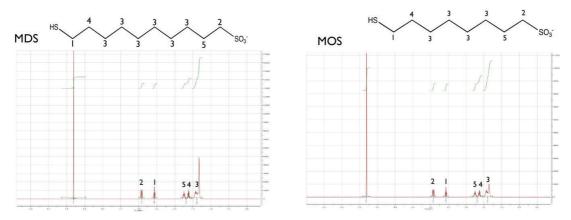


Figure M.2  $^{1}$ H-NMR (D<sub>2</sub>O) of 10-mercapto-1-decanesulfonate (MDS) and 8-mercapto-1-octanesulfonate. Both syntheses were done at the 4-5 g scale, following the same steps in Figure M.1.

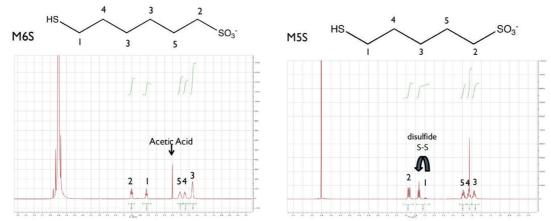


Figure M.3  $^{1}$ H-NMR (D<sub>2</sub>O) of 6-mercapto-1-haxanesulfonate (M6S) and 5-mercapto-1-pentanesulfonate (M5S). Smaller chains tend to form disulfides in the de-protecting step under HCl. This issue has been recently circumvented by de-protecting under inert conditions. Both syntheses were done at the 4-5 g scale, following the same steps in Figure M.1.

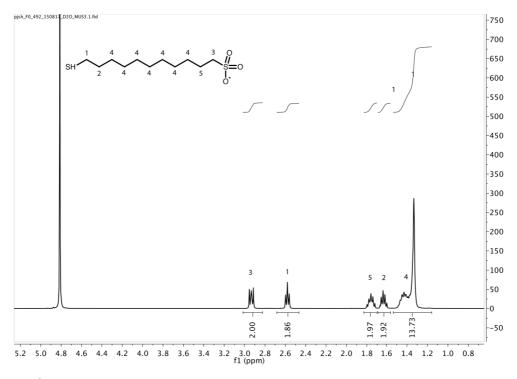


Figure M.4  $^{1}$ H-NMR ( $D_{2}O$ ) of 11-mercapto-1-undecanesulfonate (MUS) synthesized at a 15 g scale, following the steps in Figure M.1. This synthesis was performed several times, and crystallization yields a clear NMR baseline.

The synthesis of sulfonated ligands is straightforward and reproducible following this approach. Crystallization from water yields pure, methanol-soluble products that can be used directly to synthesize nanoparticles. For methanol solubility, crystallization from acidic water is recommended: to a volume V of 1M HCl, add V/3 of 1M NaOH. The material did not crystallize from 1M HCl, and the powder collected is not methanol-soluble when crystallized from a pH 7 solution. Ligands shorter than 7 carbons do not crystallize in the conditions described. Crystallization from water probably excludes disulfide bi-products, which renders the aqueous approach applicable to molecules longer than 7 carbons. To avoid disulfide formation, performing the de-protection step in dry inert conditions (dry, degassed methanolic HCl) solves the problem. Dry methanolic HCl under inert conditions, (using acetyl chloride in methanol) is a better de-protection scheme in this case: the volatiles can then be evaporated, and serial evaporations with solvents like toluene or hexanes yield a pale yellow powder. Water-soluble nanoparticles could be synthesized in the one phase protocol using all sulfonated ligands prepared with this method. The 2 and 3 carbon long mercaptosulfonates are commercially available; the former is MESNA, a pharmaceutical anti-cancer adjuvant used to mitigate urotoxicity<sup>197</sup>.

## M.1.2 Synthesis of quaternary amine terminated thiols (TMA)

**Figure M.5** Synthetic route amenable for gram-scale of cationic trimethylamine terminated thiolate molecules. During my thesis work, I have produced molecules with x = 4, 5, 6, 7, 8, 10 and 11. For large scale syntheses, (30 g above) UV irradiation may require longer than 12 h to complete the reaction. This synthesis was adapted from reference <sup>198</sup>

N,N,N-Trimethyl-10-undecenylammonium chloride: 11-bromo-1-undecene (25 mL, 111.975 mmol) was added to 300 mL of an ethanolic Trimethylamine solution (31-35 wt. % in ethanol, 4.2 M) and stirred for 2 days at room temperature. The solvent was evaporated, the yellow powder was dissolved in ~50mL DCM, and precipitated into hexane (500 mL) in a 1L beaker, yielding 30 g of white solid.

N,N,N-Trimethyl(11-mercaptoundecyl)ammonium **Chloride:** N,N,N-trimethyl(10undecenyl)ammonium bromide (30 g, 102.6 mmol) and thioacetic acid (21 mL mL, 308 mmol, ACROS) in 500 mL of methanol was and stirred in front of a UV lamp overnight (12h). The volatiles were removed in a rotary evaporator until the product became orange-red. The residue was washed several times with diethyl ether until not more orange bi-product could be removed. The product was dried under high vacuum, then dissolved in 300 mL of methanol, to which ~3 g of carbon black was added, vigorously mixed, followed by filtration through celite in a fluted filter paper. The clear solution was evaporated, yielding 32 g of white powder. This product was then dissolved in 400 mL of 1M HCl, and refluxed at 102°C overnight (~12 h). The pH was raised by the addition of 100 mL 1M NaOH, followed by the addition of 400 mL of MilliQ water, placed inside a 4°C. Thin elongated crystals grew, and were collected via centrifugation-assisted decantation. Vacuum filtration is not advised. After drying, ~10 g of a "shiny" crystalline powder was collected. <sup>1</sup>H-NMR(D2O): 1.24-1.49 (m, 14H), 1.53-1.66 (m, 2H), 1.67-1.84 (m, 2H), 2.52 (t, 8 Hz, 2H), 3.12 (s, 9H), 3.30-3.41 (m, 2H).

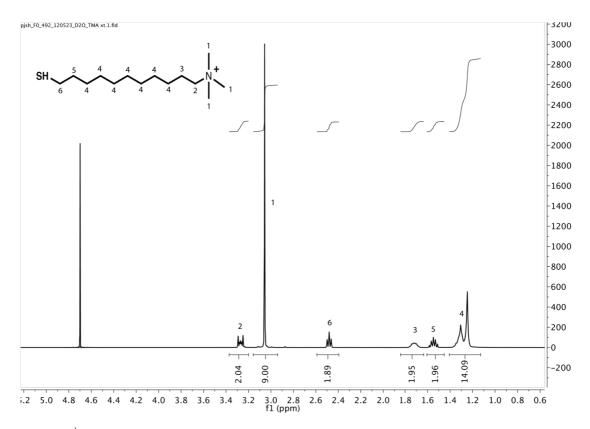


**Figure M.6** <sup>1</sup>H-NMR (D<sub>2</sub>O) N,N,N-Trimethyl-10-undecenylammonium chloride (TMA). ~10 g synthesis scale, produced as described above.

This synthesis is a modification to reference <sup>198</sup>; the shorter ligands have not been reported, but The shorter versions of this molecules, from 10 to 4 (except 6) carbons long have also been synthesized, following the same protocol. Below 7 carbons, crystallization was not observed; sequential evaporations with addition of toluene or hexanes to the final product yielded the product. These molecules have not been exploited much in this work, thus, for brevity, we omit their spectra.

#### M.1.3 Synthesis of zwitterionic ligand

Figure M.7 Synthesis of sulfobetaine terminated thiol. 3-[(11-Mercapto-undecyl)-N,N-dimethyl-amino]-propane-1-sulfonate, modified from reference 115

This synthesis was performed only once, with this length.

11-bromo-1-undecene (15 mL, 68.4 mmol) was added to a solution of 2 M dimethylamine in THF (AcroSeal<sup>™</sup>, ACROS Organics<sup>™</sup>) and the reaction mixture was stirred 48 h at room temperature. The volatiles were evaporated in a rotary evaporator. A yellow oil remained, to which 200 mL of 1 M was NaOH was added, followed by an extraction with DCM. The DCM phase was separated, dried with anhydrous sodium sulfate, filtered, and concentrated in vacuo as a yellow oil. 6.02 g of this oil was added to 100 mL of dry acetone (AcroSeal<sup>TM</sup>, ACROS Organics<sup>TM</sup>), followed by addition of 1,3-propanesultone (1.6 mL, 38.25 mmol): the reaction mixture was stirred at room temperature for two days. The white precipitate was filtered, and the resulting solid was washed with excess acetone, then dried under high vacuum. 4 g (~11.68 mmol) of the power was dissolved in methanol with thioacetic acid (1.426 mL, 20 mmol) and stirred at room temperature in front of a UV lamp. Volatiles were removed in a rotary evaporator, yielding a yellow oil. 20 mL of methanol was added to this oil, and this solution was added drop-wise into 400 mL of dry acetone (AcroSeal<sup>TM</sup>, ACROS Organics<sup>TM</sup>). The white precipitate was filtered using vacuum filtration and dried under vacuum. A solution of methanolic HCl was prepared by adding 3.56 mL (50 mmol) of acetyl chloride to 50 mL of methanol. The powder was added to this mixture and refluxed overnight. The volatiles were evaporated in a rotary evaporator, which produced a yellow oil. Toluene was added and evaporated from this oil until a pale yellow powder formed (~3 g). <sup>1</sup>H NMR (D2O) is shown in Figure M.8. This synthesis is a modification from reference 115, and several steps were modified. Of notice, the intermediate in the third step can be recrystallized for higher purity. The de-protection reported by the authors in basic conditions created disulfides in our

synthesis; methanolic HCl is a robust alternative. The only sensitive step of the reaction is the de-protection that we recommend be done under inert conditions.

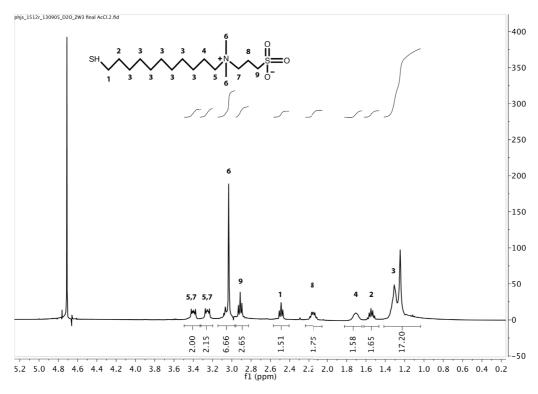


Figure M.8  $^{1}$ H-NMR (D<sub>2</sub>O) of sulfobetaine terminated thiol. 3-[(11-Mercapto-undecyl)-N,N-dimethyl-amino]-propane-1-sulfonate.

## M.2 Nanoparticle synthesis and characterization

To address the issue of nanoparticle batch-to-batch reproducibility, several syntheses under the same conditions were performed. The project began with a comprehensive assessment of how different compositions of MUS:OT nanoparticles and MUS:brOT affected the growth kinetics of amyloid fibers. To address the issue of batch-to-batch reproducibility, each composition was prepared three times (triplicates), in increments of 10% 1-octanetiol (and brOT, which is ongoing work). This means that three batches of allMUS, MUS:OT 9:1, 8:2, 7:3 all the way to 1:9 and allOT were produced. The result of the ligand composition measured by NMR versus the feed ratio is shown in Figure 2.7. Here I describe the methods to produce the nanoparticles used in this work, and the characterization of representative samples. An exhaustive characterization of all batches produced is prohibitively lengthy and is still on-going. High-throughput assays can be performed faster than our ability to fully characterize each batch: thus, a general scheme of relevant characterization is presented, and particles that were used in the body of the thesis are highlighted.

The general synthesis for one phase nanoparticles in this thesis followed, with some modifications, the report in <sup>112</sup>. The main difference lies on the purification of the particles. From a strict point of view, the nanoparticles were not purified: they were washed and cleaned of impurities. They are not amenable to column chromatography, crystallization or other conventional purification techniques; the closest we get to a purification step is the sucrose-gradient size fractionation. Increasingly, nanoparticles are being crystalized and completely characterized as atomically defined gold clusters <sup>94,199</sup>. In theory, the manipulation of these nanoparticles can evolve in this direction, providing unambiguous characterization of the species, that can be of great value to domains such as molecular structural biology, drug discovery, medicine and others <sup>104,151,173</sup>.

#### M.2.1 One phase allMUS and MUS:OT synthesis

All glassware was cleaned with fresh aqua regia (HCl:HNO<sub>3</sub> 3:1) before synthesis.

Generally, in a 500 mL round bottom flask, 0.9 mmol of gold salt (HAuCl<sub>4</sub>·3H<sub>2</sub>O) in 200 mL ethanol and 0.9 mmol of the desired thiol ligand mixture was added while stirring the reaction solution. This might be a crucial step in determining ligand ratio, because a gold-thiol complex forms, which is evidenced by the increasing turbidity of the mixture. A filtered, saturated ethanol solution of sodium borohydride (NaBH<sub>4</sub>) was added drop-wise. The solution was stirred for 2 h and the reaction vessel was kept at 4°C overnight; a black precipitate was collected via decantation. This residue was washed several times (5X each step) with ethanol, methanol and acetone, then dried under vacuum. To completely remove unbound species, particles were either dialyzed using cellulose membranes (MWCO 3500) or centrifuged several times with MilliQ water using Amicon® Ultra-15 Centrifugal Filter Devices (10k or 30k NMWL). The particles were then suspended in a small amount of water (~2 mL) and freeze dried. The powder could then be weighed and manipulated accordingly.

In a typical modification to this synthesis, to produce the triplicate series, to a 250 mL round-bottom flask we added 70 mL of absolute ethanol. We added 118.15 mg (0.3 mmol) of tetrachloroaurate  $HAuCl_4\cdot 3H_2O$  to the flask, which gave a yellow solution. In a separate glass vial, 87.13 mg of MUS (~0.3 mmol) was dissolved in 15 mL of methanol, aided by sonication. The methanolic MUS solution was filtered through a PTFE syringe filter into another vial. Concomitantly, a saturated NaBH<sub>4</sub> ethanolic solution was prepared, filtered, and added to a

dropping funnel. The ligand solution was added to the ethanolic gold mixture, allowed 10 minutes to stir, which turned the mixture opaque, followed by the drop-wise addition of the reducing agent. This synthesis was repeated several times, using different 0.3 mmol sums of MUS and OT.

This synthetic approach was not amenable to TMA ligands: the ethanolic gold solution becomes intensely orange upon TMA addition, and precipitation is visible. The addition of the reducing agent yields nanoparticles up to 40 nm in diameter. This approach was also not adequate for the zwitterionic ligand: the nanoparticles did not form. Both these particles were synthesized through modifications to the Stucky synthesis <sup>119</sup>.

## M.2.2 Stucky allMUS and MUS:OT synthesis

A 9:1 mixture of DMF and MilliQ water was prepared in a 250 mL round-bottom flask. Three different 20 mL aliquots of this mixture were used to completely dissolve the reagents in separate vials: (i) 277.7 mg (0.56 mmol) of chloro(triphenylphosphine)gold(I); (ii) 346 mg (1.2 mmol) of MUS with 56 μL (0.3 mmol) of OT and (iii) 142.3 mg (1.5 mmol) of borane tert-butylamine complex. Dissolution was completed by sonication for 15 minutes at room temperature. The gold-salt solution was added to the round-bottom flask, followed by addition of the MUS:OT (4:1) mixture. The solution was stirred under 800 rpm for 10 minutes at room temperature and became turbid. We added the reducing agent solution, connected the flask to a condenser, in an oil bath at 125°C (800 rpm) for 1.5 h. After this, the reaction flask was taken out of the heating bath and cooled while stirring (800 rpm). The flask was then kept at 4°C overnight to precipitate: the black solid (nanoparticles) was collected by decantation.

The nanoparticles were washed by centrifugation using different solvents to remove unbound molecules. The washing steps were identical to those described in the one-phase synthesis.

## M.2.3 Stucky synthesis of allTMA and ZW nanoparticles

A 1:1 mixture of ethanol and toluene was prepared in a 250 mL round-bottom flask. Three different 20 mL aliquots of this mixture were used to completely dissolve the reagents in separate vials: (i) 277.7 mg (0.56 mmol) of chloro(triphenylphosphine)gold(I); (ii) 1.2 mmol of TMA or ZW ligand and (iii) 142.3 mg (1.5 mmol) of borane tert-butylamine complex. Dissolution was completed by sonication for 15 minutes at room temperature. The gold-salt solution was added to the round-bottom flask, followed by addition of the ligand solution. The mixture was stirred under 800 rpm for 10 minutes at room temperature. We added the reducing

agent solution, connected the flask to a condenser, in an oil bath at 125°C (800 rpm) for 1.5 h. After this, the reaction flask was taken out of the heating bath and cooled while stirring (800 rpm). Here, the methodology for ZW and allTMA nanoparticle synthesis departed: (i) ZW nanoparticles precipitated like the MUS and MUS:OT particles, and its cleaning procedure followed exactly that described above. (ii) allTMA nanoparticles did not precipitate; they remained stably soluble in the mixture. Thus, the volume was decreased in a rotary evaporator, which decreased the ethanol content of the mixture; once toluene was in a large enough excess, the nanoparticles precipitated. The washing protocol for allTMA nanoparticles was different because they are soluble in ethanol. All TMA NPs were washed by centrifugation using diethyl ether and toluene. The pellet was dried, dissolved in MilliQ water, followed by the usual Amicon® Ultra-15 centrifuge-assisted dialysis (10k or 30k NMWL). The particles were then suspended in a small amount of water (~2 mL) and freeze dried.

This synthesis scale usually gave  $\sim$ 80 mg of MUS-based particles and allTMA, but  $\sim$ 30 to 40 mg of ZW NPs: the cause of lower yield in the latter case is unknown.

## M.2.4 Nanoparticle characterization

Several techniques can be used to characterize the nanoparticles. Size distribution was routinely assessed under transmission electron microscopy (TEM). Nuclear magnetic resonance was used both to assess the presence of unbound ligands (which will shortly de demonstrated to be disulfides) and determine the ligand-shell composition. Thermogravimetric analysis (TGA), zeta-potential measurements, dynamic light scattering, UV-vis among other techniques have been used in different instances. Here we describe some of the batches relevant to this thesis and recent publications.

#### M.2.4.1 Ligand-shell composition determination

<sup>1</sup>H-NMR is used to determine if the particles are free of unbound ligand. During my work, I have noticed that the chemical shift of the unbound species does not correspond to CH<sub>2</sub>-SH, but rather to the disulfide species. Figure M.9 shows the differences between the two disulfide species, prepared using iodine (I<sub>2</sub>), Figure M.10 shows the difference between washing a nanoparticle batch 5 times and 10 times using dialysis filtration (MUS:OT via the Stucky method).

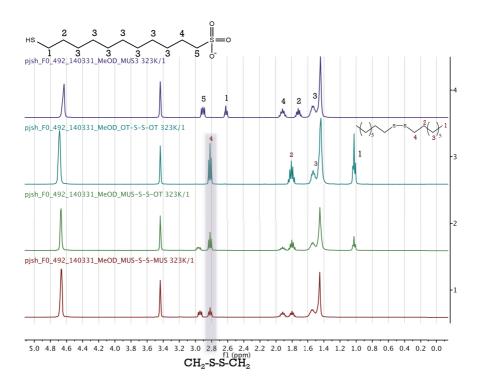
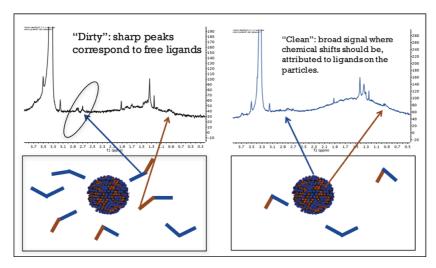


Figure M.9 <sup>1</sup>H-NMR (MeOD-d4) of MUS, OT, the disulfides produced by addition of  $I_2$  in the case of MUS:OT and only MUS. This figure depicts the shift in the CH<sub>2</sub>-SH



**Figure M.10** Blue represents MUS and orange OT. The "free ligands" have the chemical shift of disulfides. <sup>1</sup>H-NMR in MeOD-d4 and 5% D<sub>2</sub>O ensures both MUS and OT solubility. These are the spectra for MUS:OT nanoparticles prepared via Stucky method, comparing 5 water washes to 10. Instead of disulfides, the "free ligands" could be thiol-gold complexes that adsorb and desorb from the nanoparticles dynamically: however, the chemical shift of a -CH<sub>2</sub>-S-(Au)<sub>x</sub>-S-CH<sub>2</sub> would not necessarily coincide with that of disulfides. Further experimentation is needed to verify this hypothesis in case it is of interest. For now, I prefer reporting the excess ligands as disulfides based on the current evidence.

In washing the nanoparticles, the goal is to achieve a smooth spectrum, free of sharp peaks. Figure M.11 illustrates the probable contaminants, and a spectrum of a nanoparticle sample that can be deemed clean by <sup>1</sup>H-NMR. For mixed-ligand nanoparticles, the solvent used must

contemplate both molecules. If a bad solvent is used, the signal can be broadened independently of the absence of free species. The right-hand panel in Figure M.11 shows the difference between using  $D_2O$  and a mixture of  $D_2O$  and MeOD-d4: the terminal methyl group of OT is revealed with the deuterated methanol. Due to the low amount of sample, the spectrum must be zoomed in, and the sharp peaks in the green line come from the MeOD-d4.

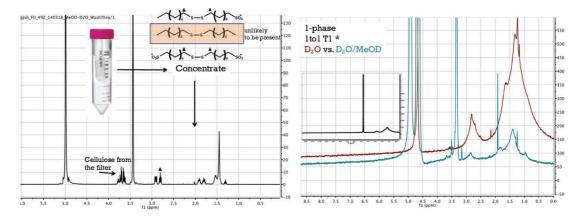


Figure M.11  $^{1}$ H-NMR of the supernatant extracted from the nanoparticles during the washing procedure. The aqueous phase carries possibly two types of disulfides that agree with the spectrum. The spectrum was acquired in  $D_{2}O$ , thus is it unlikely the disulfide formed only by the hydrophobic ligand is present. On the right, a comparison between the nanoparticle NMR in  $D_{2}O$  and a mixture with MeOD-d4: the  $-CH_{3}$  group is "revealed" with the methanol. The inset shows the typical clean spectrum of a one phase batch, used in chapters 3 and 4.

Figure M.12 summarizes the technique used to determine the stoichiometry of the ligand shell for the particles used in this thesis. An etching solution of 15 mg of Iodine (Acros) in 100 mL of MeOD-d4 (Sigma) is prepared. Between 1 to 5 mg of nanoparticles is suspended in 0.6 mL of the etchant mixture for 30 min under sonication. A precipitate forms, which, in this work, has not changed the quality or quantification under <sup>1</sup>H-NMR: in other words, performing the ligand stoichiometry calculation with only the supernatant or including the precipitate did not affect the results. There are other ways to etch the nanoparticles to calculate the ligand ratio using <sup>1</sup>H-NMR; for example, using cyanide or thermal decomposition. The choice of etchant varies with the particle system, and for MUS:OT, the I<sub>2</sub>-MeOD-d4 approach was chosen because of the clarity of the spectrum. If cyanide is used in this system, several side-reactions take place and produce peaks difficult to interpret. The main results obtained from the approach outlined by Figure M.12 can be found in Figure 2.7 in chapter 2.

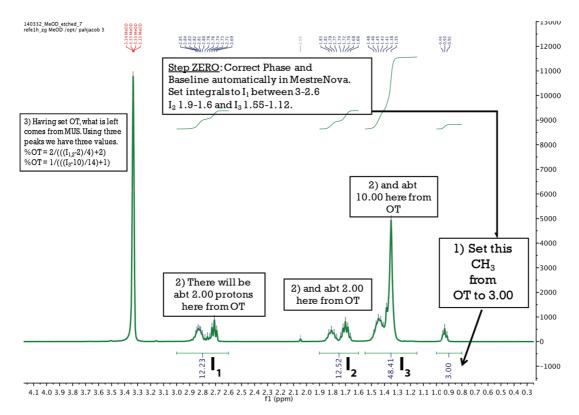
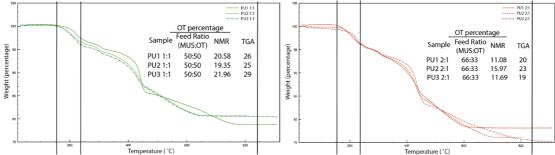


Figure M.12 Schematic approach to determine the ligand-ratio for MUS:OT nanoparticles used in this thesis. This comes from a sample synthesized using the Stucky method,

#### M.2.4.2 Thermogravimetric analysis (TGA)

TGA is often used to determine the organic content of monolayer-protected gold clusters to estimate the number of Au-S bonds and surface coverage<sup>110,200</sup>. It measures the mass of a sample as a function of increasing temperature and can be used to study several phenomena, including oxidation and thermal decomposition <sup>201,202</sup>. The nanoparticles used in this work are too polydisperse to allow a precise, quantitative treatment of the TGA data; however, it offers an estimate of the organic content of the sample. It can also be used to estimate the relative abundance of the different ligands in our nanoparticles, given they have discernible thermal decompositions. Data interpretation from TGA requires understanding of experimental the set up: for example, in an open crucible, under N<sub>2</sub> flow, a drop in mass cannot be attributed to the boiling point, but rather drying, desorption or sublimation. The sample can lose mass well before the boiling point, so only a set up with a small hole on the lid that equilibrates the vapor phase and the sample can offer a clear boiling point-related mass decay. The equipment we use is a TGA 4000 from Perkin Elmer, and Figure M.13 shows TGA's of recently synthesized nanoparticles, and an approach developed to determine ligand ratio, which is compared to the <sup>1</sup>H-NMR determination shown in Figure M.12.



**Figure M.13** TGA plots of recently one phase synthesized MUS:OT nanoparticles. The three vertical lines on the plots demark 176°C, 233°C and 833°C. OT thermally leaves the crucible between the first two indicated temperatures, whereas MUS degrades at about ~430°C. There is rough agreement between the 1H-NMR determined ratios and that derived from the TGA data: the latter reports a higher MUS content. This can result from the thermal degradation of other species in the temperature range associated to MUS that over-represents this signal. An experimental setup designed to capture the boiling point would have a much sharper drop in mass as a function of time: this type of TGA curve is indicative of drying, desorption and thermal degradation. Image and data kindly provided by Zekiye Pelin Guven

## M.2.4.3 Representative TEM analysis of nanoparticles

All TEM images were acquired in a Philips CM12 TEM or an FEI TALOS<sup>TM</sup> Electron Microscope.

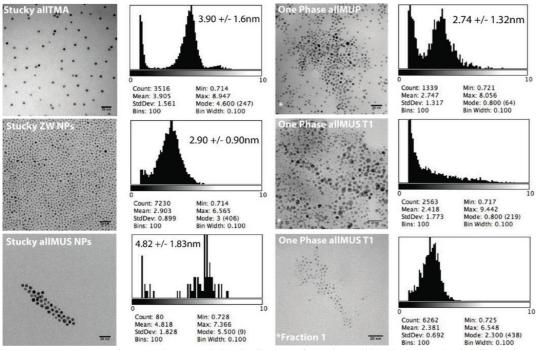


**Figure M.14** Representative TEM images and size distributions of samples used in this thesis. The size distributions were obtained using a threshold based particle analysis in ImageJ, please refer to the discussion in Figure 2.6 for the limitations of this approach.

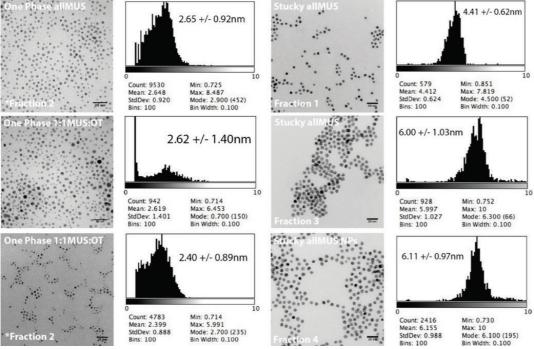


**Figure M.15** Representative TEM images and size distributions of samples used in this thesis. On the right, an illustration of the outcome from sucrose gradient size-fractionation performed on an allMUS Stucky synthesized batch.

Ideally, a final characterization should look like the supplemental information of our recent publication, discussed in chapter 2.

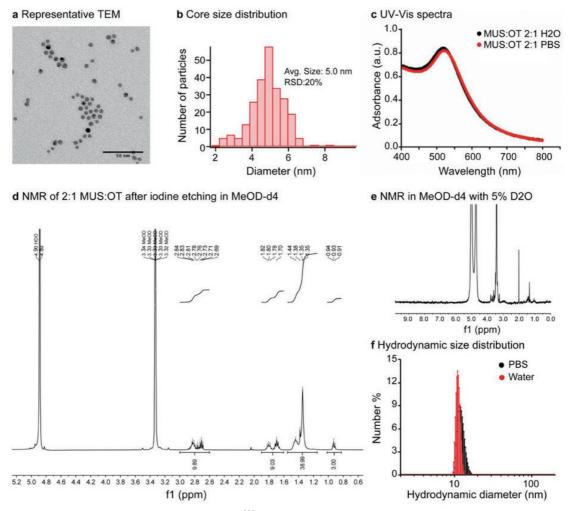


**Figure M.16** This image, reproduced from reference <sup>116</sup> summarizes the recommended characterization techniques to describe the nanoparticles we produce. This particle was synthesized with the Stucky method, and used in chapter 4 to demonstrate the role of nanoparticle size in the discriminative adsorption onto amyloid fibers.

## M.3 Preparation of amyloid fiber experiments

#### M.3.1 Preparation of $A\beta_{1-40}$ and $A\beta_{1-42}$ experiments

**Tris Buffer:** 12.114g of Trizma base, 2.922g NaCl (50 mM) and 0.2g NaN3 (0.02%) was added to 1L, pH 7.4 in MilliQ water.

NH4OH: 0.1% in MilliQ water

**13mM Basic sodium phosphate buffer (PBS):** 184.54 mg of Na<sub>2</sub>HPO<sub>4</sub>, 292 mg of NaCl and 0.02 g of NaN<sub>3</sub> were added to 100 mL MilliQ water. The solution was stirred, sonicated, then filtered in 50 mL syringe filters through 0.2μm PTFE filters, into a glass bottle. Final concentration of 13 mM Na<sub>2</sub>HPO<sub>4</sub> and 50 mM NaCl (0.02% NaN<sub>3</sub>).

**13mM Acidic sodium phosphate buffer (PBS):** 389.84 mg of NaH<sub>2</sub>PO<sub>4</sub>, 730.5 mg and 0.05 g of NaN<sub>3</sub> were added to 250 mL of MilliQ water, stirred and sonicated. The solution was filtered through a 50 mL with 0.2μm PTFE syringe filters. Final concentration of 13 mM NaH2PO4, 50 mM NaCl, 0.02% NaN<sub>3</sub>. To achieve pH 7.4 PBS, acidic PBS was added to the basic until the target pH was achieved (constant pH monitoring using a Hamilton pH-meter).

**Thioflavin T (ThT)**: 0.32 g of ThT (1μmol) as added to 10 mL of MilliQ water yielding a 100 μM solution: it was filtered through a 0.2μm PTFE syringe filter.

## M 3.2 Aβ sample preparation and kinetic assays

For a detailed protocol on how to prepare A $\beta$  samples, refer to  $^{203}$ .

The  $A\beta_{1-40}$  and  $A\beta_{1-42}$  used in this thesis were used as purchased from the Keck Laboratories, and then from ChinaPeptides. The lyophilized material was dissolved in a 1:1 mixture of 0.1% NH<sub>4</sub>OH and 100 mM Tris buffer, 0.02 % NaN<sub>3</sub> pH 7.4 at roughly 1 mg/mL.

Solutions were ultracentrifuged for 1 hour at 55 krpm at 4°C in a Beckman ultracentrifuge-

The upper half of the supernatant was collected and the peptide concentration was determined using its extinction coefficient at 280 nm (1490 M<sup>-1</sup>cm<sup>-1</sup>). A Perkin Elmer UV-vis, or the Tecan plate-reader were used to perform these measurements.

The supernatant was then diluted to the desired concentration (usually between 5 to 20  $\mu$ M) with the 13 mM PBS (pH = 7.4) described above.

Fibers were either grown in a plate reader assay, or inside 1 mL Eppendorf tubes in a thermomixer. This approach gives reliable  $A\beta_{1-40}$  monomeric solution preparation but not  $A\beta_{1-42}$ . For experiments that rely on  $A\beta_{1-42}$  we recommend following a protocol that uses size exclusion chromatography  $^{166,203}$ .

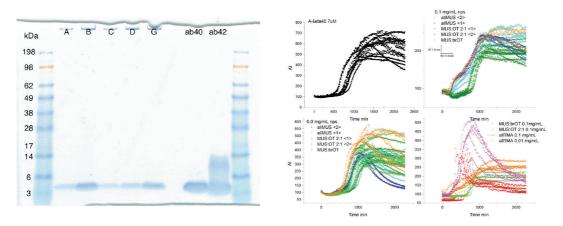
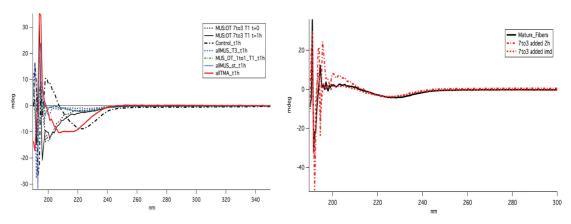


Figure M.17 SDS-PAGE of  $A\beta_{1-40}$  and  $A\beta_{1-42}$  monomeric solutions prepared using the centrifugation method. The approach is reliable for  $A\beta_{1-40}$  but not  $A\beta_{1-42}$ . On the right, typical ThT kinetic assay curves from multiple wells with the different types of nanoparticles show that this sample preparation, for  $A\beta_{1-40}$  is reliable. Lanes A through G correspond to the remaining

monomers after incubation with different nanoparticles. Red curves correspond to cationic allTMA nanoparticles that accelerate amyloid formation. Blue curves correspond to allMUS one phase particles and green curves to MUS:OT one phase nanoparticles. This phenomenon was widely investigated, and will be further pursued in the future.



**Figure M.18** Circular dichroism (CD) of fibers with nanoparticles. On the left, the impact of forming the fibers in the presence of different nanoparticles is shown: the red line corresponds to the fast amyloid formation in the presence of allTMA NPs. The spectra also confirmed the inhibitory effect of MUS:OT (10% OT) nanoparticles. On the right, we tested the effect of nanoparticle addition on the fibers, immediately after adding the NPs (in this case, MUS:OT) and after 2 h at 1000 rpm and 37°C. No significant changes were detectable by adding the nanoparticles to the mature fibers. This type of experiment is still under investigation using also atomic force microscopy to verify changes to the fibers.

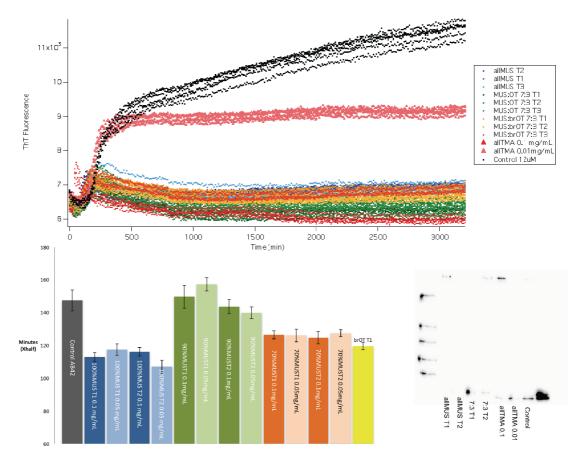


Figure M.19 Typical ThT kinetic assay with  $A\beta_{1-42}$  grown in the presence of the different types of nanoparticles. The bar graph shows the extracted nucleation times fitted to a sigmoidal curve: all nanoparticles accelerated the fibrillation kinetics of

 $A\beta_{1-42}$  but NPs with an MUS:OT ratio of 9:1 had the same timescale as the controls. A Western Blot was performed after centrifugating the samples: it indicates that the allMUS samples consumed all monomeric material, whereas MUS:OT nanoparticles stabilized a slightly heavier species.

The SDS-PAGE in Figure M.17 shows that  $A\beta_{1-40}$  monomeric solutions can be obtained using this approach, but  $A\beta_{1-42}$  shows higher order complexes.

Most of the images presented in the thesis were prepared in the absence of ThT, and the nanoparticles were added after fiber formation was complete. During the thesis work, several kinetic assays to examine the effect of nanoparticle ligand-shell on the nucleation and growth were performed in a plate reader. 90  $\mu$ l of A $\beta$  with 200  $\mu$ M ThT (from a 2mM stock solution in water) per well was incubated in the absence or presence of 10  $\mu$ l nanoparticles per well at 37 °C and shaken at 300 rpm in a 96 well black fluorescence plate, GREINER low binding 96-well plates. Measurements were made at regular intervals of 10 minutes with excitation and emission at 440 nm and 480 nm respectively.

### M.3.3 α-synuclein fiber growth

 $\alpha$ -synuclein was purchased from rPeptides and used as received. TBS buffer was prepared (50 mM Tris, 150 mM NaCl, pH = 7.5) and degassed with argon prior to use. To 1 mg of lyophilized powder, 1 mL of TBS buffer was added, the solution was filtered through a 100 kDa MWCO Microcon Filter (13000 g, 15 min, 4 °C). The concentration was adjusted to 40  $\mu$ M using the extinction coefficient at 275 nm of 5974 M<sup>-1</sup>cm<sup>-1</sup>. Both plate reader experiments and fiber preparations inside a thermomixer were performed. The images shown in the body of the thesis correspond to fibers grown over the period of one week at 1000 rpm and 37 °C. The sample was considered ready when negatively stained TEM samples showed abundant fibrillar material. Plate reader data for  $\alpha$ -synuclein was not reproducible across experiments like A $\beta_{1-40}$ .

### M.3.4 Tau fiber growth

Wild type Tau-441 was kindly provided by Nadine Ait Bouziad from Prof. Hilal Lashuel's group. A solution of 20  $\mu$ M Tau-441 was prepared by adding 1.7 mL of 13 mM PBS pH = 7.4 to 1.6 mg of the lyophilized powder. Five different aliquots of the Tau solution were prepared. To the largest 0.9 mL aliquot, heparin was added to a final concentration of 4  $\mu$ M, aiming a Tau-to-heparin 4:1 ratio. Because our MUS-based nanoparticles are also polyanions, I have tested in the other aliquots the fiber formation behavior of Tau, without heparin, but with the different nanoparticles used in this project: allMUS, MUS:OT, ZW NPs and allTMA. Negatively stained TEM was used to monitor fiber growth, which only occurred in the

Eppendorf tube with heparin. No fibers were observed for any of the nanoparticle-Tau mixtures over the course of 2 weeks in these conditions.

To test the adsorptive behavior of different nanoparticles onto grown Tau fibers, aliquots of 90  $\mu$ L of the Tau stock were placed in separate Eppendorf tubes. 10  $\mu$ L of the nanoparticle stock solution was added: allTMA, allMUS, MUS:OT (10 and 30% OT by  $^{1}$ H-NMR) and ZW NPs, in addition to fractionated allMUS and MUS:OT (30% OT by  $^{1}$ H-NMR). An experiment to test the role of nanoparticle concentration was performed: 10  $\mu$ L of 1mg/mL and 10 mg/mL MUS:OT (30% OT) were added: the results described in Chapter 4 indicate that first the nanoparticles cover small non-fibrillar species. Once such sites are covered, the nanoparticles occupy the body of the fibers.

# M.3 Electron microscopy of amyloid nanoparticle samples

## M.3.1 Dry negative staining TEM

For dry negative staining of amyloid fibers, a droplet of suspended fibers in buffer was deposited onto a carbon covered Copper TEM grid (400mesh) (PELCO<sup>®</sup> TEM grid TedPella, INC), washed with MilliQ and finally stained with a freshly prepared and filtered (0.22  $\mu$ m PTFE syringe filter) 2% solution of Uranyl acetate in MilliQ. The dried grid has been imaged in an FEI TALOS<sup>TM</sup> Transmission Electron Microscope.

## M.3.2 Cryo-TEM

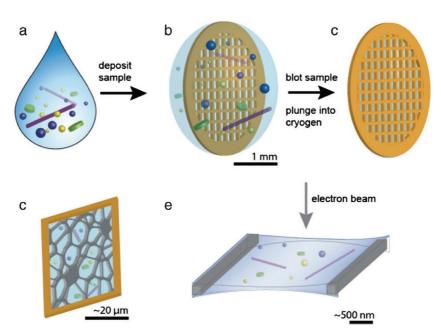


**Figure M.20** Schematic representation of a cryo-EM preparation: a sample in its native hydrated state (a) is deposited onto a TEM grid (b), blotted to leave only a very thin layer of liquid (c) that is flash frozen by plunging into a cryogen to be finally

imaged under an electron-beam (e). Reprinted with permission from reference <sup>204</sup> Copyright © 2012 Elsevier Ltd. All rights reserved.

For cryo electron microscopy a droplet of amyloid fibers suspended in buffer is flash-frozen in its native hydrated state. Therefore, a droplet has been deposited on a Quantifoil® holey carbon grid and blotted to a thin (100-300nm) layer of liquid that was flash frozen in liquid ethane using an FEI vitrobot Marc IV. Imaging was performed in a Gatan single tilt cryo holder with an FEI Tecnai Spirit BioTWIN 80kV transmission electron microscope in LowDose Mode to visualize the samples at an average exposure of 1-3electrons/Ångström<sup>2</sup>.

## M.4 Experiments omitted from the thesis

### **M.4.1 AFM**

Atomic Force Microscopy was performed during this thesis work, but yielded difficult images to interpret. Electron microscopy provides good contrast between the metallic core of the gold nanoparticles and the carbon-based amyloid fibers. Figure M.21 shows typical dry AFMs obtained after preparing  $A\beta_{1-40}$  in the presence of nanoparticles. Perhaps now that the adsorptive behavior of these nanoparticles onto amyloid fibers has been established, AFM can be used to investigate mechanical properties of the interaction, the effect of the nanoparticles on the fuzzy coat of Tau among other possibilities.

Other techniques were used with varying degree of success: ultimately, no approach was ideal for both nanoparticles and amyloid fibers. For example, in this work we discovered that, in the presence of buffer and amyloid precursors, our nanoparticles do not flow through the stationary phase in size exclusion chromatography (Superdex 200). It has also been difficult to assess the affinity of the different nanoparticles to the amyloid fibers. Surface plasmon resonance experiments (SPR) showed that the NPs have different affinities to the substrate. Deconvoluting affinity to the substrate from possible binding to the fibers is still a challenge, but can be achieved with careful controls and calibration.

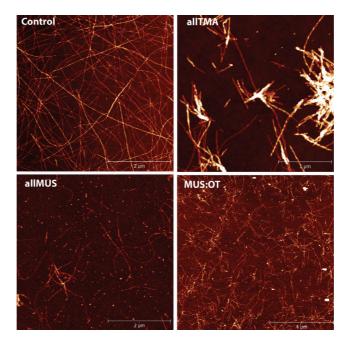


Figure M.21 Dry AFM imaging of  $A\beta_{1-40}$  grown in the presence of the nanoparticles indicated in each image. AFM is a promising technique to study the interaction between these two materials, but clarity to visualize the gold core was needed to advance the project: now that the different adsorptive behaviors are well-established, AFM can be used to analyze forces, the effect of nanoparticles on mechanical properties of the fibers, among other possibilities. (Bruker Cantilever 40 N/m).

## **Bibliography**

- 1. Dill, K. A. & MacCallum, J. L. The Protein-Folding Problem, 50 Years On. *Science* **338**, 1042–1046 (2012).
- 2. Anfinsen, C. B. *Principles that Govern the Folding of Protein Chains on JSTOR*. (Science, 1973).
- 3. Gregersen, N., Bross, P., Vang, S. & Christensen, J. H. Protein misfolding and human disease. *Annual Review of Genomics and Human Genetics* **7**, 103–124 (2006).
- 4. Chiti, F. & Dobson, C. M. Amyloid formation by globular proteins under native conditions. *Nat. Chem. Biol.* **5**, 15–22 (2009).
- 5. Hartl, F. U. Molecular Chaperones in the Cytosol: from Nascent Chain to Folded Protein. *Science* **295**, 1852–1858 (2002).
- 6. Mann, M. & Jensen, O. N. Proteomic analysis of post-translational modifications. *Nat Biotechnol* **21**, 255–261 (2003).
- 7. Cutting, G. R. Cystic fibrosis genetics: from molecular understanding to clinical application. *Nature Reviews Genetics* **16**, 45–56 (2015).
- 8. Epstein, F. H. & Bunn, H. F. Pathogenesis and Treatment of Sickle Cell Disease. *N Engl J Med* **337**, 762–769 (1997).
- 9. Surtees, R. & Blau, N. The neurochemistry of phenylketonuria. *Eur J Pediatr* **159**, S109–S113 (2000).
- 10. Adler-Abramovich, L. *et al.* Phenylalanine assembly into toxic fibrils suggests amyloid etiology in phenylketonuria. *Nat. Chem. Biol.* **8,** 701–706 (2012).
- 11. Macario, A. & de Macario, E. C. Mechanisms of disease Sick chaperones, cellular stress, and disease. *N Engl J Med* **353**, 1489–1501 (2005).
- 12. Querfurth, H. W. & LaFerla, F. M. Mechanisms of disease. *N Engl J Med* (2010).
- 13. De Strooper, B. & Karran, E. The Cellular Phase of Alzheimer's Disease. *Cell* **164**, 603–615 (2016).
- 14. Kalia, L. V. & Lang, A. E. Parkinson's disease. *Lancet* **386**, 896–912 (2015).
- 15. Wang, Y. & Mandelkow, E. Tau in physiology and pathology. *Nat Rev Neurosci* **17**, 22–35 (2015).
- 16. Fanciulli, A. & Wenning, G. K. Multiple-system atrophy. *N Engl J Med* **372**, 1375–1376 (2015).
- 17. Aguzzi, A. & Calella, A. M. Prions: protein aggregation and infectious diseases. *Physiol. Rev.* **89**, 1105–1152 (2009).
- 18. Knowles, T. P. J., Vendruscolo, M. & Dobson, C. M. The amyloid state and its association with protein misfolding diseases. *Nat. Rev. Mol. Cell Biol.* **15**, 384–396 (2014).
- 19. Sipe, J. D. & Cohen, A. S. Review: History of the Amyloid Fibril. *J. Struct. Biol.* (2000).
- 20. Sipe, J. D. *et al.* Nomenclature 2014: Amyloid fibril proteins and clinical classification of the amyloidosis. *Amyloid* **21,** 221–224 (2014).
- 21. William Thomas Astbury, S. D. K. B. The X-ray interpretation of denaturation and the structure of the seed globulins. *Biochemical Journal* **29**, 2351 (1935).
- 22. EANES, E. D. & GLENNER, G. G. X-RAY DIFFRACTION STUDIES ON AMYLOID FILAMENTS. *Journal of Histochemistry & Cytochemistry* **16**, 673–677 (1968).
- 23. Greenwald, J. & Riek, R. Biology of Amyloid: Structure, Function, and Regulation. *Structure* **18**, 1244–1260 (2010).
- 24. Tycko, R. Amyloid Polymorphism: Structural Basis and Neurobiological Relevance. *Neuron* **86**, 632–645 (2015).

- 25. Nelson, R. *et al.* Structure of the cross-β spine of amyloid-like fibrils. *Nature* **435**, 773–778 (2005).
- 26. Colletier, J.-P. *et al.* Molecular basis for amyloid-polymorphism. *Proceedings of the National Academy of Sciences* **108**, 16938–16943 (2011).
- 27. Eisenberg, D. & Jucker, M. The Amyloid State of Proteins in Human Diseases. *Cell* **148**, 1188–1203 (2012).
- 28. Paravastu, A. K., Leapman, R. D., Yau, W.-M. & Tycko, R. Molecular structural basis for polymorphism in Alzheimer's beta-amyloid fibrils. *Proc. Natl. Acad. Sci. U.S.A.* **105**, 18349–18354 (2008).
- 29. Wiltzius, J. J. W. *et al.* Molecular mechanisms for protein-encoded inheritance. *Nat Struct Mol Biol* **16,** 973–978 (2009).
- 30. Rodriguez, J. A. *et al.* Structure of the toxic core of alpha-synuclein from invisible crystals. *Nature* **525**, 486 (2015).
- 31. Petkova, A. T. *et al.* Self-propagating, molecular-level polymorphism in Alzheimer's beta-amyloid fibrils. *Science* **307**, 262–265 (2005).
- 32. Lührs, T., Ritter, C. & Adrian, M. 3D structure of Alzheimer's amyloid-β(1–42) fibrils. in (2005).
- 33. Lu, J.-X. *et al.* Molecular Structure of β-Amyloid Fibrils in Alzheimer's Disease Brain Tissue. *Cell* **154**, 1257–1268 (2013).
- 34. Greenwald, J. & Riek, R. On the Possible Amyloid Origin of Protein Folds. *J. Mol. Biol.* (2012).
- 35. Fowler, D. M., Koulov, A. V., Balch, W. E. & Kelly, J. W. Functional amyloid from bacteria to humans. *Trends in biochemical* (2007).
- 36. Maji, S. K. *et al.* Functional amyloids as natural storage of peptide hormones in pituitary secretory granules. *Science* **325**, 328–332 (2009).
- 37. Tycko, R. Molecular structure of amyloid fibrils: insights from solid-state NMR. *Q. Rev. Biophys.* **39**, 1–55 (2006).
- 38. Wang, S. *et al.* Solid-state NMR spectroscopy structure determination of a lipid-embedded heptahelical membrane protein. *Nature Methods* **10**, 1007–1012 (2013).
- 39. Tycko, R. & Wickner, R. B. Molecular Structures of Amyloid and Prion Fibrils: Consensus versus Controversy. *Acc. Chem. Res.* (2013).
- 40. SPENCER, R. *et al.* An Unusual Peptide Conformation May Precipitate Amyloid Formation in Alzheimers-Disease Application of Solid-State Nmr to the Determination of Protein Secondary Structure. *Biochemistry* **30**, 10382–10387 (1991).
- 41. LANSBURY, P. T. *et al.* Structural Model for the Beta-Amyloid Fibril Based on Interstrand Alignment of an Antiparallel-Sheet Comprising a C-Terminal Peptide. *Nat Struct Mol Biol* **2,** 990–998 (1995).
- 42. Benzinger, T. *et al.* Propagating structure of Alzheimer's beta-amyloid((10-35)) is parallel beta-sheet with residues in exact register. *Proc. Natl. Acad. Sci. U.S.A.* **95**, 13407–13412 (1998).
- 43. Antzutkin, O. N. *et al.* Multiple quantum solid-state NMR indicates a parallel, not antiparallel, organization of beta -sheets in Alzheimer's beta -amyloid fibrils. *Proceedings of the National Academy of Sciences* **97**, 13045–13050 (2000).
- 44. Petkova, A. T. *et al.* A structural model for Alzheimer's beta-amyloid fibrils based on experimental constraints from solid state NMR. *Proc. Natl. Acad. Sci. U.S.A.* **99**, 16742–16747 (2002).
- 45. Kajava, A. V., Baxa, U. & Steven, A. C. β arcades: recurring motifs in naturally occurring and disease-related amyloid fibrils. *The FASEB Journal* (2010).
- 46. Colvin, M. T. et al. High Resolution Structural Characterization of Aβ 42Amyloid

- Fibrils by Magic Angle Spinning NMR. J. Am. Chem. Soc. 137, 7509–7518 (2015).
- 47. Qiang, W., Kelley, K. & Tycko, R. Polymorph-Specific Kinetics and Thermodynamics of β-Amyloid Fibril Growth Journal of the American Chemical Society (ACS Publications). *Journal of the American Chemical* ... (2013).
- 48. Bertini, I., Gonnelli, L., Luchinat, C., Mao, J. & Nesi, A. A New Structural Model of Aβ40 Fibrils. *JACS* (2011).
- 49. Lopez del Amo, J. M. *et al.* An Asymmetric Dimer as the Basic Subunit in Alzheimer's Disease Amyloid β Fibrils. *Angewandte Chemie International Edition* **51**, 6136–6139 (2012).
- 50. Tomiyama, T. *et al.* A new amyloid β variant favoring oligomerization in Alzheimer's-type dementia. *Ann Neurol.* **63**, 377–387 (2008).
- 51. Schütz, A. K. *et al.* Atomic-resolution three-dimensional structure of amyloid β fibrils bearing the Osaka mutation. *Angewandte Chemie International Edition* **54**, 331–335 (2015).
- 52. Grabowski, T. J., Cho, H. S., Vonsattel, J. P., Rebeck, G. W. & Greenberg, S. M. Novel amyloid precursor protein mutation in an Iowa family with dementia and severe cerebral amyloid angiopathy. *Ann Neurol.* **49**, 697–705 (2001).
- 53. Tycko, R., Sciarretta, K. L., Orgel, J. P. R. O. & Meredith, S. C. Evidence for Novel β-Sheet Structures in Iowa Mutant β-Amyloid Fibrils. *Biochemistry* **48**, 6072–6084 (2009).
- 54. Qiang, W., Yau, W.-M., Luo, Y., Mattson, M. P. & Tycko, R. Antiparallel β-sheet architecture in Iowa-mutant β-amyloid fibrils. *Proceedings of the National Academy of Sciences* **109**, 4443–4448 (2012).
- 55. Sawaya, M. R. *et al.* Atomic structures of amyloid cross-β spines reveal varied steric zippers. *Nature* **447**, 453–457 (2007).
- 56. Laganowsky, A. *et al.* Atomic View of a Toxic Amyloid Small Oligomer. *Science* **335**, 1228–1231 (2012).
- 57. Balbach, J. J. *et al.* Amyloid fibril formation by A beta(16-22), a seven-residue fragment of the Alzheimer's beta-amyloid peptide, and structural characterization by solid state NMR. *Biochemistry* **39**, 13748–13759 (2000).
- 58. Wasmer, C. *et al.* Amyloid Fibrils of the HET-s(218-289) Prion Form a Solenoid with a Triangular Hydrophobic Core. *Science* **319**, 1523–1526 (2008).
- 59. Chen, M., Margittai, M., Chen, J. & Langen, R. Investigation of alpha-Synuclein Fibril Structure by Site-directed Spin Labeling. *J. Biol. Chem.* **282**, 24970–24979 (2007).
- 60. Ahmed, M. *et al.* Structural conversion of neurotoxic amyloid-β1–42 oligomers to fibrils. *Nat Struct Mol Biol* **17,** 561–567 (2010).
- 61. Xiao, Y. *et al.* Aβ(1–42) fibril structure illuminates self-recognition and replication of amyloid in Alzheimer's disease. *Nat Struct Mol Biol* **22**, 499–505 (2015).
- 62. Spirig, T., Ovchinnikova, O., Vagt, T. & Glockshuber, R. Direct evidence for self-propagation of different amyloid-β fibril conformations. *Neurodegener Dis* **14**, 151–159 (2014).
- 63. Clayton, D. F. & George, J. M. The synucleins: a family of proteins involved in synaptic function, plasticity, neurodegeneration and disease. *Trends in neurosciences* (1998).
- 64. Clayton, D. F. & George, J. M. Synucleins in synaptic plasticity and neurodegenerative disorders Clayton 1999 Journal of Neuroscience Research Wiley Online Library. *Journal of neuroscience research* (1999).
- 65. Burré, J. *et al.* alpha-Synuclein Promotes SNARE-Complex Assembly in Vivo and in Vitro. *Science* **329**, 1663–1667 (2010).

- 66. Ibáñez, P. *et al.* Causal relation between α-synuclein locus duplication as a cause of familial Parkinson's disease. *The Lancet* **364**, 1169–1171 (2004).
- 67. TROJANOWSKI, J. Q. & LEE, V. M.-Y. Parkinson's Disease and Related α-Synucleinopathies Are Brain Amyloidoses. *Annals of the New York Academy of Sciences* **991**, 107–110 (2006).
- 68. Polymeropoulos, M. H. Mutation in the -Synuclein Gene Identified in Families with Parkinson's Disease. *Science* **276**, 2045–2047 (1997).
- 69. Vilar, M., Chou, H. T., Lührs, T. & Maji, S. K. The fold of α-synuclein fibrils. in (2008).
- 70. Hoyer, W., Becker, S. & Andronesi, O. C. Molecular-level secondary structure, polymorphism, and dynamics of full-length α-synuclein fibrils studied by solid-state NMR. in (2005).
- 71. Comellas, G. *et al.* Structured regions of α-synuclein fibrils include the early-onset Parkinson's disease mutation sites. *J. Mol. Biol.* **411**, 881–895 (2011).
- 72. Stefan Barghorn, Peter Davies, A.Eckhard Mandelkow. Tau Paired Helical Filaments from Alzheimer's Disease Brain and Assembled in Vitro Are Based on β-Structure in the Core Domain†. *Biochemistry* (2004).
- 73. Holtzman, D. M., Morris, J. C. & Goate, A. M. Alzheimer's Disease: The Challenge of the Second Century. *Science Translational Medicine* **3**, 77sr1–77sr1 (2011).
- 74. LEE, V. M.-Y., Goedert, M. & TROJANOWSKI, J. Q. N EURODEGENERATIVET AUOPATHIES. *Annu. Rev. Neurosci.* **24,** 1121–1159 (2001).
- 75. Daebel, V. *et al.* β-Sheet core of tau paired helical filaments revealed by solid-state NMR. *J. Am. Chem. Soc.* **134**, 13982–13989 (2012).
- 76. Wischik, C. M., Novak, M. & Edwards, P. C. Structural characterization of the core of the paired helical filament of Alzheimer disease. in (1988).
- 77. Wegmann, S. & Medalsy, I. D. The fuzzy coat of pathological human Tau fibrils is a two-layered polyelectrolyte brush. in (2013).
- 78. Aneta T Petkova, Wai-Ming Yau, A. & Tycko, R. Experimental Constraints on Quaternary Structure in Alzheimer's β-Amyloid Fibrils†. *Biochemistry* (2006).
- 79. Meinhardt, J., Sachse, C., Hortschansky, P., Grigorieff, N. & Fändrich, M. Abeta(1-40) fibril polymorphism implies diverse interaction patterns in amyloid fibrils. *J. Mol. Biol.* **386**, 869–877 (2009).
- 80. Schmidt, M. *et al.* Comparison of Alzheimer A (1-40) and A (1-42) amyloid fibrils reveals similar protofilament structures. *Proceedings of the National Academy of Sciences* **106**, 19813–19818 (2009).
- 81. Barber, D. J. & Freestone, I. C. AN INVESTIGATION OF THE ORIGIN OF THE COLOUR OF THE LYCURGUS CUP BY ANALYTICAL TRANSMISSION ELECTRON MICROSCOPY. *Archaeometry* (1990).
- 82. Ruivo, A. *et al.* Gold nanoparticles in ancient and contemporary ruby glass. *Journal of Cultural Heritage* **9**, e134–e137 (2008).
- 83. Faraday, M. The Bakerian lecture: experimental relations of gold (and other metals) to light. *Transactions of the Royal Society* (1857).
- 84. Graham, T. Liquid Diffusion Applied to Analysis on JSTOR. *Philosophical transactions of the Royal Society* (1861).
- 85. Turkevich, J., Stevenson, P. C. & Hillier, J. A study of the nucleation and growth processes in the synthesis of colloidal gold. *Discussions of the Faraday* (1951).
- 86. Joachim, C. To be nano or not to be nano? *Nat Mater* **4,** 107–109 (2005).
- 87. Lohmann, H. Über die Beziehungen zwischen den pelagischen Ablagerungen und dem Plankton des Meeres. *Int. Revue ges. Hydrobiol. Hydrogr.* **1**, 309–323 (1908).

- 88. Eigler, D. M. & Schweizer, E. K. Positioning single atoms with a scanning tunnelling microscope. *Nature* (1990).
- 89. Kriebel, J. K., Nuzzo, R. G. & Whitesides, G. M. Self-Assembled Monolayers of Thiolates on Metals as a Form of Nanotechnology Chemical Reviews (ACS Publications). *Chemical Reviews* **111**, 5610-5637 (2005).
- 90. Kuna, J. J. *et al.* The effect of nanometre-scale structure on interfacial energy. *Nat Mater* **8**, 837–842 (2009).
- 91. Häkkinen, H. The gold-sulfur interface at the nanoscale. *Nat Chem* **4**, 443–455 (2012).
- 92. Mazzarello, R. *et al.* Structure of a CH3S monolayer on Au(111) solved by the interplay between molecular dynamics calculations and diffraction measurements. *Phys. Rev. Lett.* **98**, (2007).
- 93. Cossaro, A. *et al.* X-ray diffraction and computation yield the structure of alkanethiols on gold(111). *Science* **321**, 943–946 (2008).
- 94. Jadzinsky, P. D., Calero, G., Ackerson, C. J., Bushnell, D. A. & Kornberg, R. D. Structure of a thiol monolayer-protected gold nanoparticle at 1.1 A resolution. *Science* **318**, 430–433 (2007).
- 95. Nuzzo, R. G. & Allara, D. L. Adsorption of bifunctional organic disulfides on gold surfaces Journal of the American Chemical Society (ACS Publications). *J. Am. Chem. Soc.* (1983).
- 96. Folkers, J. P., Laibinis, P. E. & Whitesides, G. M. Self-assembled monolayers of alkanethiols on gold: comparisons of monolayers containing mixtures of short- and long-chain constituents with methyl and hydroxymethyl terminal groups. *Langmuir* **8**, 1330–1341 (1992).
- 97. Folkers, J. P., Laibinis, P. E., Whitesides, G. M. & Deutch, J. Phase behavior of two-component self-assembled monolayers of alkanethiolates on gold. *J. Phys. Chem.* **98**, 563–571 (1994).
- 98. Stranick, S. J., Parikh, A. N., Tao, Y. T., Allara, D. L. & Weiss, P. S. Phase Separation of Mixed-Composition Self-Assembled Monolayers into Nanometer Scale Molecular Domains. *J. Phys. Chem.* **98**, 7636–7646 (1994).
- 99. Park, C., Yoon, J. & Thomas, E. L. Enabling nanotechnology with self assembled block copolymer patterns. *Polymer* (2003).
- 100. Singh, C. *et al.* Entropy-Mediated Patterning of Surfactant-Coated Nanoparticles and Surfaces. *Phys. Rev. Lett.* **99**, 226106 (2007).
- 101. Ong, Q. K. *et al.* High-Resolution Scanning Tunneling Microscopy Characterization of Mixed Monolayer Protected Gold Nanoparticles. *ACS Nano* 7, 8529–8539 (2013).
- 102. Centrone, A., Penzo, E. & Sharma, M. The role of nanostructure in the wetting behavior of mixed-monolayer-protected metal nanoparticles. in (2008).
- 103. Verma, A. *et al.* Surface-structure-regulated cell-membrane penetration by monolayer-protected nanoparticles. *Nat Mater* **7,** 588–595 (2008).
- 104. Giljohann, D. A. *et al.* Gold Nanoparticles for Biology and Medicine. *Angewandte Chemie International Edition* **49**, 3280–3294 (2010).
- 105. Allen, T. M. Drug Delivery Systems: Entering the Mainstream. *Science* **303**, 1818–1822 (2004).
- 106. Jiang, S. *et al.* Surface-functionalized nanoparticles for biosensing and imaging-guided therapeutics. *Nanoscale* **5,** 3127–3148 (2013).
- 107. Doane, T. L. & Burda, C. The unique role of nanoparticles in nanomedicine: imaging, drug delivery and therapy Chemical Society Reviews (RSC Publishing) DOI:10.1039/C2CS15260F. *Chemical Society Reviews* (2012).
- 108. Bowman, M.-C. et al. Inhibition of HIV Fusion with Multivalent Gold

- Nanoparticles. J. Am. Chem. Soc. 130, 6896–6897 (2008).
- 109. Nel, A. E. *et al.* Understanding biophysicochemical interactions at the nano–bio interface. *Nat Mater* **8**, 543–557 (2009).
- 110. Daniel, M. C. & Astruc, D. Gold Nanoparticles: Assembly, Supramolecular Chemistry, Quantum-Size-Related Properties, and Applications toward Biology, Catalysis, and Nanotechnology Chemical Reviews (ACS Publications). *Chemical reviews* (2004).
- 111. Sardar, R., Funston, A. M., Mulvaney, P. & Murray, R. W. Gold Nanoparticles: Past, Present, and Future. *Langmuir* **25**, 13840–13851 (2009).
- Hu, Y., Verma, A., Chen, S., Centrone, A. & Stellacci, F. Water -soluble amphiphilic gold nanoparticles with structured ligand shells Chemical Communications (RSC Publishing) DOI:10.1039/B713143G. *Chem Comm* (2007).
- 113. Moyano, D. F. & Rotello, V. M. Nano Meets Biology: Structure and Function at the Nanoparticle Interface. *Langmuir* (2011).
- 114. Moyano, D. F. *et al.* Fabrication of Corona-Free Nanoparticles with Tunable Hydrophobicity. *ACS Nano* (2014).
- 115. R Erik Holmlin, Xiaoxi Chen, Robert G Chapman, Shuichi Takayama, A. & Whitesides, G. M. Zwitterionic SAMs that Resist Nonspecific Adsorption of Protein from Aqueous Buffer. *Langmuir* (2001).
- 116. Van Lehn, R. C. *et al.* Lipid tail protrusions mediate the insertion of nanoparticles into model cell membranes. *Nat Comm* **5** (2014).
- 117. Carney, R. P. *et al.* Size Limitations for the Formation of Ordered Striped Nanoparticles. *J. Am. Chem. Soc.* **130**, 798–799 (2008).
- 118. Carney, R. P. *et al.* Determination of nanoparticle size distribution together with density or molecular weight by 2D analytical ultracentrifugation. *Nat Comm* **2**, 335 (2011).
- 119. Nanfeng Zheng, Jie Fan, A. & Stucky, G. D. One-Step One-Phase Synthesis of Monodisperse Noble-Metallic Nanoparticles and Their Colloidal Crystals. *Journal of the American Chemical* ... (2006).
- 120. Carney, R. P. *et al.* Electrical Method to Quantify Nanoparticle Interaction with Lipid Bilayers. *ACS Nano* **7**, 932–942 (2013).
- 121. Deamer, D. W. & Bramhall, J. Permeability of lipid bilayers to water and ionic solutes. *Chemistry and Physics of Lipids* **40**, 167–188 (1986).
- White, S. H. & Wimley, W. C. Membrane protein folding and stability: physical principles. *Annu Rev Biophys Biomol Struct* **28**, 319–365 (1999).
- Hediger, M. A., Romero, M. F., Peng, J. B. & Rolfs, A. The ABCs of solute carriers: physiological, pathological and therapeutic implications of human membrane transport proteins Springer. *Pflügers Archiv* (2004).
- 124. Herce, H. D. & Garcia, A. E. Molecular dynamics simulations suggest a mechanism for translocation of the HIV-1 TAT peptide across lipid membranes. *Proc. Natl. Acad. Sci. U.S.A.* **104**, 20805–20810 (2007).
- 125. Yesylevskyy, S., Marrink, S.-J. & Mark, A. E. Alternative Mechanisms for the Interaction of the Cell-Penetrating Peptides Penetratin and the TAT Peptide with Lipid Bilayers. *Biophysical Journal* **97**, 40–49 (2009).
- 126. Almeida, P. F. & Pokorny, A. Mechanisms of Antimicrobial, Cytolytic, and Cell-Penetrating Peptides: From Kinetics to Thermodynamics. *Biochemistry* **48**, 8083–8093 (2009).
- 127. Auluck, P. K., Caraveo, G. & Lindquist, S. α-Synuclein: Membrane Interactions and Toxicity in Parkinson's Disease. http://dx.doi.org/10.1146/annurev.cellbio.042308.113313 (2010).

- 128. Bucciantini, M. *et al.* Toxic effects of amyloid fibrils on cell membranes: the importance of ganglioside GM1. *The FASEB Journal* **26,** 818–831 (2012).
- 129. Yolamanova, M. *et al.* Peptide nanofibrils boost retroviral gene transfer and provide a rapid means for concentrating viruses. *Nature Nanotech* **8,** 130–136 (2013).
- 130. Usmani, S. M. *et al.* Direct visualization of HIV-enhancing endogenous amyloid fibrils in human semen. *Nat Comms* **5**, 3508 (2014).
- 131. Banerji, S. K. & Hayes, M. A. Examination of Nonendocytotic Bulk Transport of Nanoparticles Across Phospholipid Membranes Langmuir (ACS Publications). *Langmuir* (2007).
- 132. Leduc, C., Jung, J.-M., Carney, R. R., Stellacci, F. & Lounis, B. Direct Investigation of Intracellular Presence of Gold Nanoparticles via Photothermal Heterodyne Iaging. *ACS Nano* (2011).
- 133. Van Lehn, R. C. & Alexander-Katz, A. Fusion of Ligand-Coated Nanoparticles with Lipid Bilayers: Effect of Ligand Flexibility. *J. Phys. Chem. A* 140507111529003 (2014). doi:10.1021/jp411662c
- 134. Van Lehn, R. C. & Alexander-Katz, A. Ligand-Mediated Short-Range Attraction Drives Aggregation of Charged Monolayer-Protected Gold Nanoparticles. *Langmuir* **29**, 8788–8798 (2013).
- 135. Van Lehn, R. C. *et al.* Effect of Particle Diameter and Surface Composition on the Spontaneous Fusion of Monolayer-Protected Gold Nanoparticles with Lipid Bilayers. *Nano* ... (2013).
- 136. Van Lehn, R. C. & Alexander-Katz, A. Free energy change for insertion of charged, monolayer-protected nanoparticles into lipid bilayers. *Soft Matter* **10**, 648–658 (2014).
- 137. Van Lehn, R. C. & Alexander-Katz, A. Membrane-embedded nanoparticles induce lipid rearrangements similar to those exhibited by biological membrane proteins. *J. Phys. Chem. B* **118**, 12586–12598 (2014).
- 138. Van Lehn, R. C. & Alexander-Katz, A. Pathway for insertion of amphiphilic nanoparticles into defect-free lipid bilayers from atomistic molecular dynamics simulations. *Soft Matter* **11,** 3165–3175 (2015).
- 139. Chandler, D. Interfaces and the driving force of hydrophobic assembly. *Nature* **437**, 640–647 (2005).
- 140. Chamberlain, A. K., Lee, Y., Kim, S. & Bowie, J. U. Snorkeling preferences foster an amino acid composition bias in transmembrane helices. *J. Mol. Biol.* **339**, 471–479 (2004).
- Dorairaj, S. & Allen, T. W. On the thermodynamic stability of a charged arginine side chain in a transmembrane helix. *Proc. Natl. Acad. Sci. U.S.A.* **104,** 4943–4948 (2007).
- 142. Chernomordik, L. V. & Kozlov, M. M. Mechanics of membrane fusion. *Nat Struct Mol Biol* **15**, 675–683 (2008).
- 143. Mirjanian, D., Dickey, A. N., Hoh, J. H., Woolf, T. B. & Stevens, M. J. Splaying of Aliphatic Tails Plays a Central Role in Barrier Crossing During Liposome Fusion. *Journal of Physical Chemistry B* **114**, 11061–11068 (2010).
- 144. Smirnova, Y. G., Marrink, S.-J., Lipowsky, R. & Knecht, V. Solvent-Exposed Tails as Prestalk Transition States for Membrane Fusion at Low Hydration. *J. Am. Chem. Soc.* **132**, 6710–6718 (2010).
- 145. Atukorale, P. U. *et al.* Influence of the glycocalyx and plasma membrane composition on amphiphilic gold nanoparticle association with erythrocytes. *Nanoscale* 7, 11420–11432 (2015).
- 146. Fichou, Y. et al. Hydration water mobility is enhanced around tau amyloid fibers.

- Proc. Natl. Acad. Sci. U.S.A. E272-E281 (2015).
- Lund, T. *et al.* The influence of ligand organization on the rate of uptake of gold nanoparticles by colorectal cancer cells. *Biomaterials* **32**, 9776–9784 (2011).
- 148. Sousa, A. A. *et al.* Synthesis, Characterization, and Direct Intracellular Imaging of Ultrasmall and Uniform Glutathione-Coated Gold Nanoparticles. *Small* **8**, 2277–2286 (2012).
- 149. Yang, Y.-S., Carney, R. P., Stellacci, F. & Irvine, D. J. Enhancing Radiotherapy by Lipid Nanocapsule-Mediated Delivery of Amphiphilic Gold Nanoparticles to Intracellular Membranes. *ACS Nano* **8**, 8992–9002 (2014).
- 150. Mustalahti, S. *et al.* Ultrafast Electronic Relaxation and Vibrational Cooling Dynamics of Au-144(SC2H4Ph)(60) Nanocluster Probed by Transient Mid-IR Spectroscopy. *Journal of Physical Chemistry C* **118**, 18233–18239 (2014).
- 151. Mustalahti, S. *et al.* Molecule-like Photodynamics of Au-102(pMBA)(44) Nano cluster. *ACS Nano* **9,** 2328–2335 (2015).
- 152. Verma, A. & Stellacci, F. Effect of Surface Properties on Nanoparticle–Cell Interactions. *Small* **6**, 12–21 (2010).
- 153. Jeong, J. S., Ansaloni, A., Mezzenga, R., Lashuel, H. A. & Dietler, G. Novel mechanistic insight into the molecular basis of amyloid polymorphism and secondary nucleation during amyloid formation. *J. Mol. Biol.* **425**, 1765–1781 (2013).
- 154. Duboisset, J. *et al.* Thioflavine-T and Congo Red Reveal the Polymorphism of Insulin Amyloid Fibrils When Probed by Polarization-Resolved Fluorescence Microscopy. *J. Phys. Chem. B* **117**, 784–788 (2013).
- 155. Astbury, W. T. & Dickinson, S. alpha-beta Transformation of muscle protein in situ. *Nature* **135**, 765–765 (1935).
- 156. Sarroukh, R., Goormaghtigh, E. & Ruysschaert, J. M. ATR-FTIR: A 'rejuvenated' tool to investigate amyloid proteins. *Biophysica Acta* (2013).
- 157. Middleton, C. T. *et al.* Two-dimensional infrared spectroscopy reveals the complex behaviour of an amyloid fibril inhibitor. *Nat Chem* **4,** 355–360 (2012).
- 158. Micsonai, A. *et al.* Accurate secondary structure prediction and fold recognition for circular dichroism spectroscopy. *Proceedings of the National Academy of Sciences* **112,** E3095–E3103 (2015).
- 159. Khurana, R. *et al.* Mechanism of thioflavin T binding to amyloid fibrils. *J. Struct. Biol.* **151**, 229–238 (2005).
- 160. Knowles, T. P. J. *et al.* An Analytical Solution to the Kinetics of Breakable Filament Assembly. *Science* **326**, 1533–1537 (2009).
- 161. Cohen, S. I. A. *et al.* Proliferation of amyloid-β42 aggregates occurs through a secondary nucleation mechanism. *Proc. Natl. Acad. Sci. U.S.A.* **110,** 9758–9763 (2013).
- 162. Chen, B., Thurber, K. R., Shewmaker, F., Wickner, R. B. & Tycko, R. Measurement of amyloid fibril mass-per-length by tilted-beam transmission electron microscopy. *Proceedings of the National Academy of Sciences* **106**, 14339–14344 (2009).
- Bouchet-Marquis, C. & Hoenger, A. Cryo-electron tomography on vitrified sections: a critical analysis of benefits and limitations for structural cell biology. *Micron* **42**, 152–162 (2011).
- 164. Ecken, von der, J., Müller, M., Lehman, W. & Manstein, D. J. Structure of the Factin-tropomyosin complex: Nature: Nature Publishing Group. *Nature* (2015).
- 165. Adamcik, J., Jung, J. M., Flakowski, J. & De Los Rios, P. Understanding amyloid aggregation by statistical analysis of atomic force microscopy images: Nature Nanotechnology: Nature Publishing Group. *Nature* (2010).
- 166. Cohen, S. I. A. et al. A molecular chaperone breaks the catalytic cycle that generates

- toxic Aβ oligomers. Nat Struct Mol Biol 22, 207–213 (2015).
- 167. Patterson, J. The Preparation and Standardization of Colloidal Gold for the Lange Test. *British journal of experimental pathology* **12**, 143 (1931).
- 168. Mirkin, C. A., Letsinger, R. L. & Mucic, R. C. A DNA-based method for rationally assembling nanoparticles into macroscopic materials. *Nature*, **382**, 607-609 (1996).
- 169. Alivisatos, A. P. *et al.* Organization of 'nanocrystal molecules' using DNA. *Nature* **382**, 609–611 (1996).
- 170. Page Faulk, W. & Malcolm Taylor, G. Communication to the editors. *Immunochemistry* **8,** 1081–1083 (1971).
- 171. Mayhew, T. M., Mühlfeld, C. & Vanhecke, D. A review of recent methods for efficiently quantifying immunogold and other nanoparticles using TEM sections through cells, tissues and organs. *Annals of Anatomy* (2009).
- 172. Ackerson, C. J., Jadzinsky, P. D., Jensen, G. J. & Kornberg, R. D. Rigid, specific, and discrete gold nanoparticle/antibody conjugates. *J. Am. Chem. Soc.* **128**, 2635–2640 (2006).
- 173. Ackerson, C. J., Jadzinsky, P. D., Sexton, J. Z., Bushnell, D. A. & Kornberg, R. D. Synthesis and bioconjugation of 2 and 3 nm-diameter gold nanoparticles. *Bioconjug. Chem.* **21**, 214–218 (2010).
- 174. Goldschmidt, L., Teng, P. K., Riek, R. & Eisenberg, D. Identifying the amylome, proteins capable of forming amyloid-like fibrils. *Proc. Natl. Acad. Sci. U.S.A.* **107**, 3487–3492 (2010).
- Liao, Y. H., Chang, Y. J., Yoshiike, Y., Chang, Y. C. & Chen, Y. R. Negatively Charged Gold Nanoparticles Inhibit Alzheimer's Amyloid-β Fibrillization, Induce Fibril Dissociation, and Mitigate Neurotoxicity. *Small* **8**, 3631–3639 (2012).
- 176. Yoshiike, Y., Akagi, T. & Takashima, A. Surface structure of amyloid-beta fibrils contributes to cytotoxicity. *Biochemistry* **46**, 9805–9812 (2007).
- 177. Krishnan, R. *et al.* A Bacteriophage Capsid Protein Provides a General Amyloid Interaction Motif (GAIM) That Binds and Remodels Misfolded Protein Assemblies. *J. Mol. Biol.* **426**, 2500–2519 (2014).
- 178. Povilonienė, S. *et al.* Functionalization of α-synuclein fibrils. *Beilstein Journal of Nanotechnology* **6,** 124–133 (2015).
- 179. Holzer, M., Ghetti, B., Spillantini, M. G. & Crowther, R. A. Analysis of Tau Phosphorylation and Truncation in a Mouse Model of Human Tauopathy. *The American journal of Pathology,* **172**, 123-131 (2008).
- 180. Spillantini, M. G., Crowther, R. A., Jakes, R., Hasegawa, M. & Goedert, M. α-Synuclein in filamentous inclusions of Lewy bodies from Parkinson's disease and dementia with Lewy bodies. *Proceedings of the National Academy of Sciences* **95**, 6469–6473 (1998).
- 181. Crowther, R. A. Straight and paired helical filaments in Alzheimer disease have a common structural unit. in (1991).
- 182. Bolisetty, S., Adamcik, J., Heier, J. & Mezzenga, R. Amyloid Directed Synthesis of Titanium Dioxide Nanowires and Their Applications in Hybrid Photovoltaic Devices. *Advanced Functional Materials* **22**, 3424–3428 (2012).
- 183. Hertel, C. *et al.* Inhibition of the electrostatic interaction between β-amyloid peptide and membranes prevents β-amyloid-induced toxicity. *Proceedings of the National Academy of Sciences* **94**, 9412–9416 (1997).
- 184. Grey, M. *et al.* Acceleration of α-synuclein aggregation by exosomes. *J. Biol. Chem.* **290,** 2969–2982 (2015).
- 185. Yoshiike, Y., Chui, D.-H., Akagi, T., Tanaka, N. & Takashima, A. Specific compositions of amyloid-beta peptides as the determinant of toxic beta-aggregation.

- J. Biol. Chem. 278, 23648–23655 (2003).
- 186. Timothy McPherson, Argaw Kidane, Igal Szleifer, A.Kinam Park. Prevention of Protein Adsorption by Tethered Poly(ethylene oxide) Layers: Experiments and Single-Chain Mean-Field Analysis. *Langmuir* (1998).
- 187. Cao, Z. & Jiang, S. Super-hydrophilic zwitterionic poly(carboxybetaine) and amphiphilic non-ionic poly(ethylene glycol) for stealth nanoparticles. *Nano Today* (2012).
- 188. He, Y. *et al.* Molecular Simulation Studies of Protein Interactions with Zwitterionic Phosphorylcholine Self-Assembled Monolayers in the Presence of Water. *Langmuir* **24,** 10358–10364 (2008).
- Hayden, S. C. *et al.* Aggregation and Interaction of Cationic Nanoparticles on Bacterial Surfaces. *JACS*, **134**, 6920-6923 (2012).
- 190. Shengfu Chen, Jie Zheng, Lingyan Li, A. & Jiang, S. Strong Resistance of Phosphorylcholine Self-Assembled Monolayers to Protein Adsorption: Insights into Nonfouling Properties of Zwitterionic Materials. *Journal of the American Chemical* (2005).
- 191. Mangialasche, F., Solomon, A., Winblad, B. & Mecocci, P. Alzheimer's disease: clinical trials and drug development. *The Lancet* (2010).
- 192. Doody, R. S. *et al.* Phase 3 Trials of Solanezumab for Mild-to-Moderate Alzheimer's Disease. *N Engl J Med* **370**, 311–321 (2014).
- 193. Rao, P. P. N., Mohamed, T., Teckwani, K. & Tin, G. Curcumin Binding to Beta Amyloid: A Computational Study. *Chem Biol Drug Des* **86**, 813–820 (2015).
- 194. Cukalevski, R. *et al.* Role of Aromatic Side Chains in Amyloid β-Protein Aggregation. *ACS chemical* (2012).
- 195. Schmidt, M. et al. Peptide dimer structure in an A $\beta$ (1–42) fibril visualized with cryo-EM. Proceedings of the National Academy of Sciences 112, 11858-11863 (2015).
- 196. Liu, Y., Lin, X.-M., Sun, Y. & Rajh, T. In Situ Visualization of Self-Assembly of Charged Gold Nanoparticles. *JACS* (2013).
- 197. Siu, L. L. & Moore, M. J. Use of mesna to prevent ifosfamide-induced urotoxicity. *Support Care Cancer* **6**, 144–154 (2014).
- 198. Joe Tien, Andreas Terfort, A. & Whitesides, G. M. Microfabrication through Electrostatic Self-Assembly. *Langmuir* (1997).
- 199. Azubel, M. *et al.* Nanoparticle imaging. Electron microscopy of gold nanoparticles at atomic resolution. *Science* **345**, 909–912 (2014).
- 200. Levi-Kalisman, Y. *et al.* Synthesis and characterization of Au102(p-MBA)44 nanoparticles. *J. Am. Chem. Soc.* **133**, 2976–2982 (2011).
- 201. Pang, L. S. K., Saxby, J. D. & Chatfield, S. P. Thermogravimetric analysis of carbon nanotubes and nanoparticles. *J. Phys. Chem.* **97**, 6941–6942 (1993).
- 202. Lebon, A. *et al.* Magnetism, Charge Order, and Giant Magnetoresistance in SrFeO3–δSingle Crystals. *Phys. Rev. Lett.* **92**, 037202 (2004).
- 203. Jan, A., Hartley, D. M. & Lashuel, H. A. Preparation and characterization of toxic A[beta] aggregates for structural and functional studies in Alzheimer's disease research: Abstract: Nature Protocols. *Nature protocols* (2010).
- 204. Newcomb, C. J., Moyer, T. J., Lee, S. S. & Stupp, S. I. Advances in cryogenic transmission electron microscopy for the characterization of dynamic self-assembling nanostructures. *Current opinion in colloid* (2012).

#### Curriculum Vitae

#### Paulo H Jacob Silva

EPFL STI IMX SUNMIL, Station 12, MXG 032, 1015 Lausanne, Switzerland

Phone: +41 21 69 37877, paulo.jacob@epfl.ch; phjacob@gmail.com

#### **Education**

2011-present Doctorate (PhD) in Materials Science

École Polytechnique Fédérale de Lausanne (EPFL), Switzerland

Supramolecular Nanomaterials and Interfaces - SUNMIL

The Study of Amphiphilic Nanoparticles at the Biological Interface.

Thesis Director: Professor Francesco Stellacci

2007-2010 **Preclinical Medical Training** 

University of São Paulo Medical School (FMUSP) Internship: Intensive Care Unit of InCor (Heart Institute)

Research: Macrohemodynamic Response of Porcine Models to Septic Shock.

Prof. Dr. Luiz F. Poli de Figueiredo

2001-2006 Bachelor of Science (BSc.) in Materials Science and Engineering

Massachusetts Institute of Technology - MIT

Bachelor projects:

Cyclic Transformations in Ball-Milled Copper-Zirconium Alloys.

Prof. Christopher Schuh

Ligand-Phase Separation on Gold Nanoparticles.

Prof. Francesco Stellacci

## **Teaching Experience**

Teaching Assistantships.

Fall 2011

Fall 2012 and 2013

Fall 2014

"Surfaces and interfaces" Prof. Francesco Stellacci

"Thermodynamics for Materials Science" Prof. Francesco Stellacci "Introduction à la science des matériaux" Prof. Michel Rappaz

2011-2016 Throughout my doctoral studies I have trained masters and doctoral students

in addition to new post-doctoral fellows in nanoparticle synthesis and practices

of our laboratory.

## Languages

- Portuguese Mother Tongue.
- English Fluent written and spoken.
- **Spanish** Fluent spoken and reading, intermediate writing.
- French B2/C1
- German B2

#### **Peer-reviewed publications**

"From Homoligand- to Mixed-Ligand- Monolayer-Protected Metal Nanoparticles: A Scanning Tunneling Microscopy Investigation." Alicia M. Jackson, Ying Hu, Paulo Jacob Silva, and Francesco Stellacci. J. Am. Chem. Soc., 2006, 128 (34), pp 11135-11149

"High-Resolution Scanning Tunneling Microscopy Characterization of Mixed Monolayer Protected Gold Nanoparticles." Quy Khac Ong, Javier Reguera, Paulo Jacob Silva, Mauro Moglianetti, Kellen Harkness, Maria Longobardi, Kunal S. Mali, Christoph Renner, Steven De Feyter, and Francesco Stellacci. ACS Nano, 2013, 7 (10), pp 8529–8539

"Electrical Method to Quantify Nanoparticle Interaction with Lipid Bilayers." Randy P. Carney, Yann Astier, Tamara M. Carney, Kislon Voïtchovsky, **Paulo H. Jacob Silva**, Francesco Stellacci. *ACS Nano*, 2013, 7 (2), pp 932–942

"Lipid tail protrusions mediate the insertion of nanoparticles into model cell membranes." Reid C. Van Lehn, Maria Ricci, **Paulo H.J. Silva**, Patrizia Andreozzi, Javier Reguera, Kislon Voïtchovsky, Francesco Stellacci & Alfredo Alexander-Katz. *Nature Communications* **5**, 21 July 2014 Article number: 4482.

"Influence of the glycocalyx and plasma membrane composition on amphiphilic gold nanoparticle association with erythrocytes." Prabhani U. Atukorale, Yu-Sang Yang, Ahmet Bekdemir, Randy P. Carney, **Paulo J. Silva**, Nicki Watson, Francesco Stellacci and Darrell J. Irvine. *Nanoscale*, 2015,7, 11420-11432.

#### **Under revision**

"Additives to improve thermal stability of viruses from hours to months: implications for vaccine storage" Maria Pelliccia, Patrizia Andreozzi, Jayson Paulose, Marco D'Alicarnasso, Valeria Cagno, Manuela Donalisi, Andrea Civra, **Paulo Jacob Silva**, Randy P. Carney, Varpu Marjomäki, David Lembo, Francesco Stellacci\*, Vincenzo Vitelli\*, Silke Krol. *Under review – submitted to Nature Communications*.

#### **Attended Conferences**

Attended "Opportunities and Risks of Nanomaterials National Research Programme NRP 64" each year from 2012-2015. Presented a poster in 2014.

Participated in the NANOFOL – NanoDiaRa conference "Nanoparticles for Early Diagnostics of Inflammatory Diseases New approaches in the field of soft and hard nanoparticles" held on November 20th - 21st 2013, in Lisbon, Portugal.

**Gordon Research Conference (GRC)** Self-Assembly & Supramolecular Chemistry: 05/17/2015 - 05/22/2015 Tuscany, Italy. Presented poster

#### **Research Interests**

Materials Science, nanoscience and biomaterials. Disease mechanisms, histopathology and neuroscience.

#### **Non-Academic Professional Experience**

Co-founded PVsolar Energias Renovaveis. Since 2006 PVsolar pioneers the integration of non-hydraulic renewable energies in large-scale Brazilian hydro-power plants. Current projects include the first national renewable energy park in the Usina Hidrelétrica Engenheiro Sérgio Motta, Sao Paulo, Brazil. Current focus in hybrid pumped-storage hydroelectricity for battery-free solar energy storage.